Sebastian Franz Höfler, BSc

Preparation and Characterization of Integrated Organic Multi-Junction Solar Cell/ Lithium-Ion Battery Hybrid Devices for Simultaneous Energy Conversion and Storage

MASTER THESIS

In partial fulfillment of the requirements for the academic degree

Diplom-Ingenieur

in the field of study of Technical Chemistry

submitted at

Graz University of Technology

Supervisors

Assoc.Prof. Dipl.-Ing. Dr.techn. Gregor Trimmel

Institute for Chemistry and Technology of Materials

Dr. Ilie Hanzu

Institute for Chemistry and Technology of Materials

Graz, September 2015

AFFIDAVIT / EIDESSTATTLICHE ERKLÄRUNG

I declare that I have authored this thesis independently, that I have not used other than the declared sources/resources, and that I have explicitly indicated all material which has been quoted either literally or by content from the sources used. The text document uploaded to TUGRAZonline is identical to the present master's thesis.

Ich erkläre an Eides statt, dass ich die vorliegende Arbeit selbstständig verfasst, andere als die angegebenen Quellen/Hilfsmittel nicht benutzt, und die den benutzten Quellen wörtlich und inhaltlich entnommenen Stellen als solche kenntlich gemacht habe. Das in TUGRAZonline hochgeladene Textdokument ist mit der vorliegenden Masterarbeit identisch.

Date / Datum

Signature / Unterschrift

To my family

Abstract

A novel concept of an integrated solar battery hybrid device or power pack based on the combination of an organic multi-junction solar cell and a low-voltage lithium-ion battery for simultaneous energy conversion and storage is presented. The solar energy conversion and the electrochemical energy storage system are connected in series in a three-terminal assembly with two positive and a shared negative electrode. In order to charge the lithium-ion battery upon illumination of the photovoltaic system, a voltage exceeding 1.15 V needs to be supplied by the bulk-heterojunction tandem solar cell.

Tandem solar cells were prepared in normal device architecture consisting of a MoO_3 hole-transport layer, a benzothiadiazole-based small band gap polymer with carbazole moiety blended with a fullerene derivative as active layer in both sub-cells and Ti/Cu top electrodes. Various intermediate layers based on the combination of metals (Al, Ag, Au, Cu, Ti) and metal oxides (TiO_x, ZnO, MoO_3) with MoO_3 serving as electron- and hole-transport layer were investigated for enhanced photo-voltage generation. Lithium titanate ($Li_4Ti_5O_{12}$), cobalt diantimonide ($CoSb_2$) and cobalt triantimonide ($CoSb_3$) were used as electro-active species for composite electrodes for the low-voltage lithium-ion battery. The electrode materials were prepared and characterized in half- and full-cell configuration via common electrochemical methods including cyclic voltammetry (CV), galvanostatic cycling with potential limitation (GCPL), galvanostatic intermittent titration technique (GITT), and potentio electrochemical impedance spectroscopy (PEIS). Three different methods were presented to determine the chemical diffusion coefficient of Li^+ in $Li_4Ti_5O_{12}$, $CoSb_2$ and $CoSb_3$ composite electrodes, which were based on CV (Randles-Sevcik), PEIS (Warburg diffusion element) and GITT (Weppner-Huggins) measurements.

Integrated power packs were assembled and sealed under argon atmosphere by applying pressure on an O-ring via Plexiglas® plates to provide an air- and moisture-tight packaging of the solar battery hybrid device. The power pack was characterized on the basis of the performance of the solar cell via I-V measurements and of the lithium-ion battery via galvanostatic cycling experiments. Because of assembling and packaging problems and low voltages supplied by the photovoltaic system based on the impact of the liquid electrolyte of the battery system, the lithium-ion battery could not be charged upon illumination of the solar cell and no overall energy conversion and storage efficiency could be determined.

Kurzfassung

Integrierte Hybrid-Solarbatterien basieren auf der Umwandlung von Sonnenenergie in elektrische Energie durch Solarzellen unter gleichzeitiger Speicherung der elektrischen Energie in einer Batterie. Diese Arbeit behandelt ein neuartiges Konzept einer kombinierten organischen Mehrfachsolarzelle und einer Lithium-Ionen-Batterie, welches durch Serienschaltung in einem drei-terminalen, integrierten Aufbau mit zwei positiven und einer geteilten negativen Elektrode erreicht werden soll.

Die Ladung der integrierten Lithium-Ionen-Batterie erfolgt dabei durch Belichtung der Solarzelle. Um die benötigte Mindestspannung zum Laden der Batterie zu erreichen, wurden Bulk-Heterojunction Tandem-Solarzellen in Normalaufbau gebaut. Diese bestanden aus einer MoO_3 Lochleitungsschicht, einem Benzothiadiazol-basierten konjugierten Polymer mit Carbazol-Gruppe mit geringer Bandlücke kombiniert mit Fulleren-Derivaten als Aktivschicht und Ti/Cu-Elektroden. Verschiedene Zwischenschichten basierend auf einer Kombination von Metallen (Al, Ag, Au, Cu, Ti) oder Metalloxiden (TiO_x, ZnO, MoO_3) mit MoO_3 als Elektronen- und Lochleitungsschicht wurden hinsichtlich einer verbesserten Spannungserzeugung untersucht. Lithiumtitanat ($Li_4Ti_5O_{12}$), Cobaltdiantimonid ($CoSb_2$) und Cobalttriantimonid ($CoSb_3$) wurden als elektro-aktive Spezies zur Herstellung von Kompositelektroden in Lithium-Ionen-Batterien verwendet, welche unter Verwendung verschiedener elektrochemischer Methoden wie Cyclovoltammetrie (CV), Konstantstromzyklisierung (GCPL), galvanostatische Titrationsmethode (GITT) und potentiostatische elektrochemische Impedanzspektroskopie (PEIS) charakterisiert wurden. Zudem wurde der chemische Diffusionskoeffizient von Li^+ in $Li_4Ti_5O_{12}$, $CoSb_2$ und $CoSb_3$ Kompositelektroden mittels CV (Randles-Sevcik), PEIS (Warburg Diffusions-Element) und GITT (Weppner-Huggins) bestimmt.

Integrierte Hybrid-Solarbatterien wurden unter Argon-Atmosphäre assembliert und durch einen mit Plexiglas®-Platten angepressten O-Ring abgedichtet. Strom-Spannungs-Kennlinien- sowie GCPL-Messungen wurden zur Charakterisierung der Solarzelle bzw. der Lithium-Ionen-Batterie durchgeführt. Probleme bei der Assemblierung sowie niedrige Spannungen der Solarzelle aufgrund des Einflusses des Elektrolyten der Batterie führten dazu, dass die integrierte Lithium-Ionen-Batterie durch Belichtung der Tandem-Solarzelle nicht geladen und dahingehend auch keine Energie-Umwandlungs- und Speichereffizienz ermittelt werden konnte.

Acknowledgments

First of all, I want to express my gratitude to both of my supervisors Assoc.Prof. Dipl.-Ing. Dr.techn. Gregor Trimmel and Dr. Ilie Hanzu for giving me the opportunity to work on this very interesting field of integrated solar battery hybrid devices and of course for their pleasant permanent support during my master thesis.

Furthermore, I want to thank my colleagues in the working group for inspiring discussions, useful comments and remarks, and all people employed at the Institute for Chemistry and Technology of Materials (ICTM) of Graz University of Technology for the friendly and enjoyable atmosphere. I also want to thank my friends and all people I met during my studies for their support and motivation throughout writing this thesis.

My deepest gratitude is dedicated to my family, especially my parents and my brother, for supporting me from the very beginning and during my studies.

List of Abbreviations

[60]PCBM	[6,6]-phenyl-C_{61}-butyric acid methyl ester
[70]PCBM	[6,6]-phenyl-C_{71}-butyric acid methyl ester
α	transfer coefficient
a	exponent of the constant phase element
A	surface area of the electrode [cm^2]
AC	alternating current
ACC	acceptor
AM	air mass
BET	Brunauer-Emmett-Teller
BHJ	bulk-heterojunction
C	concentration of inserted species [mol cm^{-3}] or concentration of active centers [mol cm^{-3}]
CB	chlorobenzene
CE	counter electrode
CIGS	copper indium gallium diselenide
CIS	copper indium diselenide
CPE	constant phase element
CV	cyclic voltammetry
D	chemical diffusion coefficient [$cm^2\ s^{-1}$]
DC	direct current
DCB	1,2-dichlorobenzene
DLS	dynamic light scattering
DMC	dimethyl carbonate
DON	donor
DSSC	dye-sensitized solar cell
$E^{0'}$	formal potential of a redox couple [V]
EC	ethylene carbonate
E_{CE}	potential at the counter electrode [V]
E_g	band gap [eV]
E_{HOMO}	energy level of the highest occupied molecular orbital [eV]

E_{LUMO}	energy level of the lowest unoccupied molecular orbital [eV]
EMC	ethylmethyl carbonate
ΔE_p	peak separation [V]
$E_{p,a}$	anodic potential peak [V]
$E_{p,c}$	cathodic potential peak [V]
EQE	external quantum efficiency [%]
ΔE_s	change of the steady-state voltage during the current pulse [V]
ΔE_t	total transient change of the cell voltage during the current pulse [V]
ETL	electron-transport layer
E_{WE}	potential at the working electrode [V]
F	Faraday constant [As mol^{-1}]
F8T2	poly[(9,9-dioctylfluorenyl-2,7-diyl)-*co*-bithiophene]
FF	fill factor [%]
GCPL	galvanostatic cycling with potential limitation
GITT	galvanostatic intermittent titration technique
HOMO	highest occupied molecular orbital
HTL	hole-transport layer
I	current [A]
ICBA	indene-C_{60} bisadduct
IEA	International Energy Agency
i_p	peak current [A]
$i_{p,a}$	anodic peak current [A]
$i_{p,c}$	cathodic peak current [A]
$i_{p,max}$	maximal peak current [A]
IPCE	incident photon-to-current efficiency
ITO	indium tin oxide
j	imaginary number
J	current density [mA cm^{-2}]
J_{sc}	short-circuit current density [mA cm^{-2}]
LTO	lithium titanate
LUMO	lowest unoccupied molecular orbital
m_i	mass of active material of component i in the electrode [g]
M_i	molecular weight of component i [g mol^{-1}]
ν	scan rate [V s^{-1}]

n	number of exchanged electrons
n_a	number of exchanged electrons
NMP	1-methyl-2-pyrrolidone
OCV	open circuit voltage [V]
OSC	organic solar cell
PCDTBT	poly[*N*-9´-heptadecanyl-2,7-carbazole-*alt*-5,5-(4´,7´-di-2-thienyl-2´,1´,3´-benzothiadiazole)]
PCE	power conversion efficiency [%]
PCPDTBT	poly[2,6-(4,4-bis(2-ethylhexyl)-4*H*-cyclopenta[2,1-b;3,4-b′]dithiophene)-*alt*-4,7(2,1,3-benzothiadiazole)]
PEDOT:PSS	poly(3,4-ethylenedioxythiophene) polystyrene sulfonate
PEIS	potentio electrochemical impedance spectroscopy
PSiF-DBT	poly[2,1,3-benzothiadiazole-4,7-diyl-2,5-thiophenediyl(9,9-dioctyl-9*H*-9-silafluorene-2,7-diyl)-2,5-thiophenediyl]
PV	photovoltaic
PVD	physical vapor deposition
R	ideal gas constant [J mol^{-1} K^{-1}]
R_{ct}	charge transfer resistance [Ω]
R_e	resistance of the electrolyte [Ω]
RE	reference electrode
R_i	dynamic resistance [Ω]
R_s	series resistance [Ω cm^2]
R_{sh}	shunt resistance, parallel resistance [kΩ cm^2]
S	electrode surface area [cm^2]
sccm	standard cubic centimeters per minute
SEM	scanning electron microscopy
τ	period of the galvanostatic current pulse [s]
T	absolute temperature [K]
T_W	modulus of the Warburg element [Ω s$^{-1/2}$]
V	voltage [V]
V_M	molar volume [cm^3 mol^{-1}]
V_{mpp}	voltage at the maximum power point [V]
V_{OC}	open circuit voltage [V]
ω	angular frequency [rad/s]

W	Warburg element
WE	working electrode
XRD	X-ray diffraction
Z	impedance
Z_W	Warburg diffusion element
$Z_W(\omega)$	Warburg diffusion element as function of frequency

Table of Contents

1 Introduction

Fossil fuels such as coal, oil and natural gas are the major global energy sources covering about 80% of the world total primary energy supply (Figure 1).[1] The accelerated use of fossil reserves, however, contributes to the global climate change and, since fossil fuels are exhaustible resources, might culminate in a future energy crisis, unless progress in alternative energy sources is made.[2–4] Renewable energy technologies such as wind power, hydropower, solar energy, geothermal energy, and bio energy represent a credible solution addressing these major concerns. The share of renewables in the global total primary energy supply of 13.5% (2012) is marginal compared to fossil fuels but is expected to increase to 15-26% by 2035 according to various scenarios and projections presented in the World Energy Outlook of the International Energy Agency (IEA).[5] Among these renewable energy technologies, solar energy is the most promising candidate providing an enormous potential to meet the global energy demand and to tackle the energy crisis. To illustrate this, given a world total energy consumption of about 376 EJ in 2012[1], solar energy with an annual potential of 1,575-49,387 EJ would fully cover the world's primary energy demand in 2012.[6]

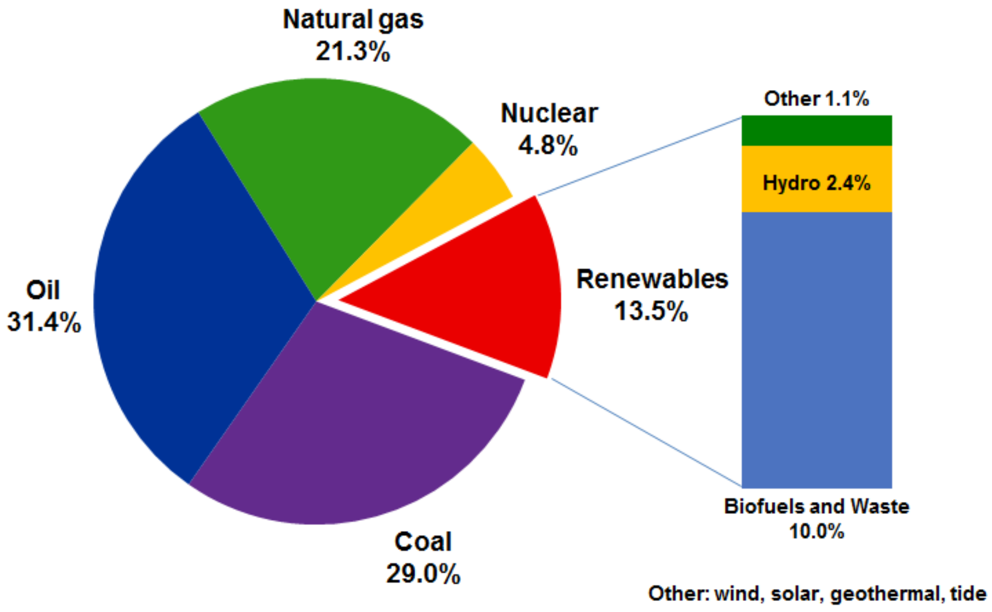

Figure 1: Fuels shares of world total primary energy supply in 2012 (data taken from [1])

The share of solar energy in the global total primary energy supply is far below 1%. Nevertheless, it retains a high potential, in particular in the area of electricity production. For example, a rapid growth in the electricity production via photovoltaic (PV) systems around 10 to 20 times from 2011 to 2035 is predicted.[5] However, important challenges in PV systems design are raised by diurnal and seasonal fluctuations of solar irradiation as well as the dependence on weather conditions (e.g. shadowing by clouds). This implies variations in the solar electricity supply because of non-continuous solar irradiation levels that further lead to stability and reliability problems of the power grid system.[2] This stability and reliability issue will become even more severe in the next decades since the number of PV installations and solar electricity production is expected to increase.[5]

In order to buffer electricity peaks and to provide a constant electricity supply independent from external influences, electrical energy can be converted into storable energy forms and back into electrical energy on demand.[7] On the basis of the energy storage form in the system, electrical energy storage technologies can be classified into mechanical (e.g. pumped hydroelectric storage), electrical (e.g. capacitors), thermal (e.g. latent or sensible heat storage), chemical (e.g. hydrogen storage), electrochemical (e.g. rechargeable battery systems) and thermochemical (e.g. solar fuels) energy storage technologies.[8–10] Electricity supplied by PV systems can be stored in various energy storage devices, among which electrochemical energy storage technologies provide major potential especially for decentralized storage. Examples of such electrochemical energy storage technologies are rechargeable batteries (e.g. lead-acid battery, nickel-cadmium battery, nickel-metal hydride battery, lithium-ion battery) and redox flow batteries.

In conventional energy storage systems, the solar energy conversion device and the energy storage device are part of two independent, non-integrated, four-terminal systems contacted by wiring. This means that the photo-generated electricity is transferred from the PV system via wiring to an external electrochemical storage system. However, there are many shortcomings related to such non-integrated technologies mainly in terms of size, weight and limitations with regard to flexibility.[11] This is why integrated assemblies of solar energy conversion and storage technologies in one single device have been reported recently.[2,11–14] Such hybrid devices or power packs are integrated, three-terminal systems made by stacking of a solar energy conversion and an energy storage device. Various combinations of solar energy converters and electrical or electrochemical energy storage systems are used in integrated hybrid devices such as silicon nanowire-based solar cells with lithium-ion batteries[12], dye-sensitized solar cells (DSSCs) with lithium-ion batteries[11], DSSCs with lithium-oxygen batteries[13], DSSCs with redox flow batteries[2], silicon solar cells with supercapacitors[15], DSSCs with supercapacitors[16], organic tandem solar cells with supercapacitors[17], and perovskite solar cells with supercapacitors [14].

Apart from tackling the imbalance between solar energy supply and energy demand, both non-integrated (four-terminal) and integrated (three-terminal) solar energy conversion and storage devices facilitate energy-self-sufficient operation in off-grid systems. This provides major potential for developing countries, in particular in remote areas with missing connections to the electricity grid. Integrated power packs, however, have many advantages compared to non-integrated systems including size, weight, and a simultaneous energy conversion and storage without the need of contacting of two independent devices by wiring.[11] Self-powering portable and mobile energy systems, for example electronics such as mobile phones or wireless sensors, can be manufactured in small and light-weight devices and improve the customer's flexibility.[11,12,14,18] The fabrication of bendable, ultrathin, integrated energy wires provides a potential application in the fields of electronic textiles and smart clothing.[18]

Nevertheless, there is still a debate about the applicability and future prospects of integrated devices because of the competition with already marketed, non-integrated technologies. This is because integrated hybrid devices have to face various drawbacks such as air- and moisture-tight packaging requirements and problems with regard to up-scaling for high-energy demand applications. There is still much effort required to improve the performance of the energy conversion and storage systems and to optimize the assembling procedure and packaging process to bring such power packs on the market.

1.1 *Aims of this Thesis*

In this work, a novel concept of an integrated solar battery hybrid device based on the combination of an organic multi-junction solar cell and a lithium-ion battery is presented. This power pack consists of an organic tandem solar cell in normal device architecture stacked in series with a low-voltage lithium-ion battery to obtain a three-terminal assembly (Figure 2).

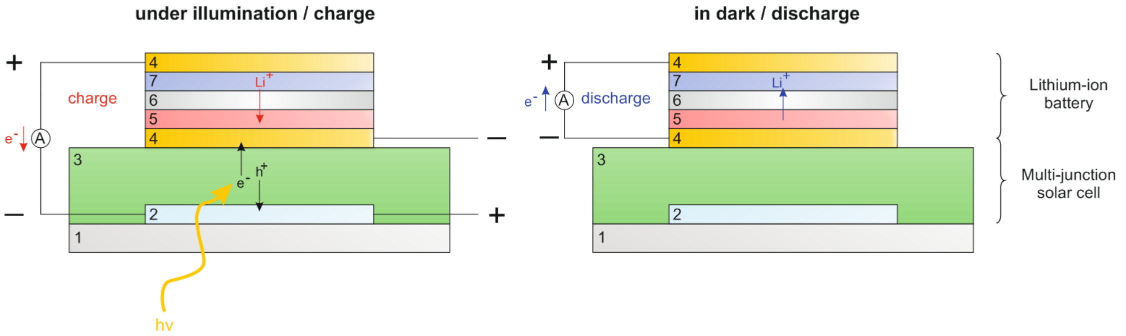

Figure 2: General design (without packaging) and schematic representation of the working mechanism of the integrated solar battery hybrid device under illumination/charge and in dark/discharge: (1) glass, (2) ITO, (3) multi-junction solar cell, (4) copper current collector, (5) $CoSb_y$ (y = 2,3), negative electrode, (6) separator + electrolyte, (7) $Li_4Ti_5O_{12}$, positive electrode

The working mechanism (Figure 2) of this integrated power pack is based on a combined light-to-electricity conversion and storage process. In principle, the battery is charged upon illumination of the solar cell and discharged under dark conditions. In order to charge the battery, an over-voltage has to be applied, which should be accomplished by the voltage provided by the organic multi-junction solar cell. Upon illumination of the solar cell, excitons are created within the photo-active layer, which are separated at the donor/acceptor interface by applying an electric field. The generated holes and electrons are transported to the positive electrode and negative electrode of the solar cell, respectively. The over-voltage provided by the organic multi-junction solar cell forces electrons from the lithium ion battery to move via the external circuit to the indium tin oxide (ITO) electrode of the solar cell, concomitant with the movement of Li ions via the electrolyte and separator to the negative electrode (charging). Under dark conditions, the battery is discharged on the external load and Li ions move from the negative to the positive electrode via the electrolyte and separator, whereas electrons move via the external circuit to the positive electrode. In dark, the photovoltaic cell behaves like a diode biased in the blocking direction.

Subject of this work was the fabrication and optimization of organic solar cells for high photo-voltage generation, the preparation and electrochemical characterization of electrode materials for lithium-ion batteries, and combination of the solar energy conversion and electrochemical energy storage technology in an integrated solar battery hybrid device. Basically, in order to charge the low-voltage lithium-ion battery with the organic solar cell in the integrated solar battery hybrid device, appropriate materials for high photo-voltage generation need to be evaluated. This is why benzothiadiazole-based small band gap and polyfluorene-based wide band gap polymers (donor) were combined with fullerene derivatives (acceptor) in bulk-heterojunction solar cells. For improved photo-voltage generation, various intermediate layer combinations based on thermally evaporated metals and metal oxides as electron- and hole-transport layer were investigated in multi-junction solar cells. For optimization of the device performance, the effect of the hole-transport layer thickness, the solvent for solution processing, thermal annealing and additional metal and alkali-metal compound layers was examined.

A low-voltage lithium-ion battery system was chosen as energy storage technology for the integrated power pack because of limitations with regard to the voltage provided by the solar cell. Therefore, appropriate electrode materials were evaluated, prepared and electrochemically characterized in half- and full-cell configuration in three-electrode Swagelok cells with regard to their specific capacity, charge/discharge capacity and cycling stability. Moreover, the chemical diffusion coefficient of Li^+ in the prepared composite electrodes was determined via cyclic voltammetry (Randles-Sevcik), potentio electrochemical impedance spectroscopy (Warburg diffusion element) and galvanostatic intermittent titration technique (Weppner-Huggins).

Finally, an organic multi-junction solar cell and a low-voltage lithium-ion battery were combined in an integrated power pack sealed with an O-ring. The photovoltaic system was characterized via I-V measurements and the lithium-ion battery via galvanostatic cycling. The integrated hybrid device should be charged upon illumination of the solar cell and discharged under dark conditions.

1.2 Photovoltaics

Solar cells are photovoltaic systems for conversion of solar energy to electrical energy. Depending on the materials used, three different generations of solar cells are distinguished. First generation solar cells are based on mono- or polycrystalline silicon and are the most common photovoltaic technology.[19] Second generation solar cells such as thin-film solar cells provide major potential for reduction of fabrication costs and use materials like cadmium telluride (CdTe), copper indium diselenide (CIS), copper indium gallium diselenide (CIGS), gallium arsenide (GaAs) or amorphous silicon (a-Si).[20,21] Emerging technologies for future solar electricity supply are based on dye-sensitized solar cells, organic solar cells, hybrid polymer solar cells and perovskite solar cells (third generation solar cells).[22]

1.2.1 Organic Solar Cells

Organic solar cells (OSCs) are based on organic semiconductors which enable the conversion of solar energy to electrical energy.[4,23] Materials for OSCs include organic, conjugated polymers with a delocalized π electron system (e.g. polythiophenes) and organic small molecules (e.g. phthalocyanines).[23] Considering polymer-based OSCs, the conjugated polymer (donor) is combined with various acceptor materials such as fullerenes (e.g. C_{60}), fullerene derivatives (e.g. [60]PCBM, [70]PCBM), electron-accepting polymers (e.g. cyano-substituted conjugated polymers), or organic small molecules (e.g. perylenes).[23–26] Donor and acceptor materials constitute the photo-active layer of solar cells forming either a separated layer structure (bilayer-heterojunction) or a nanoscale interpenetrating network of donor and acceptor domains (bulk-heterojunction, BHJ), shown in Figure 3.

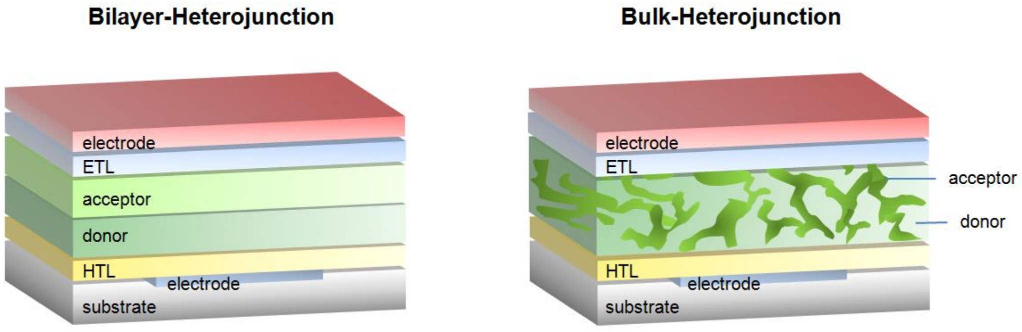

Figure 3: Bilayer-heterojunction and bulk-heterojunction solar cells

BHJ-type OSCs consist of a photo-active layer of donor and acceptor embedded between two electrodes (Figure 4). Interfacial layers between the photo-active layer and the electrodes alleviate charge transfer processes of electrons and holes to the respective electrodes and minimize leakage currents. Holes are transported via a hole-transport layer (HTL) to the anode, whereas electrons are transported via an electron-transport layer (ETL) to the cathode. OSCs are generally fabricated in two different configurations, namely normal and inverted device architecture, which differ in the materials used for the top electrodes. These are made of low work function metals (e.g. aluminum) in normal device architecture (cathode) and of high work function metals (e.g. silver, gold) in inverted device architecture (anode).[27] A typical substrate material is glass, which is usually coated with a transparent conductive oxide (e.g. indium tin oxide, ITO) serving as electrode. Common materials for HTLs and ETLs are poly(3,4-ethylenedioxythiophene) polystyrene sulfonate (PEDOT:PSS) and TiO_x, respectively.[27]

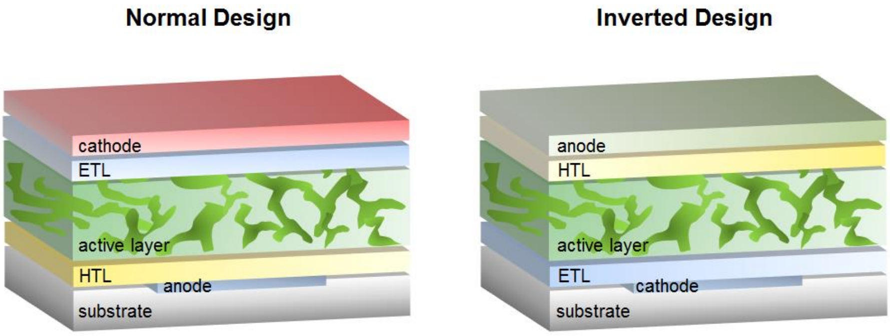

Figure 4: Bulk-heterojunction solar cells in normal and inverted device architecture

The conversion process of light energy into electrical energy in OSCs is based on a series of various physical processes (Figure 5).[23,28] Upon illumination of solar cells, photons with an energy exceeding the band gap of the donor or the acceptor are absorbed by the photo-active material within the active layer (1). The photon absorption initiates the excitation of an electron from the highest occupied molecular orbital (HOMO) to the lowest unoccupied molecular orbital (LUMO) and thus the formation of a coulombically bound electron-hole pair, called exciton.[23] In case of photo-excitation and exciton generation in the donor material, the exciton diffuses within the donor phase until it reaches the acceptor phase or decays via radiative or non-radiative paths depending on the diffusion length and the lifetime of the created electron-hole pair (2).[23,28] If the exciton reaches the acceptor within its lifetime and diffusion length (ns- and nm-regime)[29], the electron is transferred to the acceptor phase forming a metastable charge-transfer electron-hole pair across the donor/acceptor interface.[28,30] An electric field is required for charge separation based on the dissociation of the exciton into a photo-generated electron and hole (3).[28] The free charge carriers migrate to the respective electrodes based on the internal electric field provided by electrodes with different work functions (4).[28,31] Electrons are transported via percolated acceptor paths to the cathode and holes via donor domains to the anode, followed by extraction of the free charge carriers at the electrodes (5).

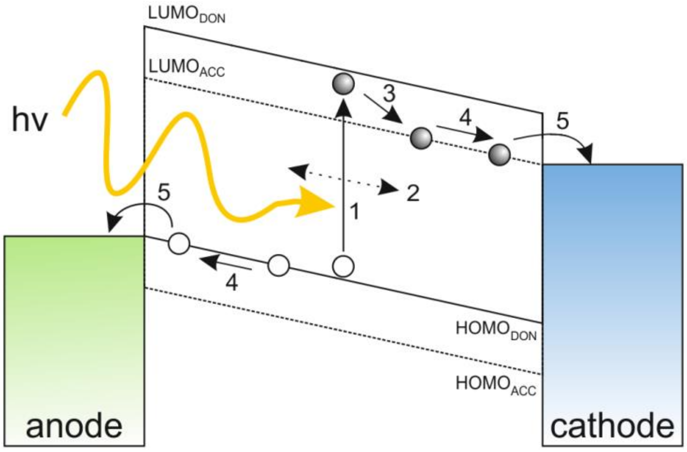

Figure 5: Fundamental physical processes for photo-current generation upon illumination of bulk-heterojunction organic solar cells in normal device architecture based on the photo-excitation of the donor material: (1) photon absorption, (2) exciton diffusion, (3) exciton dissociation, (4) free carrier migration, (5) carrier extraction[28] (DON = donor, ACC = acceptor)

The maximal theoretical conversion efficiency of single-junction solar cells with an energy band gap of 1.1 eV is limited by 30% under non-concentrated, illuminated conditions derived from W. Shockley and H. J. Queisser.[32] This is based on two major phenomena (Figure 6):

- Only photons with an energy exceeding the band gap of the photo-active materials are absorbed and contribute to the conversion efficiency but photons with lower energy cannot generate excited states and thus lead to sub-band gap transmission losses.[4,25,33]
- Photons with an energy exceeding the band gap create hot charge carriers, which relax down to the LUMO level of the donor material and thus, the excess photon energy is lost by thermalization of hot charge carriers.[4,30]

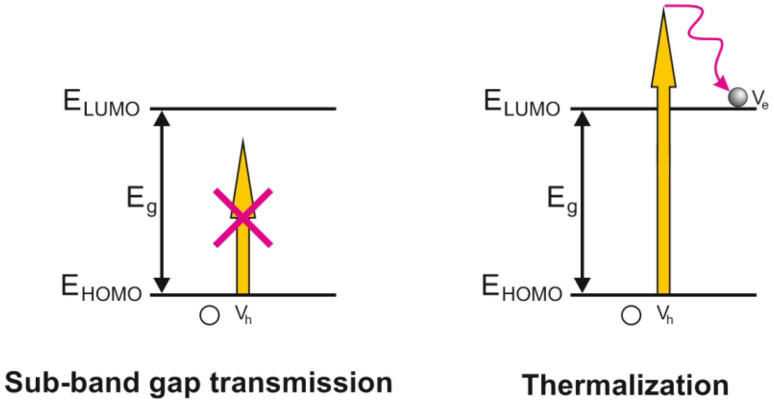

Sub-band gap transmission

Thermalization

Figure 6: Sub-band gap transmission and thermalization losses in organic solar cells[4]

The Shockley-Queisser limit of single-junction solar cells can be exceeded by solar cells in tandem or multi-junction configuration. Tandem and multi-junction solar cells consist of two or further stacked solar cells connected in series (two-terminal) or parallel (three-terminal).[34] According to De Vos, the theoretical conversion efficiency of tandem solar cells with energy band gaps of 1.9 eV and 1.1 eV can be increased to 42.3%.[35] Stacking of sub-cells with complementary absorption behavior, for example of solar cells with wide and small band gap polymers, enables to cover the solar emission spectrum more efficiently in order to enhance light harvesting and photo-current generation (Figure 7). Photons with higher energy are absorbed by the wide band gap sub-cell and photons with lower energy by the small band gap sub-cell, yielding enhanced solar-to-electricity conversion efficiencies. However, the maximum photo-current generation of multi-junction solar cells is limited by the smallest short-circuit current density (J_{SC}) of a sub-cell (Kirchhoff's law).[34]

Sub-cells of multi-junction solar cells are connected via intermediate or recombination layers, which ensure the recombination of charge carriers. In case of normal tandem device architecture, electrons from the front cell are injected via the electron-transport layer and holes coming from the back cell are injected via the hole-transport layer (Figure 7).[4] Using the multi-junction approach higher photo-voltages can be generated compared to single-junction solar cells. The open circuit voltage (V_{OC}) of a multi-junction solar cell equals the sum of the V_{OC}s of each contributing sub-cell (Kirchhoff's law), which is only valid for ideal, fully-transparent intermediate layers enabling loss-free charge recombination.[34]

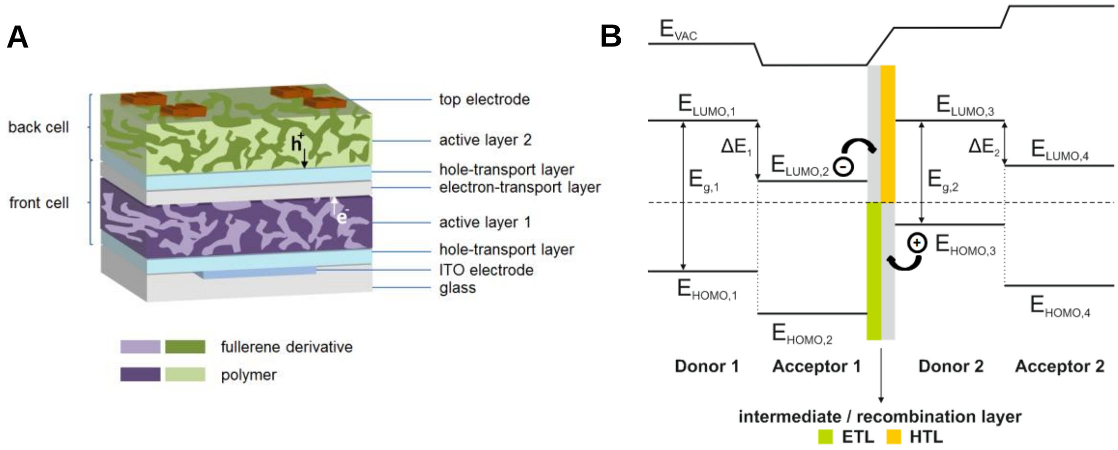

Figure 7: (A) Basic design of bulk-heterojunction multi-junction solar cells with two different active layers connected in series in normal device architecture. (B) Band diagram of a multi-junction solar cell connected in series via intermediate layers consisting of an electron- and hole-transport layer[34]

In this work, bulk-heterojunction solar cells were prepared in normal device architecture consisting of a MoO_3 hole-transport layer, a blend of conjugated polymers (PCDTBT, PSiF-DBT, PCPDTBT, F8T2) and fullerene derivatives ([60]PCBM, [70]PCBM, ICBA) as donor and acceptor material, and titanium/copper top electrodes. Single-junction solar cells were optimized with regard to the hole-transport layer thickness and the film morphology (solvent effect, thermal annealing). Multi-junction solar cells were fabricated by stacking sub-cells in series via recombination layers. These intermediate layers were based on a combination of metal and metal oxides with MoO_3 serving as electron- and hole-transport layer. Additional metal and alkali-metal compound layers were introduced for the optimization of the device performance. Tandem solar cells were required to supply enough voltage (1.15 V) to charge the low-voltage lithium-ion battery in the integrated solar battery hybrid device upon illumination.

Solar cells were characterized based on their characteristic parameters including the open circuit voltage (V_{OC}), the short-circuit current density (J_{SC}), the fill factor (FF) and the power conversion efficiency (PCE) obtained from I-V measurements, which were averaged over five devices. Series (R_s) and shunt resistances (R_{sh}) were calculated from the J-V curves under illumination. Furthermore, single-junction solar cells were characterized via IPCE (incident photon-to-current efficiency) measurements.

1.3 Lithium-Ion Battery

Lithium-ion batteries are secondary, rechargeable batteries used for electrochemical energy storage and conversion. Reversible charging and discharging processes enable an effective conversion of electrical energy into chemical energy upon charging and vice versa upon discharging.

A classical lithium-ion battery consists of a positive and a negative electrode separated by an electrolyte-soaked separator. Positive electrodes are typically made of inorganic transition metal oxides (e.g. V_2O_5[36], MnO_2[36]) and chalcogenides (e.g. TiS_2[37]).[38] Moreover, organic molecules and polymers have been used as cathode materials in rechargeable batteries.[38] Positive electrode materials can be further classified into lamellar compounds (e.g. $LiCoO_2$, $LiNi_{1/3}Mn_{1/3}Co_{1/3}O_2$), spinel compounds (e.g. $LiMn_2O_4$) and olivine group compounds (e.g. $LiFePO_4$).[39] Negative electrodes are typically made of insertion materials based on carbons (e.g. graphite[40]), transition metal oxides (e.g. TiO_2[41]) and chalcogenides (e.g. MoS_2[42]), and lithium alloys (e.g. Li-Al alloys[43], Li-Sn alloys[44]), among which graphite is the most important one and the system with the widest commercial use.[38] Separators are able to retain the liquid lithium electrolyte in a percolating network of cavities and are placed between the positive and negative electrode to avoid direct contact and short circuits. Typical separator materials for lithium-ion batteries are polymer-based microporous materials such as polyolefins.[45] Liquid electrolytes in lithium-ion batteries provide conductive paths for alkali metal ion transport processes upon repeated charge-discharge processes. Electrolytes consist of lithium salts (e.g. $LiPF_6$, $LiBF_4$, $LiClO_4$) dissolved in organic alkyl carbonate solvents such as ethylene carbonate (EC), dimethyl carbonate (DMC) and ethylmethyl carbonate (EMC).[46,47]

During charging, a voltage is applied by an external power source to force electrons to move from the positive to the negative electrode via the external electric circuit, concomitant with the Li ion movement from the positive to the negative electrode via the electrolyte. During discharge, Li ions migrate in the reverse direction, concomitantly with the transport of electrons via the external electric circuit in the same direction. Figure 8 shows the basic principle of charge-discharge reactions in lithium-ion batteries using the example of a graphite/$LiCoO_2$ battery system.

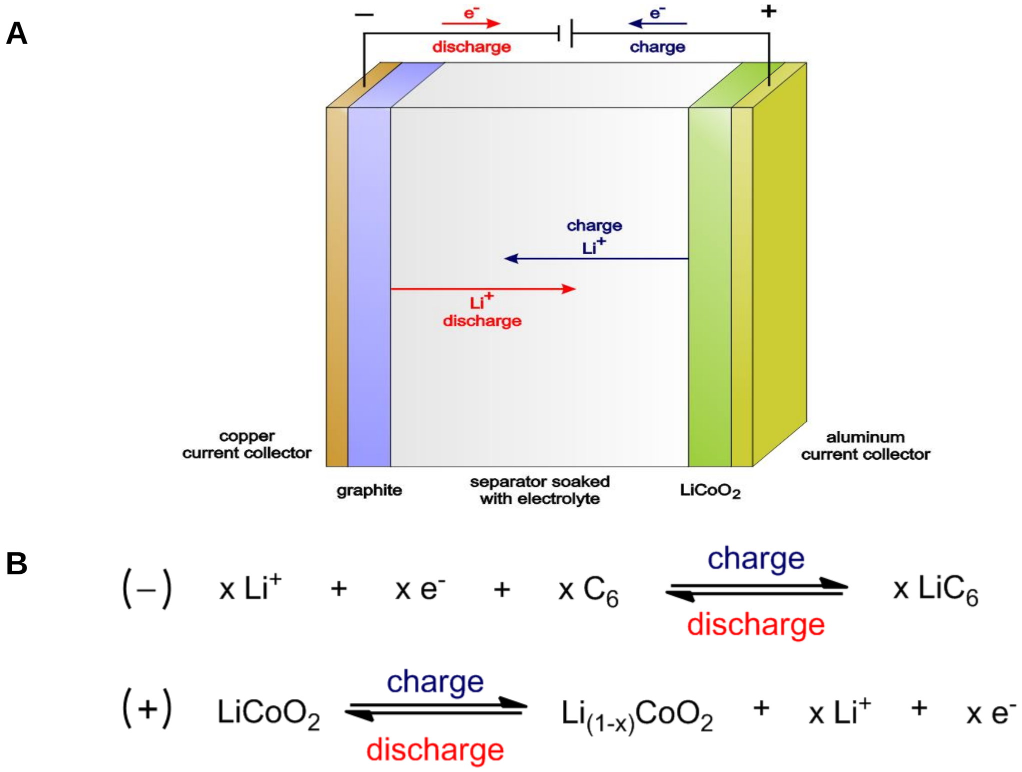

Figure 8: (A) Rechargeable lithium-ion battery based on graphite (negative electrode) and $LiCoO_2$ (positive electrode) with (B) the respective electrochemical reactions occurring during charge and discharge

In this work, promising electrode materials, namely lithium titanate ($Li_4Ti_5O_{12}$), cobalt diantimonide ($CoSb_2$) and cobalt triantimonide ($CoSb_3$), were investigated for application in low-voltage rechargeable lithium-ion batteries. A low-voltage battery system was chosen since the minimal voltage required for charging the battery in the integrated power pack is limited by the voltage supplied by the photovoltaic system upon illumination.

Lithium titanate is generally considered as a promising anode material because of a high theoretical specific capacity (175 mAh/g), a good cycling behavior with high reversible Li ion insertion/extraction, structural stability upon lithiation/de-lithiation processes (zero-strain insertion), a high charge-discharge rate capability, and a stable voltage plateau at about 1.55 V vs. Li/Li^+.[48–53] However, in this low-voltage battery application, lithium titanate was used as a positive electrode active material (cathode) since its electrochemical Li^+ insertion reaction occurs at a higher potential than for the Co-Sb alloys that were consequently used in their usual role, i.e. negative electrode active materials (anode).

Co-Sb intermetallic compounds are potential alternative anode materials for rechargeable lithium-ion batteries. Cobalt antimonides show a good electrochemical performance, improved theoretical capacities compared to graphite, flat voltage plateaus, a good cycling stability, and less volume change problems compared to pure antimony.[54,55] $CoSb_2$ is a transition metal dipnictide with arsenopyrite structure with semiconducting and non-magnetic behavior.[56] $CoSb_3$ is a transition metal tripnictide with skutterudite structure, derived from the ABX_3 perovskite structure.[57]

Lithium titanate, cobalt diantimonide and cobalt triantimonide were used as electro-active material for the preparation of composite electrodes, which were electrochemically characterized in half- and full-cell configuration via cyclic voltammetry (CV), galvanostatic cycling with potential limitation (GCPL), galvanostatic intermittent titration technique (GITT), and potentio electrochemical impedance spectroscopy (PEIS). Moreover, the chemical diffusion coefficient of Li^+ in the composite electrodes was determined from CV (Randles-Sevcik), PEIS (Warburg diffusion element), and GITT (Weppner-Huggins) measurements.

2 Results and Discussion

An integrated solar battery hybrid device was fabricated by combining an organic photovoltaic with a battery system in a three-terminal assembly with two positive and a shared negative electrode. For this purpose, bulk-heterojunction (BHJ) solar cells and electrode materials for lithium-ion batteries were prepared and characterized, followed by assembling and testing of the integrated power pack.

2.1 Bulk-Heterojunction Solar Cells

2.1.1 Single-Junction Solar Cells

In general, single-junction solar cells in normal device architecture were prepared for the application as photovoltaic system in integrated solar battery hybrid devices. For this purpose, BHJ solar cells were made on glass substrates coated with an indium tin oxide (ITO) layer as transparent anode. A hole-transport layer consisting of molybdenum(VI) oxide (MoO_3) was thermally deposited onto pre-cleaned and oxygen plasma etched substrates via physical vapor deposition (PVD). The transition metal oxide was chosen as a water-free alternative material with hole-transport properties as it is reported to effectively replace poly(3,4-ethylenedioxythiophene) polystyrene sulfonate (PEDOT:PSS) in organic solar cells.[58] This is important for safety reasons since even minor traces of water contaminations might react tremendously with the lithium-ion battery in the solar battery hybrid device. For BHJ solar cells, a blend of a conjugated polymer and a fullerene derivative serving as donor and acceptor material was doctor bladed onto the MoO_3 layer forming an interpenetrating network. The cathode comprising a titanium interfacial layer and copper top electrode was thermally deposited onto the active layer, finally obtaining single-junction solar cells. A detailed description of the device fabrication is given in Chapter 3.2. A graphical representation of the examined single-junction solar cells in normal device architecture is shown in Figure 9.

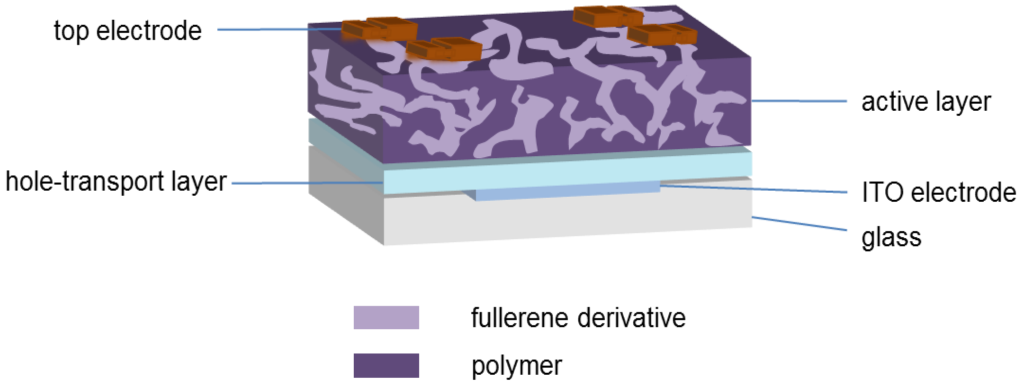

Figure 9: Bulk-heterojunction solar cells comprising a polymer:fullerene derivative blend as active layer in normal device architecture

Different conjugated polymers blended with fullerene derivatives were evaluated for the application in BHJ solar cells aiming at a good cell performance. In particular, a high voltage, current density and power conversion efficiency are essential for the overall performance (conversion and storage efficiency) of the solar battery hybrid device. This implies that a voltage exceeding 1.15 V should be supplied by the solar cell in order to charge the integrated electrochemical energy storage device. For optimization of the solar cell performance, the effect of the donor:acceptor ratio, the hole-transport layer thickness, the solvent for solution processing and thermal annealing on the characteristic parameters was investigated.

2.1.1.1 Evaluation of Donor and Acceptor Materials

Blends of various donor and acceptor materials were evaluated with regard to their performance in single-junction solar cells. In detail, benzothiadiazole-based small band gap polymers with carbazole (PCDTBT), sila-fluorene (PSiF-DBT) and cyclopenta[2,1-b:3,4-b’]dithiophene (PCPDTBT) moieties, and the polyfluorene-based wide band gap polymer F8T2 were used as donor materials.[59] The acceptor materials were based on various fullerene derivatives including [60]PCBM, [70]PCBM and ICBA. The chemical structures of the investigated donor and acceptor materials are shown in Figure 10.

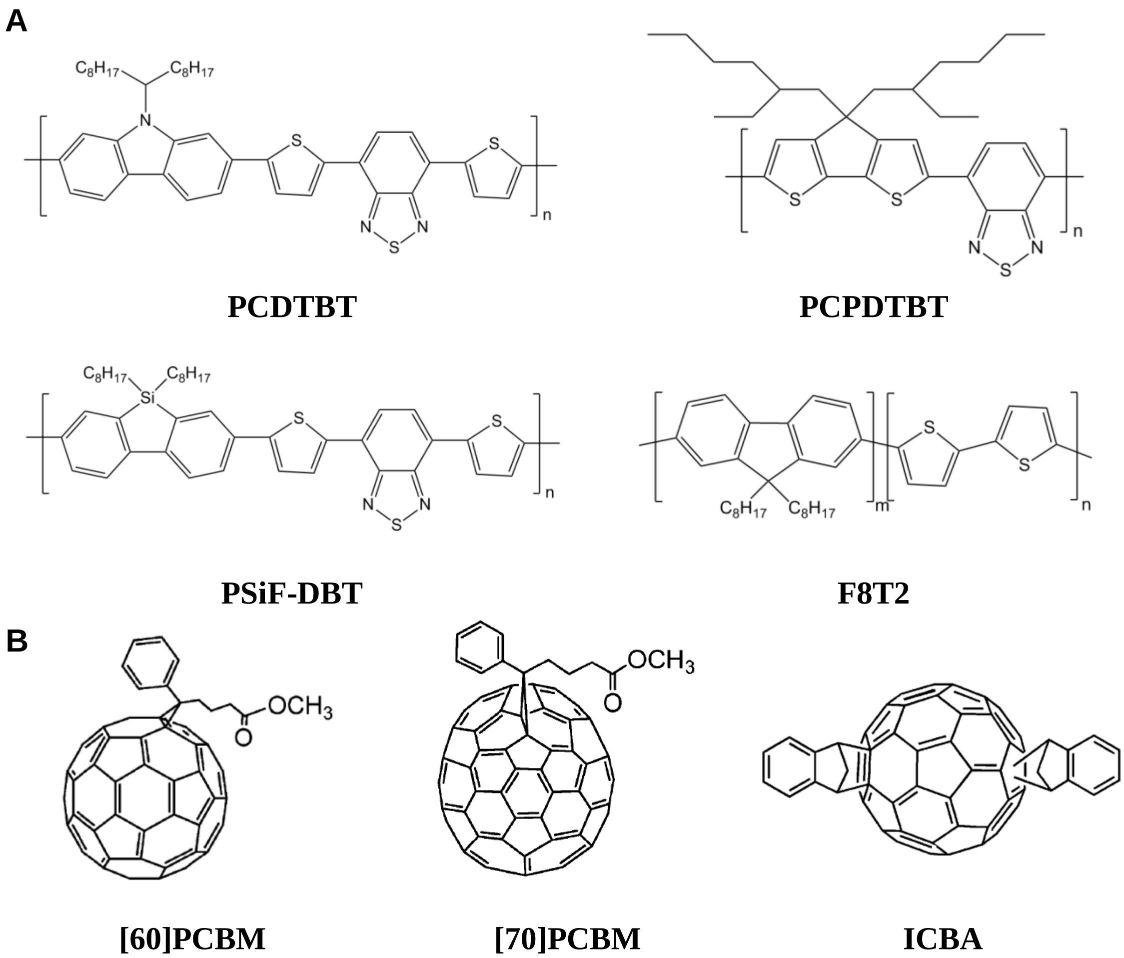

Figure 10: Chemical structures of evaluated (A) donor and (B) acceptor materials[60,61]

For evaluation of donor and acceptor materials, BHJ solar cells were fabricated in normal device architecture using a MoO_3 hole-transport layer, a polymer:fullerene derivative blend as active layer, a titanium interfacial layer and a copper top electrode.

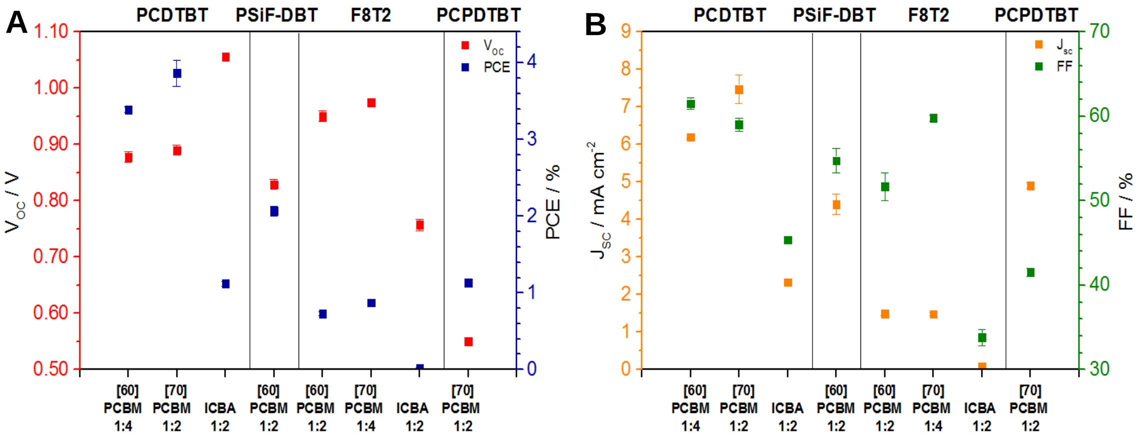

Figure 11: (A) Open circuit voltage and power conversion efficiency, and (B) short-circuit current density and fill factor of blends of different conjugated polymers and fullerene derivatives with varying donor:acceptor ratios. Characteristic parameters were averaged over five solar cells.

Figure 11 shows characteristic device parameters of the investigated BHJ solar cells comprising different donor and acceptor materials with varying ratios. Comparing the device performance of the BHJ solar cells, PCPDTBT:[70]PCBM solar cells exhibited both a poor PCE (1.13±0.02%) and V_{OC} (0.55 V), which is too low for the application in solar battery hybrid devices. Both F8T2:PCBM-based solar cells showed an improved V_{OC} exceeding 0.95 V compared to the PCPDTBT system but facing lower PCE-values (below 0.9%), which is due to a decline in J_{SC} (below 1.5 mA/cm^2). Even worse performance parameters were obtained when using ICBA as fullerene derivative. PSiF-DBT:[60]PCBM solar cells exhibited rather moderate cell characteristics with a PCE of 2.1±0.1% but exceeding those of the PCPDTBT and F8T2 counterparts. PCDTBT:ICBA solar cells showed an extremely high V_{OC} (1.06 V) as well but facing low J_{SC}s and thus low PCE-values. By substituting ICBA with [60]PCBM or [70]PCBM using PCDTBT as donor, improved characteristics compared to the other examined donor:acceptor blends were obtained. The PCE-values (over 3.3%) in particular exceeded the efficiencies of the other blends, which is due to relatively high V_{OC}s (about 0.9 V), FFs (about 60%), and improved J_{SC}s (over 6 mA/cm^2). Representative J-V curves of BHJ solar cells of the examined donor:acceptor blends are shown in Figure 12.

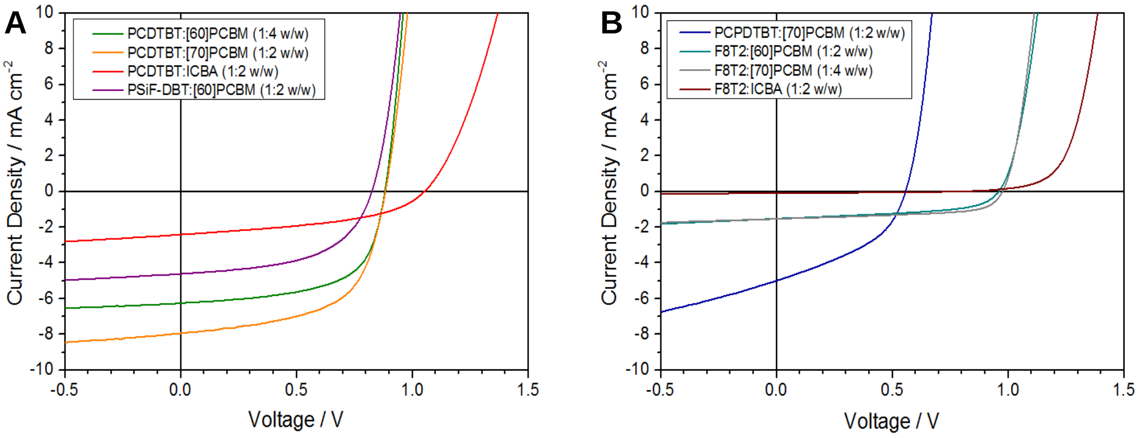

Figure 12: J-V curves of BHJ solar cells comprising different donor:acceptor materials

PCDTBT:[60]PCBM and PCDTBT:[70]PCBM solar cells showed an improved device performance compared to the other examined blends. Hence, PCDTBT was used as standard donor material for further optimization experiments. These included an evaluation of diverse fullerene-based acceptor materials and investigation of the effect of the donor:acceptor ratio, for instance.

2.1.1.2 PCDTBT:Fullerene Derivative as Active Layer in BHJ Solar Cells

For optimization of the performance of BHJ solar cells, the donor material PCDTBT was mixed with different fullerene derivatives ([60]PCBM, [70]PCBM, ICBA) in varying donor:acceptor ratios (1:1 w/w, 1:2 w/w, 1:4 w/w). A graphical representation of the characteristic parameters is given in Figure 13.

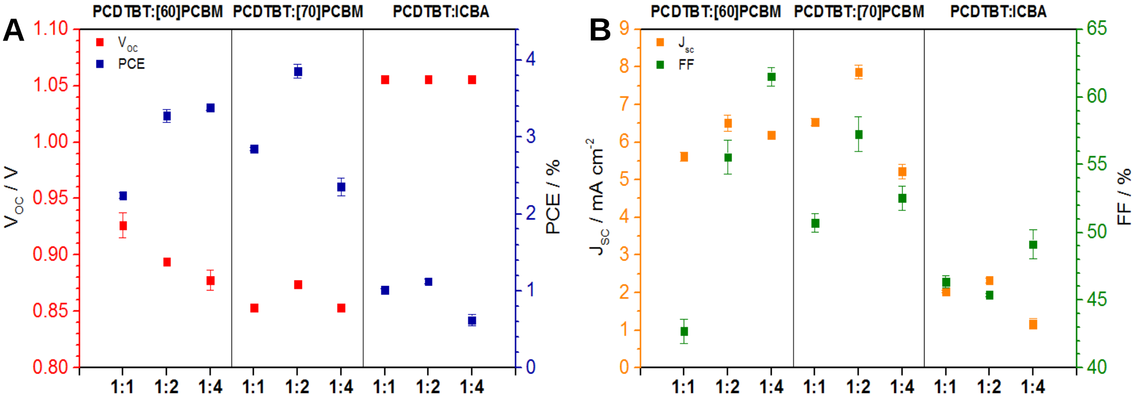

Figure 13: (A) Open circuit voltage and power conversion efficiency, and (B) short-circuit current density and fill factor of PCDTBT:fullerene derivative BHJ solar cells with varying donor:acceptor ratios. Characteristic parameters were averaged over five solar cells.

Comparing the device performance of BHJ solar cells comprising different donor:acceptor blends, PCDTBT:[60]PCBM solar cells exhibited a slight decline in V_{OC} when reducing the donor:acceptor ratio accompanied with a significant increase in FF. Hence, the device performance was improved by using higher amounts of acceptor material giving an optimum in the range studied at 1:4 (w/w) with a PCE of 3.39±0.04%. PCDTBT:[70]PCBM solar cells showed an improved performance when reducing the donor:acceptor ratio from 1:1 (w/w) to 1:2 (w/w), followed by a decline at higher amounts of the acceptor material. This trend was valid for all investigated characteristic parameters. Thus, the optimum donor:acceptor ratio for PCDTBT:[70]PCBM solar cells was determined to be 1:2 (w/w) with a PCE of 3.86±0.09%. PCDTBT:ICBA solar cells displayed a relative constant V_{OC} over all examined donor:acceptor ratios but an optimum in J_{SC} and PCE at a ratio of 1:2 (w/w) with a PCE of 1.12±0.03%.

With regard to the different fullerene derivatives, PCDTBT:ICBA solar cells exhibited higher V_{OC}s but also relatively low J_{SC}s and PCE-values compared to PCBM-based solar cells. Using [60]PCBM as fullerene derivative, improved J_{SC}s and FFs at lower donor:acceptor ratios were obtained resulting in higher efficiencies. By substituting [60]PCBM with [70]PCBM, slightly lower V_{OC}s but also higher J_{SC}s especially at higher polymer:fullerene derivative ratios were obtained. This is based on the higher optical absorption of [70]PCBM in the visible range of the electromagnetic spectrum compared to [60]PCBM resulting in an improved photon harvesting, which is supported by the PCDTBT:fullerene derivative absorption spectra shown in Figure 14.[62] This implies that the absorption range can be extended compared to pristine polymer thin films by blending fullerene-based acceptor materials to the polymer solution prior to the casting process. However, the difference in V_{OC} between ICBA- and PCBM-based solar cells is due to a shift of the LUMO energy level of ICBA relative to [60]PCBM and [70]PCBM.[63] ICBA (-3.74 eV)[64] has a higher LUMO energy level compared to [60]PCBM (-3.91 eV)[63,64] and [70]PCBM (-3.91 eV)[63] resulting in a higher difference between the HOMO energy level of the donor and the LUMO energy level the acceptor. As a consequence, an enhanced V_{OC} can be proposed for PCDTBT:ICBA solar cells, which is supported by the experimental data.

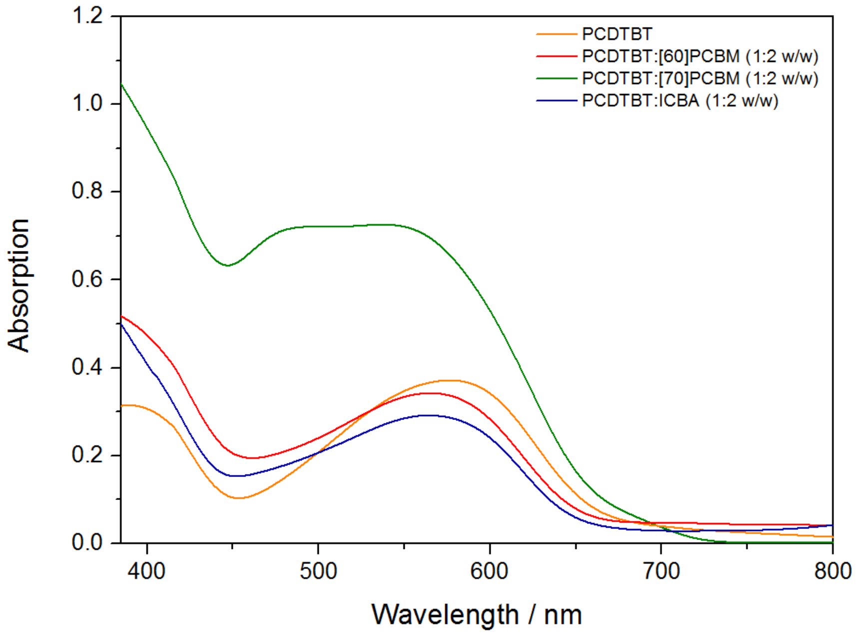

Figure 14: Absorption spectra of PCDTBT and PCDTBT:fullerene derivative thin films

By variation of the donor:acceptor ratio in PCDTBT:[70]PCBM-based BHJ solar cells, the best performance was obtained when using a donor:acceptor ratio of 1:2 (w/w). For a 1:4 (w/w) and a 1:1 (w/w) ratio, an increase in the series resistance R_s and a decrease in the fill factor were observed. For example, PCDTBT:[70]PCBM solar cells with a donor:acceptor ratio of 1:2 (w/w) had a series resistance of 16.1±1.7 Ω cm^2 compared to 24.3±2.2 Ω cm^2 for a ratio of 1:1 (w/w) and 21.2±1.2 Ω cm^2 for 1:4 (w/w). This increase in the R_s-value and decrease in FF is based on an inappropriate alignment of the donor and acceptor phases within the interpenetrating network of the active layer. Hence, the formation of a percolation network with an increasing number of charge-trapping sites or a lack of acceptor domains for the formation of proper percolation pathways can be proposed.[65] This problem can be overcome by modifying the film morphology of the active layer to obtain better-connected percolation networks, for example via changing the solvent for solution processing as reported by Park et al..[65] This is important since charge carriers need to be transported to the respective electrodes via these percolation pathways.[65]

The J-V curves of the best solar cell for each PCDTBT:fullerene derivative blend with its optimal donor:acceptor ratio and for PCDTBT:[70]PCBM solar cells with varying donor:acceptor ratios are represented in Figure 15.

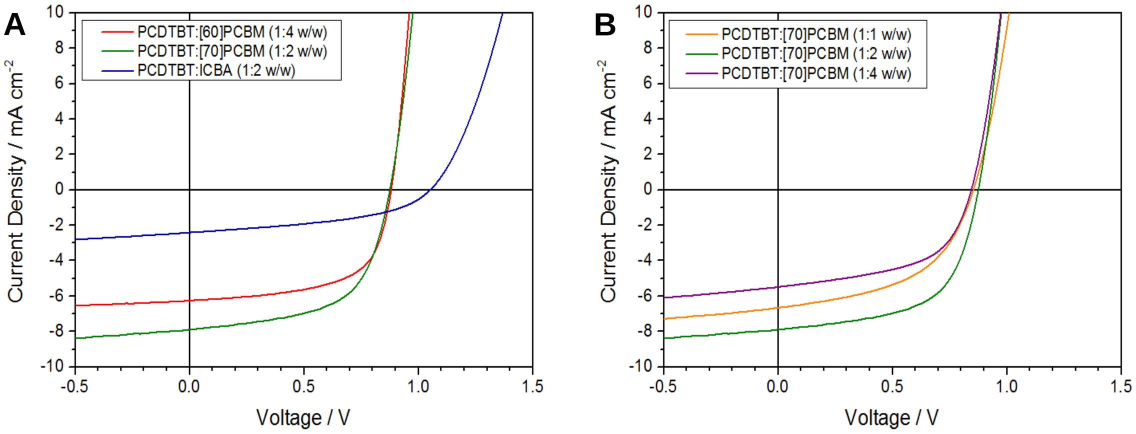

Figure 15: J-V curves of (A) PCDTBT:fullerene derivative BHJ solar cells with the optimal donor:acceptor ratio and (B) PCDTBT:[70]PCBM BHJ solar cells with varying donor:acceptor ratio

As a result, PCDTBT:[70]PCBM solar cells with a donor:acceptor ratio of 1:2 (w/w) were determined to show the best device performance giving a V_{OC} of 0.87 V, a J_{SC} of 7.86±0.18 mA/cm^2, a FF of 57.3±1.3%, and a PCE of 3.86±0.09%. Hence, this system was used for subsequent optimization experiments, for instance concerning a variation of the hole-transport layer thickness.

2.1.1.3 PCDTBT:[70]PCBM Single-Junction Solar Cells

According to Shrotriya et al., MoO_3 is an efficient hole-transport layer able to effectively substitute PEDOT:PSS in polymer solar cells.[58] The transition metal oxide layer was thermally deposited providing a water-free system, which is important for the integrated power pack presented. For optimization of PCDTBT:[70]PCBM (1:2 w/w) single-junction solar cells, the MoO_3 layer thickness was varied in the range of 5-20 nm. The respective characteristic parameters are represented in Figure 16.

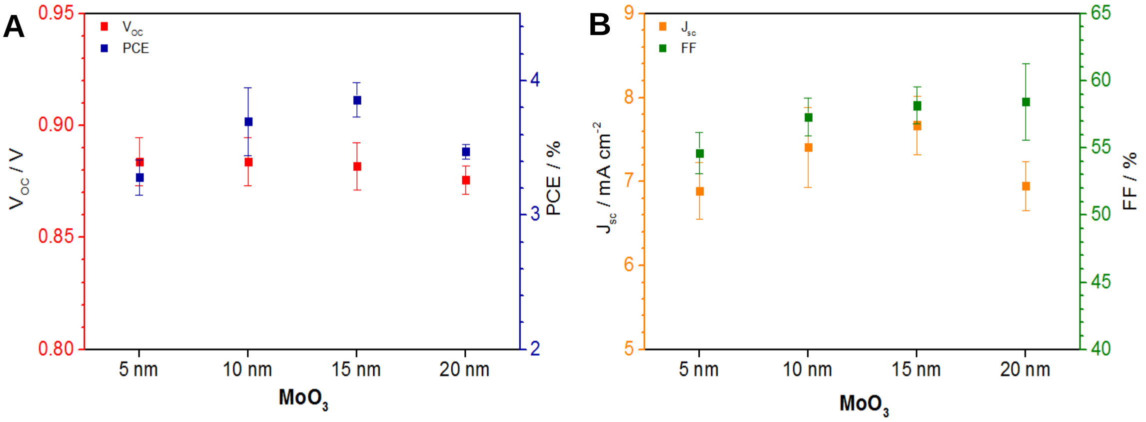

Figure 16: (A) Open circuit voltage and power conversion efficiency, and (B) short-circuit current density and fill factor of PCDTBT:[70]PCBM (1:2 w/w) BHJ solar cells with varying MoO_3 layer thicknesses. Characteristic parameters were averaged over five solar cells.

For the examined PCDTBT:[70]PCBM (1:2 w/w) solar cells, a variation in the MoO_3 layer thickness did not greatly affect the V_{OC} but a significant improvement in the J_{SC} and hence in the PCE were obtained when increasing the hole-transport layer thickness from 5 nm to 15 nm. A further increase of the MoO_3 layer thickness leaded to a decline in the device performance. This corresponds to the determined R_s-values, where a minimum series resistance of 15.6±1.5 $\Omega\ cm^2$ was found for solar cells with a 15 nm MoO_3 layer. Hence, the optimal MoO_3 layer thickness was determined to be 15 nm giving following average characteristic parameters: a V_{OC} of 0.88±0.01 V, a J_{SC} of 7.67±0.35 mA/cm^2, a FF of 58.2±1.4%, and a PCE of 3.86±0.13%.

In addition to the hole-transport layer thickness, the morphology of the active layer greatly influences the device performance of BHJ solar cells.[65] The film morphology is reported to be affected by various processing parameters including donor:acceptor ratios, solvents and thermal annealing for example.[23,65–68] Considering the effect of organic solvents on the solar cell characteristics, chlorobenzene (CB) and 1,2-dichlorobenzene (DCB) were used as solvents for the PCDTBT:[70]PCBM blend. The donor:acceptor mixture was doctor bladed at different temperatures (40°C and 60°C) for the preparation of BHJ solar cells comprising a MoO_3 hole-transport layer (15 nm and 10 nm for DCB/40°C) and Ti/Cu electrodes. The corresponding characteristic parameters are shown Figure 17.

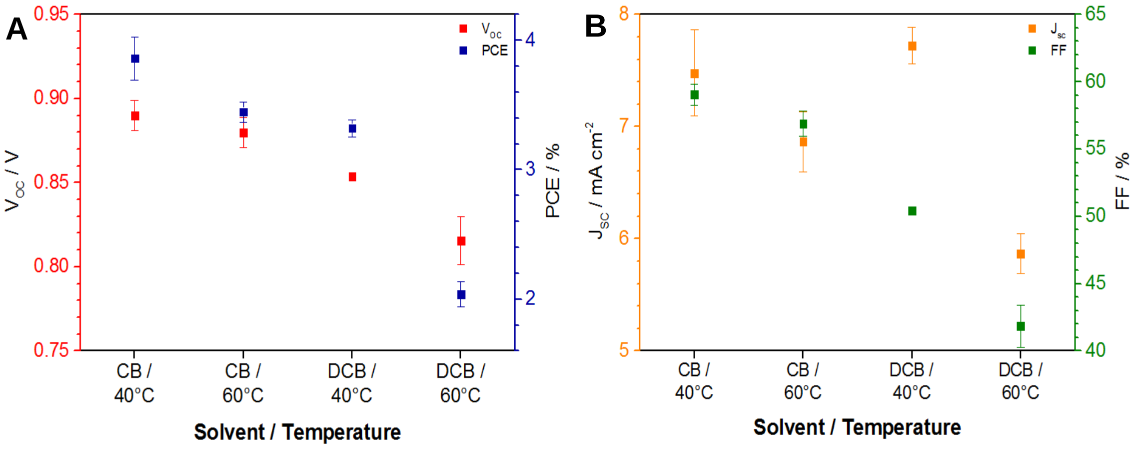

Figure 17: (A) Open circuit voltage and power conversion efficiency, and (B) short-circuit current density and fill factor of PCDTBT:[70]PCBM (1:2 w/w) BHJ solar cells doctor bladed at 40°C / 60°C from different solvents (layer thickness approx. 80 nm). Characteristic parameters were averaged over five solar cells.

Using CB as solvent for the PCDTBT:[70]PCBM blend, an increase in the blading temperature from 40°C to 60°C leaded to a decline in the J_{SC} and FF accompanied by a decline in the efficiency from 3.86±0.17% to 3.45±0.08%, whereas the V_{OC} only slightly decreased. This positive effect of lower blading temperatures might be due to an improved film morphology based on a slower evaporation of the solvent. A well-connected percolation network of donor and acceptor domains within the photo-active layer can be proposed resulting in an enhanced J_{SC} and FF as well as a reduced R_s-value.[65] By substituting CB with DCB (40°C) a further decrease in the device characteristics was ascertainable. Again, increasing the blading temperature from 40°C to 60°C (DCB) had a negative effect on the device performance. The decrease in FF and increase in R_s from CB/40°C to DCB/60°C (from $15.1 \pm 1.4\ \Omega\ \mathrm{cm}^2$ to $45.1 \pm 7.0\ \Omega\ \mathrm{cm}^2$) might be caused by an increased number of charge-trapping sites in the percolation network. Comparing these results with the literature, an improved device performance was reported when using DCB as solvent for the PCDTBT:[70]PCBM blend based on a smaller nanoscale phase separation of donor and acceptor domains.[65] Especially for lower blend ratios (1:4 w/w), the emergence of fibrillary polymer nanostructures was reported resulting in prevalent and well-connected percolated networks.[65] The choice of the deposition method of the active layer probably caused the difference between the experimental results presented (doctor blading) and the data reported in the literature (spin coating). Nevertheless, CB was used as solvent for the PCDTBT:[70]PCBM blend and the temperature for doctor blading was chosen to be 40°C.

Considering the effect of thermal annealing on the device performance, PCDTBT:[70]PCBM (1:2 w/w) BHJ solar cells comprising MoO_3 as hole-transport layer (10 nm) and Ti/Cu electrodes were thermally annealed at several stages of processing in order to investigate the effect of heat treatment on the solar cell performance.

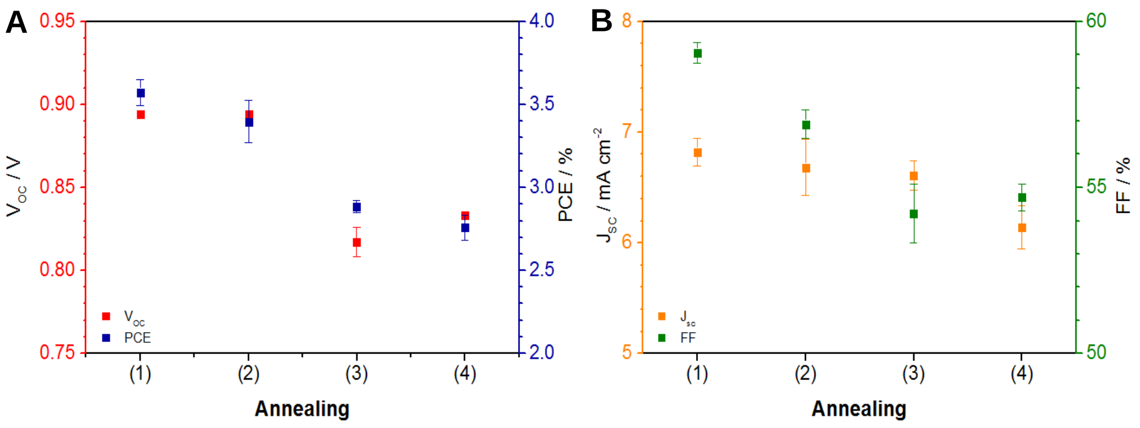

Figure 18: (A) Open circuit voltage and power conversion efficiency, and (B) short-circuit current density and fill factor of PCDTBT:[70]PCBM (1:2 w/w) BHJ solar cells (layer thickness approx. 90 nm) with different thermal annealing procedures: (1) no annealing, (2) annealing before electrode deposition (100°C, 10 min, 15 K/min), (3) annealing after electrode deposition (100°C, 30 min, 15 K/min), (4) annealing before and after electrode deposition (100°C, 10 min, 15 K/min; 100°C, 30 min, 15 K/min). Characteristic parameters were averaged over five solar cells.

Figure 18 shows that the best device performance was obtained without thermal annealing. Annealing of the active layer after doctor blading leaded to a slight decline in the performance. In contrast, when annealing BHJ solar cells after deposition of the top electrodes, a significant decline of the device characteristics was observable. Thermal annealing before and after the deposition of the top electrode also had a negative impact on the performance. Comparing the different annealing procedures, by increasing the duration of heat treatment a decrease in device performance was noticed, which was valid for all examined characteristic parameters. With ongoing heat treatment (from (1) to (4)), a decline in the FF and an increase in the R_s-value (from 16.8±0.7 Ω cm² to 23.7±1.8 Ω cm²) was obtained. This implies the formation of an increased number of charge-trapping sites in the percolated network. As reported in the literature, thermal annealing at elevated temperatures leaded to a decline of the device performance for PCDTBT-based solar cells.[65,68] For all further experiments, PCDTBT:[70]PCBM (1:2 w/w) BHJ solar cells were not thermally annealed but doctor bladed at 40°C for a slow evaporation of the solvent.

In conclusion, various parameters were investigated to optimize the solar cell performance. These included the evaluation of conjugated polymers and fullerene derivatives as donor and acceptor materials for the active layer, the optimization of the donor:acceptor ratio, the adjustment of the hole-transport layer thickness and the film morphology modification via solvent processing and thermal annealing. As a result, PCDTBT:[70]PCBM (1:2 w/w) solar cells with an optimized total layer thickness in the range of 90-120 nm were determined to show the best device performance of the evaluated donor:acceptor blends. However, apart from a good J_{SC} (7.67±0.35 mA/cm^2) and PCE (3.86±0.13%), the V_{OC} (0.88±0.01 V) is too low for a successful implementation as photovoltaic system in solar battery hybrid devices. Hence, a further optimization especially with regard to the voltage was necessary in order to provide a V_{OC} and a voltage at the maximum power point (V_{mpp}) exceeding 1.15 V, which should be achieved by organic multi-junction solar cells.

2.1.2 Multi-Junction Solar Cells

Organic multi-junction solar cells can be used for enhanced photo-voltage generation by stacking of solar cells via recombination layers. The open circuit voltage of multi-junction solar cells with ideal, fully-transparent intermediate layers enabling loss-free charge recombination equals the sum of the V_{OC}s of each contributing sub-cell.[34] This is why tandem and triple-junction solar cells were fabricated in normal device architecture in order to achieve a V_{OC} and V_{mpp} exceeding 1.15 V, which is necessary to charge the solar battery hybrid device.

In detail, tandem solar cells were prepared on glass substrates coated with an ITO layer serving as transparent anode, followed by thermal deposition of a MoO_3 hole-transport layer. A blend of PCDTBT:[70]PCBM (1:2 w/w) as active layer within the front cell was stacked in series with a second active layer forming the back cell of the tandem device. For this second active layer, various blends of conjugated polymers and fullerene derivatives serving as donor and acceptor materials were investigated in order to extend the absorption range and to cover the solar emission spectrum efficiently. The absorption range of tandem solar cells can be tuned by using donor (e.g. wide and small band gap polymers) and acceptor materials with complementary absorption behavior exhibiting absorption maxima in a different region of the electromagnetic spectrum. Thus, an enhanced light harvesting and photo-current generation can be proposed as a result of an extended absorption range. Nevertheless, according to Kirchhoff’s law the maximum short-circuit current density of multi-junction solar cells is limited by the smallest J_{SC} of each contributing sub-cell.[34] These active layers were connected in series via thermally deposited intermediate layers by physical vapor deposition. Various metals and metal oxides, in some cases modified with interfacial layers, were combined with MoO_3 serving as electron- and hole-transport layer, respectively. The cathode comprising a titanium interfacial layer and copper top electrode was thermally deposited onto the second active layer finally obtaining the multi-junction solar cell. A detailed description of the device fabrication is given in Chapter 3.2.

A graphical representation of the prepared multi-junction solar cells in normal device architecture is shown in Figure 19.

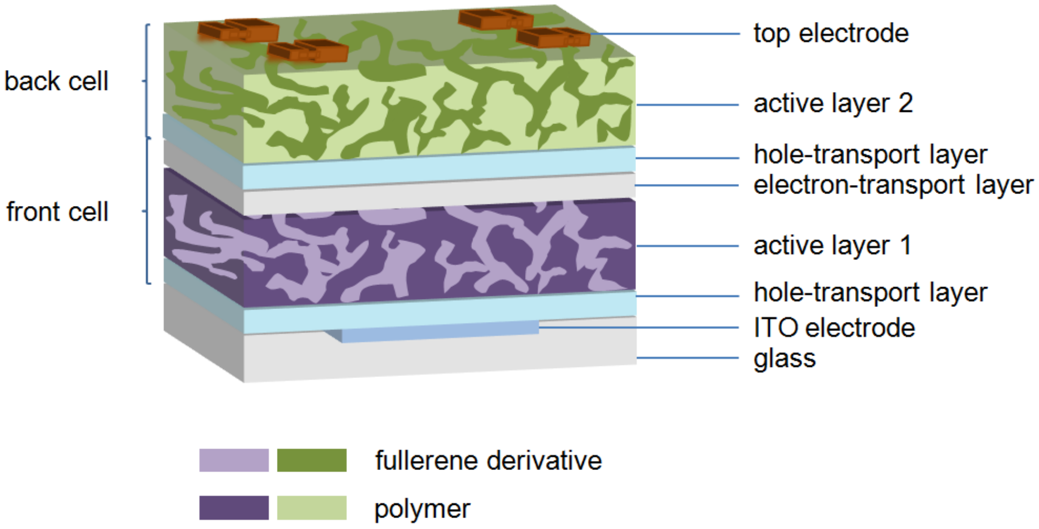

Figure 19: Multi-junction solar cells comprising two different active layers connected in series via intermediate layers in normal device architecture

2.1.2.1 Active Layers in Multi-Junction Solar Cells

Donor materials with complementary absorption region should be combined in tandem solar cells in order to enhance light harvesting. For this purpose, various conjugated polymers including the small band gap polymers PCDTBT, PSiF-DBT and PCPDTBT, and the wide band gap polymer F8T2 were examined with regard to their absorption behavior. Polymer thin films were prepared by doctor blading of a polymer solution (10 mg/mL in chlorobenzene) onto pre-cleaned microscope slides. The normalized absorption spectra of the pristine polymer thin films were recorded in the range of 385-900 nm (Figure 20).

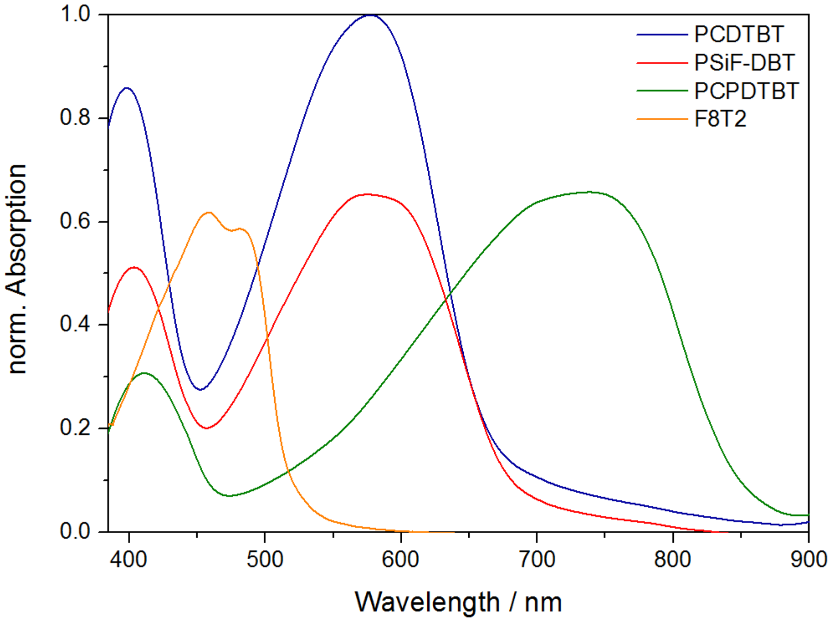

Figure 20: Absorption spectra of pristine PCDTBT, PSiF-DBT, PCPDTBT, and F8T2 thin films in the range of 385-900 nm

Comparing the absorption spectra of the examined polymers, absorption peaks at 396 nm and 578 nm were determined for PCDTBT. PSiF-DBT showed a similar absorption range compared to PCDTBT with maxima at 404 nm and 575 nm. Thus, combining these two materials in tandem solar cells would not succeed in extending the absorption range. The low band gap PCPDTBT (with peak maxima at 420 nm and 736 nm) and the wide band gap F8T2 (459 nm and 480 nm) are donor materials with an appropriate complementary absorption region. Because of the poor device performance of F8T2:fullerene derivative BHJ solar cells, only the benzothiadiazole-based polymers were used as donor materials in tandem solar cells.

Because of the good device performance of PCDTBT:[70]PCBM (1:2 w/w) BHJ solar cells, the PCDTBT:[70]PCBM blend was used as standard active layer for at least one sub-cell in multi-junction solar cells. Since PCDTBT (E_g = 1.88 eV[69]) has the highest band gap of the examined benzothiadiazole-based donor materials (E_g (PSiF-DBT) = 1.82 eV[70], E_g (PCPDTBT) = 1.46 eV[71]), PCDTBT:[70]PCBM was used as active layer in the front cell of multi-junction solar cells. An optimized intermediate layer combination of 1 nm Al / 15 nm MoO_3 was thermally deposited onto the first active layer.[72] For the second active layer, the different low band gap polymers blended with fullerene derivatives were doctor bladed onto the intermediate layer, followed by thermal deposition of Ti/Cu electrodes. The corresponding J-V curves and characteristic parameters are represented in Figure 21 and Table 1, respectively.

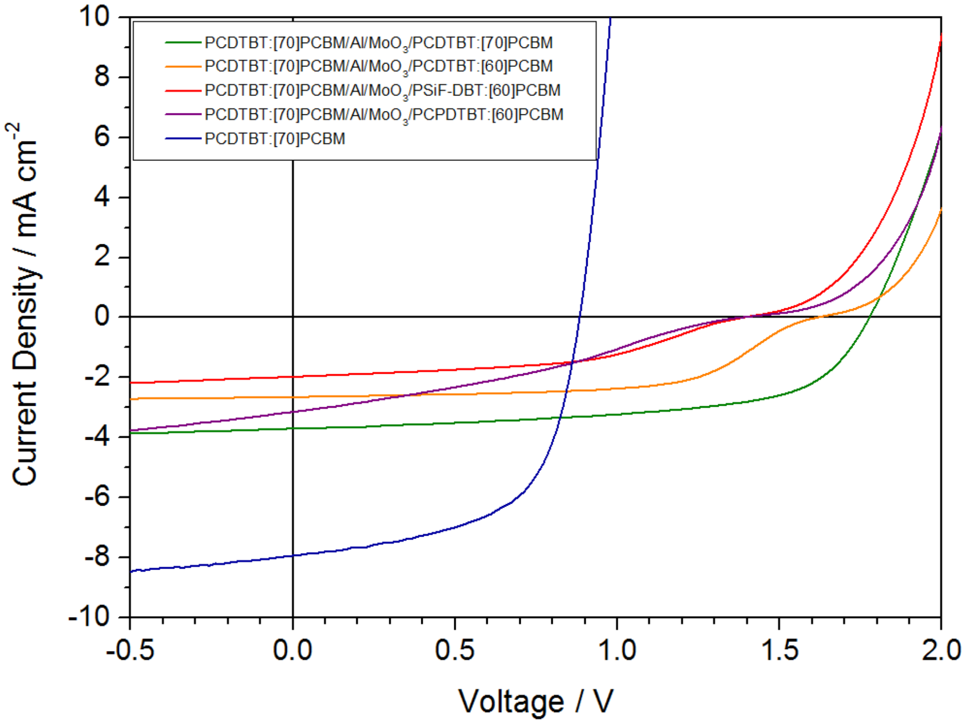

Figure 21: J-V curves of multi-junction solar cells with PCDTBT:[70]PCBM (1:2 w/w) front cells, 1 nm Al / 15 nm MoO$_3$ intermediate layers and various donor:acceptor blend back cells and of a single-junction reference cell

Table 1: Average photovoltaic performance parameters of multi-junction and single-junction reference solar cells. The general device geometry was glass / ITO / MoO$_3$ / PCDTBT:[70]PCBM (1:2 w/w) / 1 nm Al / 15 nm MoO$_3$ / active layer / Ti / Cu. Averages were taken over five solar cells. R$_s$- and R$_{sh}$-values were extracted from the respective J-V curves under illumination.

Active Layer of Back Cell	**V_{OC} [V]**	**J_{SC} [mA cm^{-2}]**	**FF [%]**	**PCE [%]**	**R_s [Ω cm^2]**	**R_{sh} [kΩ cm^2]**
PCDTBT:[70]PCBM (1:2 w/w)	1.78	3.71±0.04	58.9±0.9	3.88±0.03	50.9±5.2	4.29±0.92
PCDTBT:[60]PCBM (1:2 w/w)	1.62	2.61±0.08	57.5±3.5	2.43±0.14	483.5±62.2	2.85±1.10
PSiF-DBT:[60]PCBM (1:2 w/w)	1.40±0.01	1.91±0.05	46.4±0.4	1.26±0.03	570.6±22.4	1.58±0.32
PCPDTBT:[60]PCBM (1:2 w/w)	1.41±0.02	3.08±0.06	30.6±0.8	1.34±0.03	978.2±107.5	0.67±0.08
- (single-junction)	0.89±0.01	7.48±0.38	59.0±0.8	3.86±0.17	15.1±1.4	0.73±0.24

The best device performance was obtained using PCDTBT:[70]PCBM (1:2 w/w) in both sub-cells giving a V_{OC} of 1.78 V, a J_{SC} of 3.71±0.04 mA/cm², a FF of 58.9±0.9% and a PCE of 3.88±0.03%. Hence, the open circuit voltage reached the sum of the V_{OC}s of each contributing sub-cell. By substituting [70]PCBM with [60]PCBM in the back cell, a decline in the cell performance was determined. This improved device performance of [70]PCBM-based solar cells can be attributed to an increased fraction of absorbed light in the visible region below 650 nm of the electromagnetic spectrum compared to [60]PCBM-based systems (Figure 14).[73,74] Tandem solar cells with PSiF-DBT:[60]PCBM and PCPDTBT:[60]PCBM back cells exhibited a worse device performance with lower V_{OC}s, FFs and PCE-values compared to the PCDTBT-based systems. This decrease in the solar cell performance was also supported by the significant increase in the R_s-values.

As a result, the best device performance was obtained using PCDTBT:[70]PCBM (1:2 w/w) as active layer in both sub-cells of multi-junction solar cells with an optimized active layer thickness of about 90 nm for each sub-cell. Further optimization of the device performance of multi-junction solar cells included the investigation of the effect of various intermediate layer combinations, partially modified with interfacial layers.

2.1.2.2 Intermediate Layers in Multi-Junction Solar Cells

In general, multi-junction solar cells are prepared by stacking active layers via intermediate layers. The choice of materials for these recombination layers and their properties are crucial for the overall solar cell performance since various requirements have to be met including

(i) a high optical transparency over the absorption range of the back cell(s) in order to reduce optical losses[34]

(ii) low energy barriers for electron- and hole-extraction processes at the acceptor/electron-transport layer interface and the donor/hole-transport layer interface[72]

(iii) a high electrical conductivity and charge carrier mobility within the intermediate layers to minimize the number of occurring charge-trapping events[75]

(iv) an efficient recombination of electrons coming from one sub-cell and holes from the other at the interface of electron- and hole-transport layers within the recombination layer[4]

(v) an easy and low-cost processing method to obtain environmentally stable and robust intermediate layers with the ability of protecting prior-deposited active layers from further processing (e.g. solution processing).[34]

Taking these prerequisites into account, layers of highly optical transparent materials with electron- and hole-transport properties are stacked in series to ensure an effective recombination of electrons and holes at the interface of the electron- and hole-transport layers. These recombination layers can be either solution-processed or thermally deposited under vacuum. Solution-processed intermediate layers based on a combination of *n*-type metal oxides like TiO_x[76] or ZnO nanoparticles[77] and PEDOT:PSS serving as electron- and hole-transport layer are reported in the literature. Thermally deposited intermediate layers use combinations of metal thin films as electron-transport layer and *p*-type-like transition metal oxides such as NiO, MoO_3 or WO_3 as hole-transport layer.[72] Moreover, ultrathin metal layers of Ag[78] and Au[79] as intermediate layers have been reported but facing problems in solution-processed tandem solar cells because of dissolution effects of prior-deposited active layers.[72]

Especially for solution-processed organic multi-junction solar cells, a lack in study of metal/*p*-type like oxide intermediate layer combinations is reported.[72] This is why various metals (Al, Ag, Au, Cu, Ti) and metal oxides (TiO_x, ZnO, MoO_3) combined with the *p*-type-like transition metal oxide MoO_3 serving as electron- and hole-transport layer were investigated with regard to the influence on the device performance. Different metal (Ca, Ti) and alkali-metal compound (LiF, Cs_2CO_3) interfacial layers were thermally deposited under vacuum in order to adjust the work function of the metals for improved device performances. For investigation of these intermediate layer combinations in tandem solar cells, sub-cells with PCDTBT:[70]PCBM (1:2 w/w) active layers were connected in series via various thermally deposited recombination layers.

2.1.2.2.1 Metal/MoO_3 and Metal Oxide/MoO_3 Intermediate Layers

Metal/MoO_3 and metal oxide/MoO_3 intermediate layer combinations were tested in terms of their influence on the photovoltaic characteristic parameters in tandem solar cells. The respective J-V curves of the multi-junction solar cells and a single-junction reference cell are represented in Figure 22. The photovoltaic characteristic parameters are summarized in Table 2.

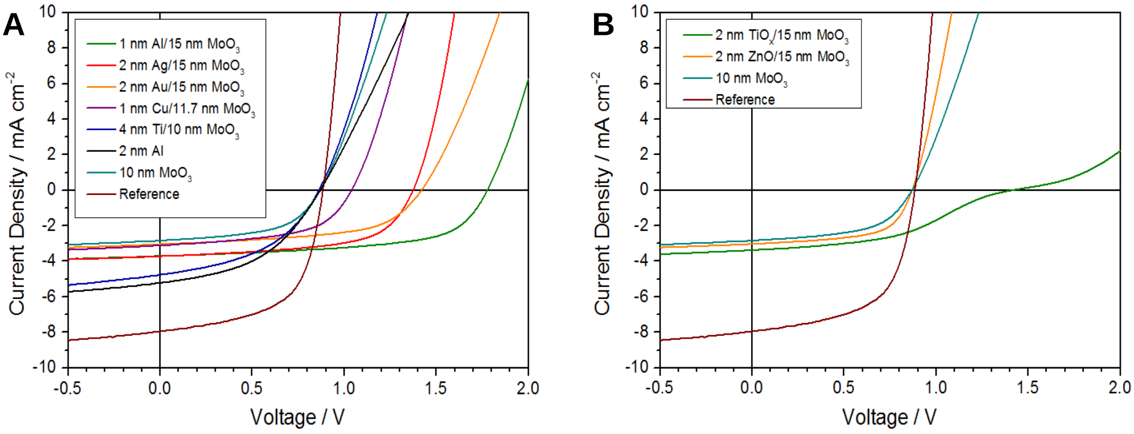

Figure 22: J-V curves of PCDTBT:[70]PCBM multi-junction solar cells with (A) metal/MoO_3 and (B) metal oxide/MoO_3 intermediate layers

Table 2: Average photovoltaic performance parameters of multi-junction solar cells with different intermediate layer combinations (metal or metal oxide/MoO_3). The general device geometry was glass / ITO / MoO_3 / PCDTBT:[70]PCBM (1:2 w/w) / intermediate layer / PCDTBT:[70]PCBM (1:2 w/w) / Ti / Cu. Averages were taken over five solar cells. R_s- and R_{sh}-values were extracted from the respective J-V curves under illumination.

Intermediate Layer	V_{OC} [V]	J_{SC} [mA cm^{-2}]	FF [%]	PCE [%]	R_s [Ω cm²]	R_{sh} [kΩ cm²]
1 nm Al/15 nm MoO_3	1.78	3.71±0.04	58.9±0.9	3.88±0.03	50.9±5.2	4.29±0.92
2 nm Ag/15 nm MoO_3	1.41±0.05	3.51±0.13	58.4±0.7	2.88±0.12	46.7±2.4	1.74±0.33
2 nm Au/15 nm MoO_3	1.41±0.01	3.01±0.01	56.8±0.1	2.44±0.02	65.8±5.9	2.82±1.52
1 nm Cu/11.7 nm MoO_3	1.06±0.03	3.00±0.09	53.9±1.1	1.71±0.04	52.9±1.7	1.80±0.33
4 nm Ti/10 nm MoO_3	0.87	4.74±0.05	44.3±0.6	1.84±0.01	51.6±1.8	0.57±0.09
2 nm TiO_x /15 nm MoO_3	1.40±0.02	3.41±0.07	41.0±1.2	1.93±0.05	626.6±118.3	1.92±0.60
2 nm ZnO/15 nm MoO_3	0.87	2.97±0.04	59.5±1.0	1.57±0.04	37.9±3.0	2.00±0.28
2 nm Al	0.87	5.30±0.19	42.8±2.4	2.03±0.08	62.7±4.3	0.63±0.03
10 nm MoO_3	0.87±0.01	2.78±0.04	54.8±0.8	1.34±0.02	56.2±1.9	1.99±0.11
- (single-junction)	0.89±0.01	7.48±0.38	59.0±0.8	3.86±0.17	15.1±1.4	0.73±0.24

The best solar cell performance of the examined multi-junction solar cells was obtained when using a 1 nm Al / 15 nm MoO_3 intermediate layer giving a V_{OC} of 1.78 V, a J_{SC} of 3.71±0.04 mA/cm², a FF of 58.9±0.9% and a PCE of 3.88±0.03%. According to Kirchhoff's law, the V_{OC} was found to be the sum of the V_{OC}s of both sub-cells. This is due to an efficient collection of charge carriers and a high optical transparency of the intermediate layer of approx. 98% from 350-900 nm.[72] The J_{SC} was found to be only half the value of the single-junction reference cell leading to a comparable FF and PCE-value. Using Ag/MoO_3 as intermediate layer a significant decline in the V_{OC} and J_{SC} was ascertainable resulting in a drop of the PCE. This decline in the J_{SC} might be due to a lower transmission of Ag/MoO_3 compared to the Al/MoO_3 intermediate layer in the visible range of the electromagnetic spectrum.[72,80] Because of this reduced light transmission, a decrease in light harvesting in the back cell and hence in photo-current generation can be proposed. In comparison to that, tandem solar cells with an Au/MoO_3 intermediate layer showed a similar V_{OC} and FF but a slightly lower J_{SC} and PCE. By substituting Au/MoO_3 with Cu/MoO_3, a similar J_{SC} and FF but a significant drop of the

V_{OC} was noticed. Tandem solar cells with a Ti/MoO_3 intermediate layer exhibited a low V_{OC} comparable to the single-junction device resulting in a poor PCE. This low open circuit voltage is based on the low shunt or parallel resistance R_{sh}. Low shunt resistances are known to reduce current flows and voltages resulting in power losses since an alternative current path is provided.[81] This might be due to problems during manufacturing. However, Ti/MoO_3 was determined to be an inadequate intermediate layer for this system, even though titanium has a similar work function (4.33 eV)[82] compared to aluminum (4.28 eV)[83] and silver (4.26 eV)[82,83]. Using an ultrathin aluminum intermediate layer (2 nm), a rather poor device performance was obtained with a V_{OC} similar to the single-junction reference cell but an improved J_{SC} compared to the other multi-junction solar cells. The low open circuit voltage is ascribable to the missing hole-transport properties of the aluminum intermediate layer responsible for non-effective electron-hole recombination. A graphical representation of the corresponding energy level diagram of PCDTBT:[70]PCBM multi-junction solar cells with metal/MoO_3 intermediate layers is given in Figure 23.

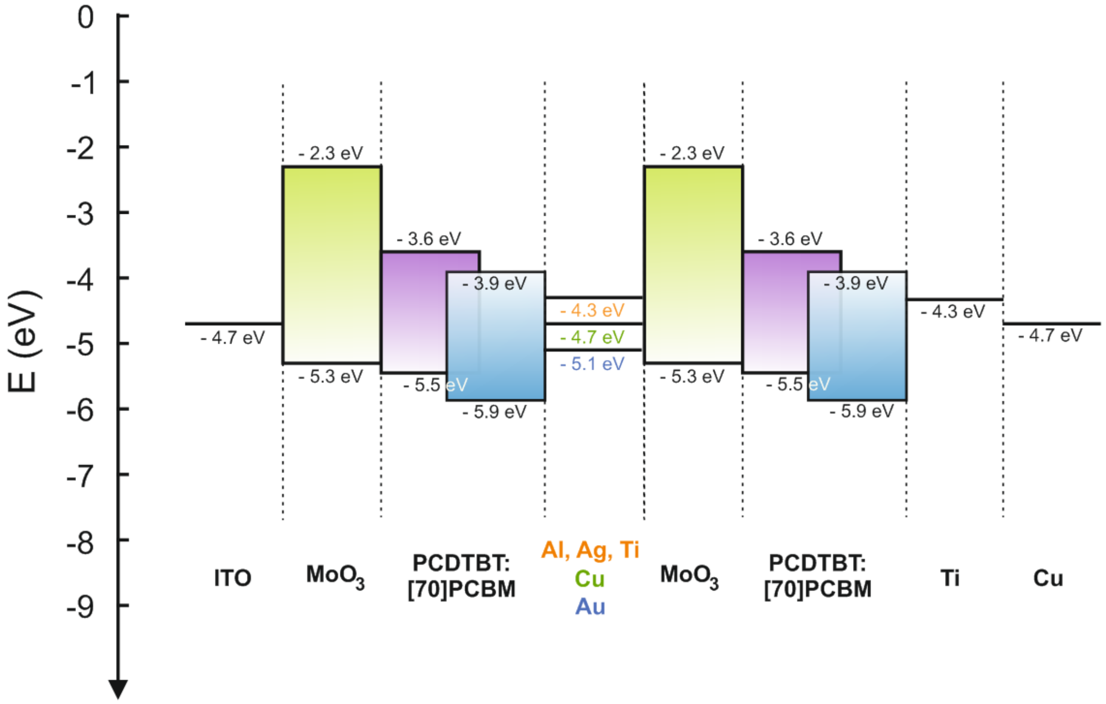

Figure 23: Energy level diagram of PCDTBT:[70]PCBM multi-junction solar cells with metal/MoO_3 intermediate layers

With regard to the metal oxide/MoO_3 recombination layers, TiO_x and ZnO were prepared by thermal evaporation of metallic Ti or Zn at a pressure of 10^{-4} mbar, followed by exposure to air during which a conversion of the metal layers to the respective metal oxides was assumed. According to the literature, titanium shows a high affinity to oxygen accompanied by the conversion into TiO_x within microseconds, whereas dense ZnO films are formed upon oxidation of Zn films under ambient air.[84,85] Comparing the device performance, only tandem solar cells with a TiO_x/MoO_3 intermediate layer showed good characteristic parameters with a high V_{OC} but exhibited s-shaped J-V curves resulting in a relative low FF and an extremely high R_s-value. These s-shaped curves are based on non-ohmic contact properties, which can be overcome by deposition of metal-based interfacial layers providing an equivalent ohmic contact between the electron- and hole-transport layer.[34,86–93] Tandem solar cells with ZnO/MoO_3 intermediate layers exhibited poor photovoltaic performance parameters, which might be due to manufacturing problems. The poor device performance of tandem solar cells with a MoO_3 intermediate layer is based on missing electron-transport properties of the transition metal oxide, which is due to its high conduction band (-2.3 eV).[58] This additional energy barrier for electron-transport processes prevents efficient electron-hole recombination within the intermediate layer. This is why photovoltaic characteristics comparable to single-junction devices were obtained. A graphical representation of the corresponding energy level diagram of PCDTBT:[70]PCBM multi-junction solar cells with metal oxide/MoO_3 intermediate layers is given in Figure 24.

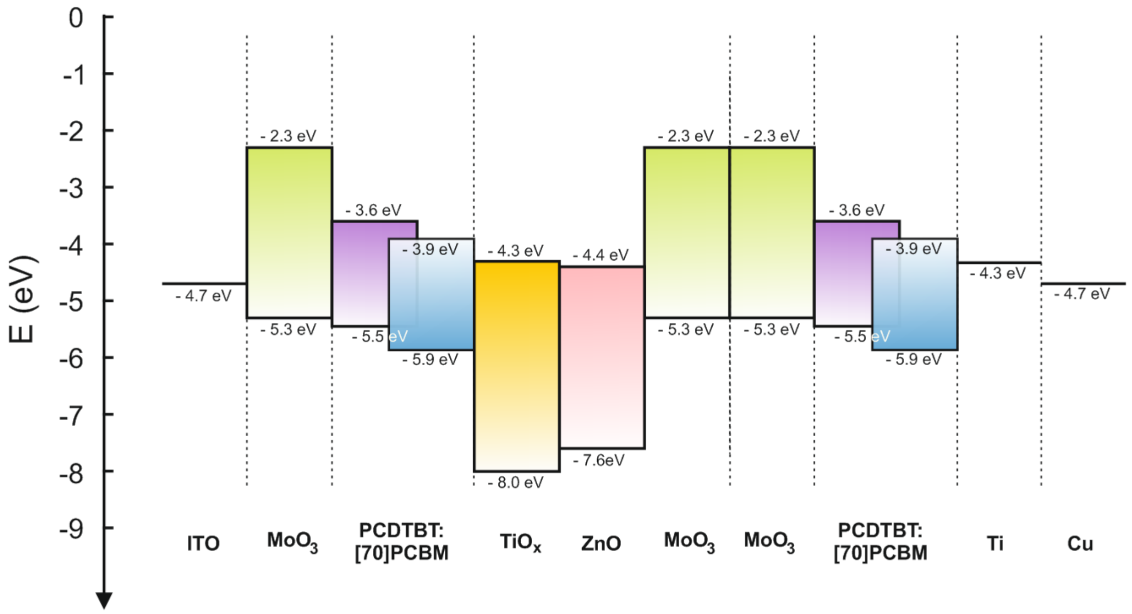

Figure 24: Energy level diagram of PCDTBT:[70]PCBM multi-junction solar cells with metal oxide/MoO_3 intermediate layers

2.1.2.2.2 Modification and Optimization of Al/MoO$_3$ Intermediate Layers in Multi-Junction Solar Cells

In order to determine the influence of additional alkali-metal compound (lithium fluoride) and metal layers (calcium) combined with Al/MoO$_3$-based intermediate layers on the device performance, multi-junction solar cells with different recombination layers were prepared including LiF/Al/MoO$_3$[72] and Ca/Al/MoO$_3$[94]. The photovoltaic characteristic parameters and J-V curves are graphically represented in Figure 25.

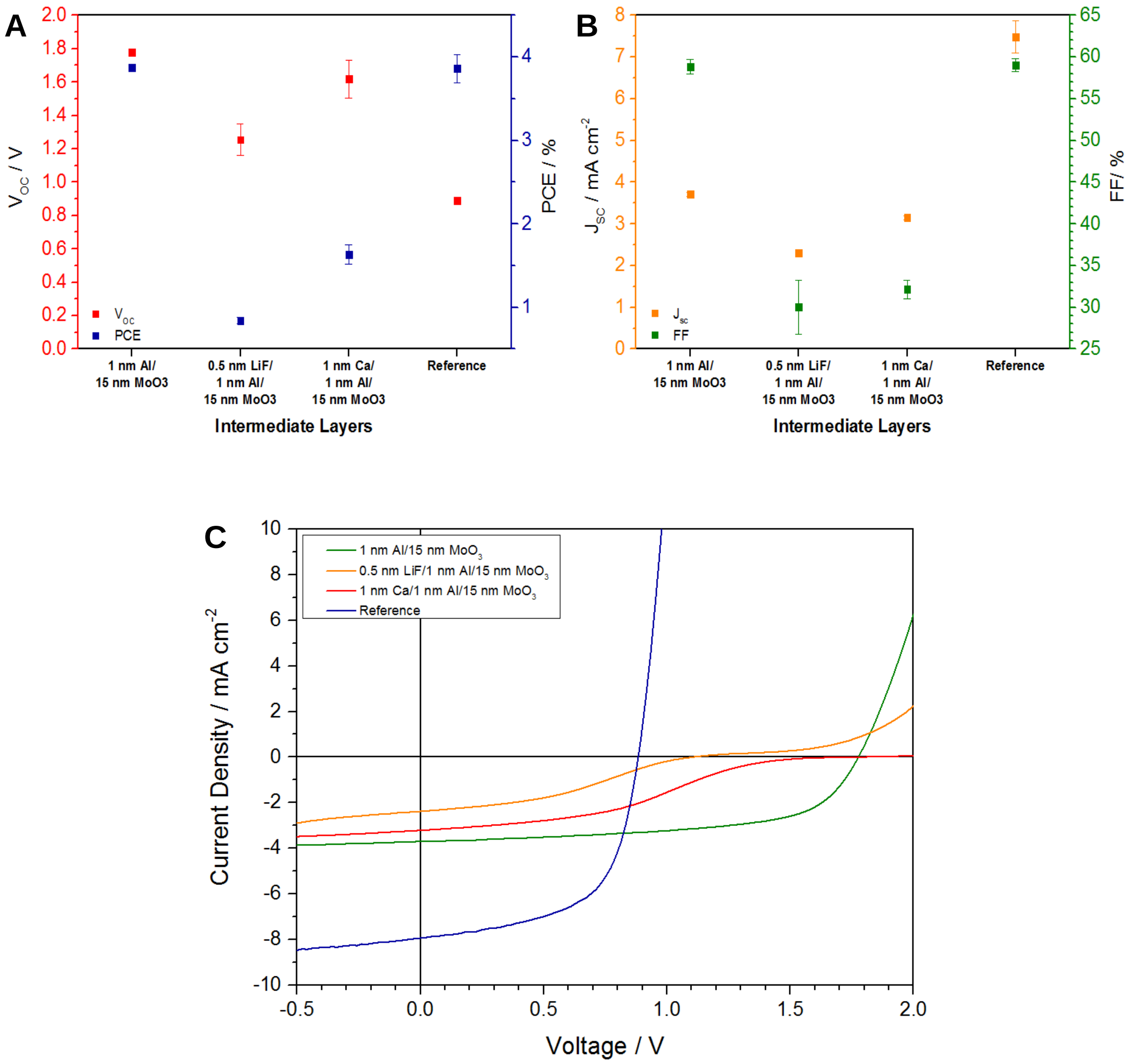

Figure 25: (A) Open circuit voltage and power conversion efficiency, (B) short-circuit current density and fill factor, and (C) J-V curves of single- and multi-junction solar cells with Al/MoO$_3$-based intermediate layers. Characteristic parameters were averaged over five solar cells.

Tandem solar cells with Al/MoO_3 recombination layers showed an improved device performance compared to other intermediate layer combinations. By inserting lithium fluoride and calcium interfacial layers, s-shaped curves were obtained yielding lower FFs (about 30%) and PCE-values. These s-shaped curves are based on non-ohmic contacts of the intermediate layer.[34,86–93] Multi-junction solar cells with a Ca/Al/MoO_3 recombination layer exhibited a higher V_{OC} (1.62±0.11V) compared to the LiF/Al/MoO_3 counterpart. Both intermediate layer combinations exhibited significant higher R_s- but lower R_{sh}-values compared to tandem solar cells with an Al/MoO_3 recombination layer. However, tandem solar cells with Al/MoO_3, LiF/Al/MoO_3 and Ca/Al/MoO_3 intermediate layer combinations showed an improved V_{OC} but also lower J_{SC}s and FFs compared to the single-junction reference cell.

Because of the good device performance of tandem solar cells with Al/MoO_3 intermediate layers, the metal and metal oxide layer thicknesses were optimized. The respective performance parameters and J-V curves are shown in Figure 26.

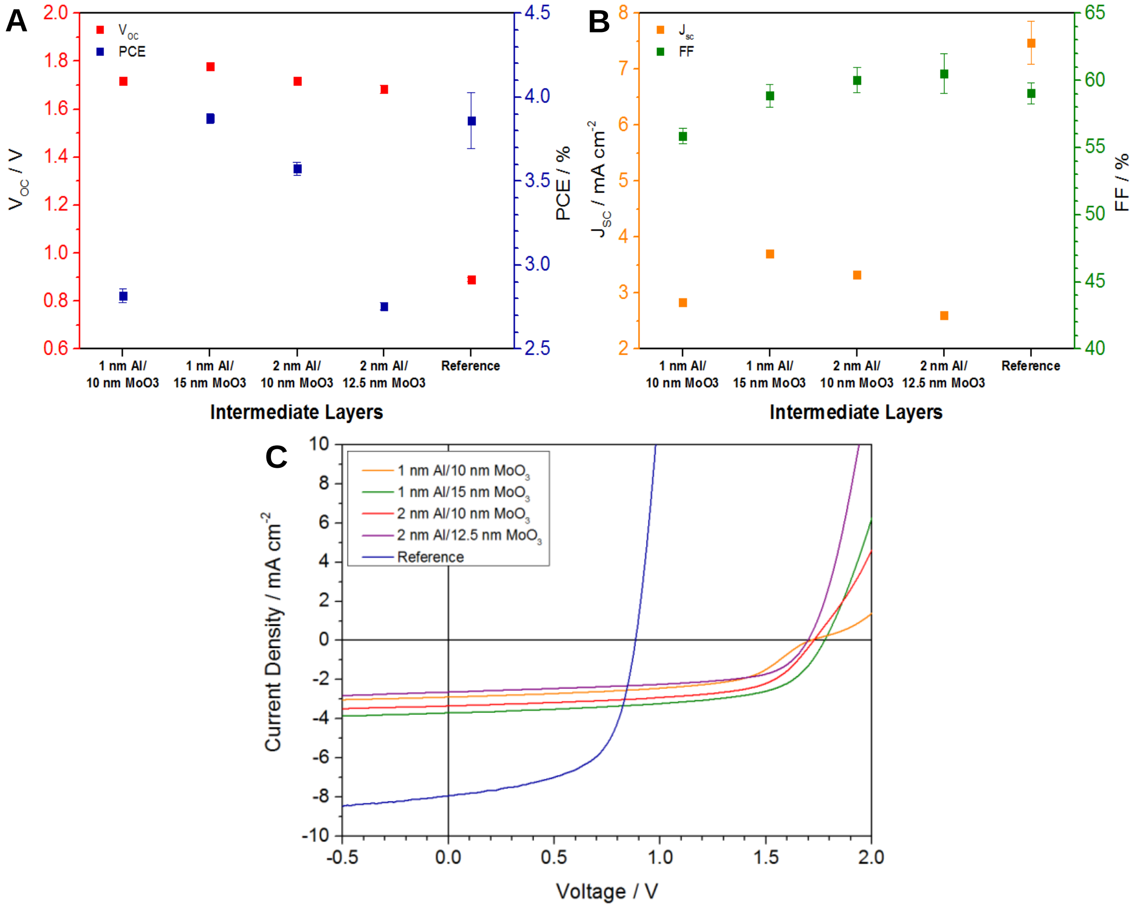

Figure 26: (A) Open circuit voltage and power conversion efficiency, (B) short-circuit current density and fill factor, and (C) J-V curves of single- and multi-junction solar cells with Al/MoO_3 intermediate layers with varying layer thicknesses. Characteristic parameters were averaged over five solar cells.

A variation of the electron- and hole-transport layer thickness did not greatly affect the V_{OC} but an optimum in J_{SC} and thus in PCE was found for 1 nm Al / 15 nm MoO_3 intermediate layers. This recombination layer yielded the lowest R_s-value and highest R_{sh}-value of the examined Al/MoO_3 combinations. This optimized intermediate layer combination was also used by Zhao et al. for solution-processed polymer tandem solar cells.[72]

2.1.2.2.3 Modification of Ag/MoO_3 Intermediate Layers in Multi-Junction Solar Cells

For optimization of PCDTBT:[70]PCBM (1:2 w/w)-based multi-junction solar cells, interfacial layers comprising calcium and cesium carbonate were combined with Ag/MoO_3 intermediate layers. Similar recombination layers in tandem solar cells have been reported in the literature such as Ca/Ag/MoO_3[94] and Cs_2CO_3/Ag/MoO_3[80].

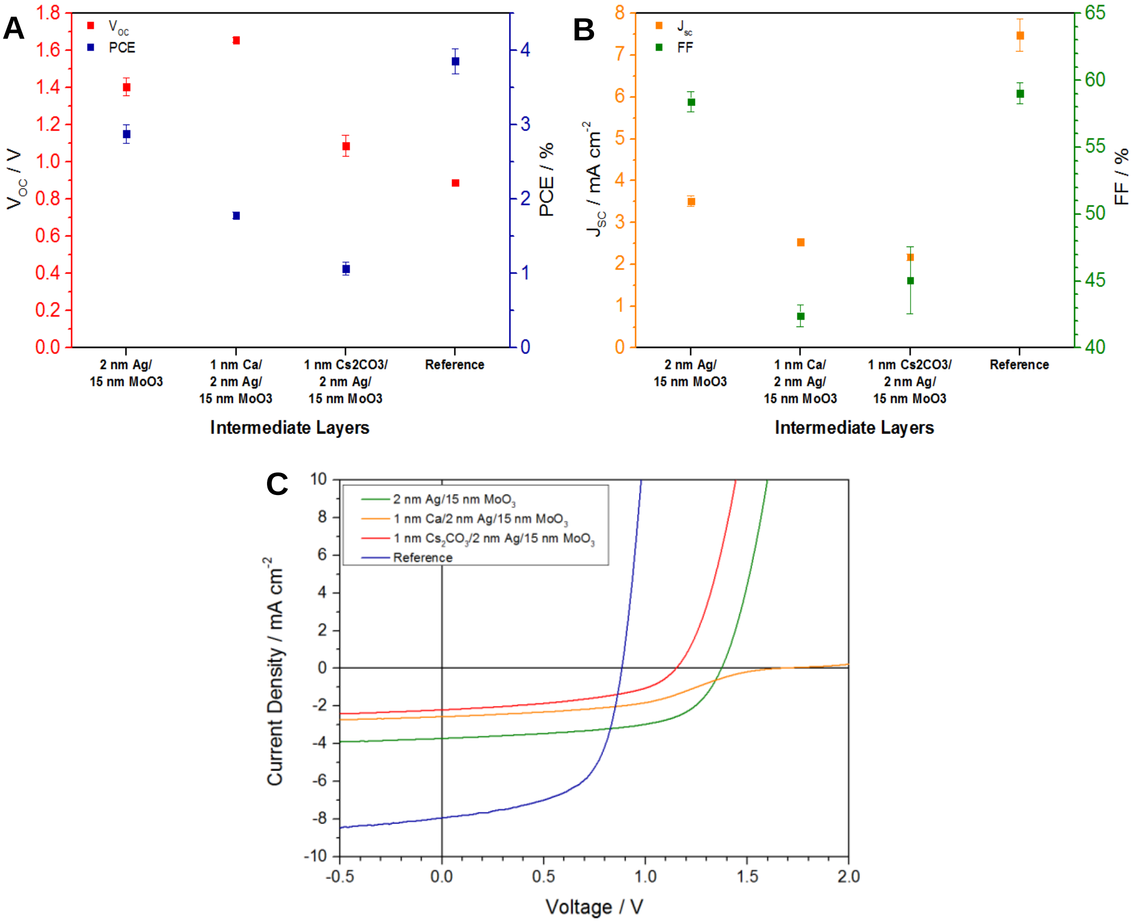

Figure 27: (A) Open circuit voltage and power conversion efficiency, (B) short-circuit current density and fill factor, and (C) J-V curves of single- and multi-junction solar cells with Ag/MoO_3 intermediate layers. Characteristic parameters were averaged over five solar cells.

Figure 27 shows the characteristic parameters as well as the J-V curves of tandem solar cells with various intermediate layer combinations. The best device performance was obtained when using an Ag/MoO_3 intermediate layer giving a V_{OC} of 1.41±0.05 V, a J_{SC} of 3.51±0.13 mA/cm^2, a FF of 58.4±0.8%, and a PCE of 2.88±0.12%. The V_{OC} was found to achieve 79% of the sum of the V_{OC}s of both sub-cells. By insertion of a calcium interfacial layer, an increase in the V_{OC} (1.66±0.01 V) was ascertained accompanied with an s-shaped J-V curve. This s-shaped curve is based on non-ohmic contact properties of the intermediate layer resulting in a decline of the FF and PCE, and yielded a significant increase in the series resistance.[29–36] By substituting calcium with cesium carbonate as interfacial layer, a poor efficiency based on a significant decline in V_{OC} (1.09±0.06 V) but a similar FF (about 45%) were obtained. However, multi-junction solar cells with Ag/MoO_3, Ca/Ag/MoO_3 and Cs_2CO_3/Ag/MoO_3 intermediate layers showed improved V_{OC}s but lower PCE-values compared to single-junction solar cells.

2.1.2.2.4 Other Intermediate Layers in Multi-Junction Solar Cells

Further intermediate layer combinations such as Cu/MoO_3, Ti/Cu/MoO_3 and Ti/MoO_3 were investigated in PCDTBT:[70]PCBM (1:2 w/w)-based tandem solar cells. The characteristic parameters are graphically represented in Figure 28.

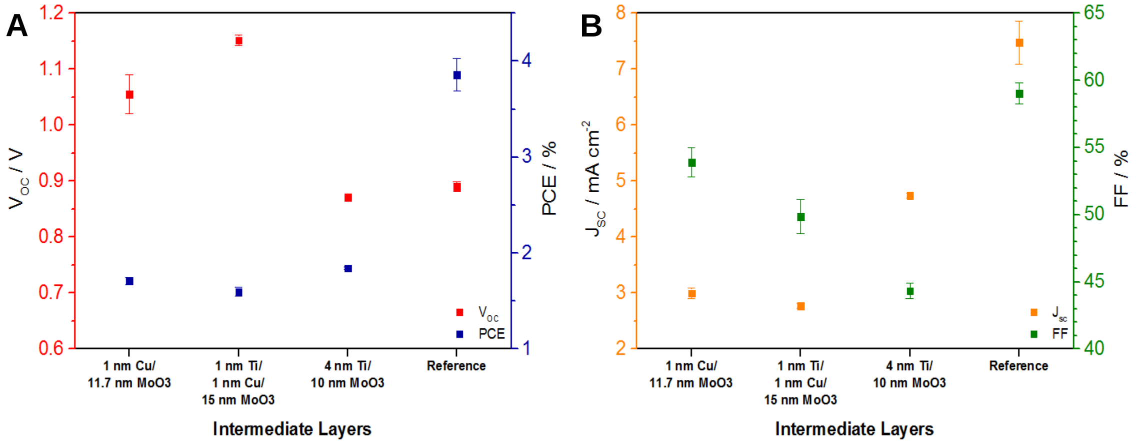

Figure 28: (A) Open circuit voltage and power conversion efficiency, and (B) short-circuit current density and fill factor of single- and multi-junction solar cells with Cu/MoO_3, Ti/Cu/MoO_3 and Ti/MoO_3 intermediate layers. Characteristic parameters were averaged over five solar cells.

Tandem solar cells with a Cu/MoO_3 intermediate layer exhibited a slightly improved V_{OC} but a lower FF, J_{SC} and PCE compared to the single-junction reference cell. By inserting a titanium interfacial layer, a further increase in V_{OC} was obtained accompanied with a decline in the J_{SC} and PCE. The additional interfacial layer also yielded a higher series resistance and a reduced FF. However, multi-junction solar cells with a Ti/MoO_3 intermediate layer apparently showed a poor device performance with a V_{OC} comparable to the single-junction reference cell. This is based on the effect of the low shunt resistance (0.57 ± 0.09 kΩ cm^2). Low shunt resistances provide an alternative, parallel path for photo-generated current without producing power.[81] This leakage currents reduce the solar cell characteristic parameters V_{OC}, J_{SC} and FF, and cause significant power losses.[81]

2.1.2.3 Triple-Junction Solar Cells

According to Kirchhoff's law, the open circuit voltage for multi-junction solar cells equals the sum of the V_{OC}s of each contributing sub-cell, which is valid for ideal, fully-transparent intermediate layers with loss-free charge recombination.[4,34] In order to investigate the effect of the number of stacked solar cells on the photo-voltage generation, single-, bi- and triple-junction solar cells were prepared consisting of PCDTBT:[70]PCBM (1:2 w/w) active layers connected in series via 1 nm Al / 15 nm MoO_3 intermediate layers. J-V curves and the photovoltaic performance parameters are shown in Figure 29 and Table 3, respectively.

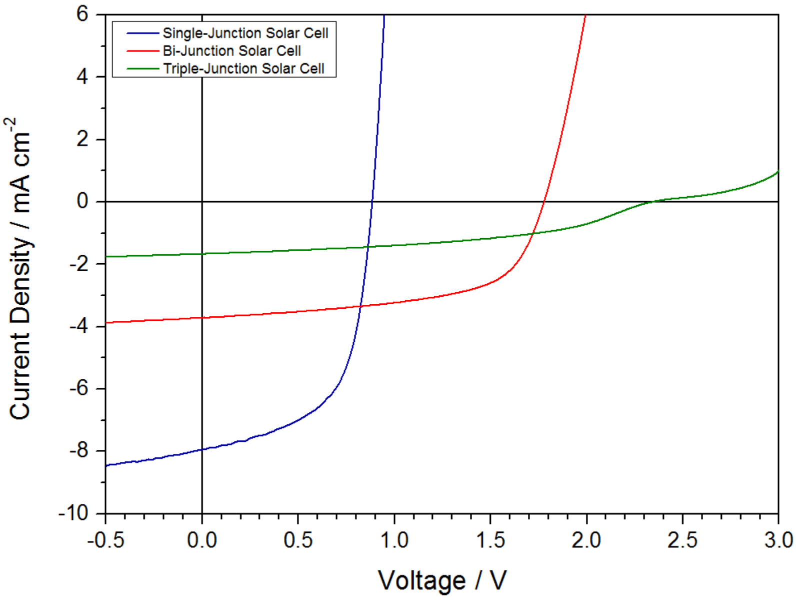

Figure 29: J-V curves of single-, bi- and triple-junction solar cells with PCDTBT:[70]PCBM active layers and 1 nm Al / 15 nm MoO_3 intermediate layers

Table 3: Average photovoltaic performance parameters of single-, bi- and triple-junction solar cells. Averages were taken over five solar cells. R_s- and R_{sh}-values were extracted from the respective J-V curves under illumination.

Device Geometry (Total Layer Thickness)	V_{OC} [V]	J_{SC} [mA cm²]	FF [%]	PCE [%]	R_s [Ω cm^2]	R_{sh} [kΩ cm^2]
Single-Junction (79±2 nm)	0.89±0.01	7.48±0.38	59.1±0.8	3.86±0.17	15.1±1.4	0.73±0.24
Bi-Junction (215±9 nm)	1.78	3.71±0.04	58.9±0.9	3.88±0.03	50.9±5.2	4.29±0.92
Triple-Junction (402±12 nm)	2.38±0.03	1.57±0.06	46.4±0.7	1.74±0.03	1000.3± 115.9	5.12±2.02

Comparing the device performance of single-, bi- and triple-junction solar cells, the V_{OC} increased with increasing number of stacked sub-cells, which can be explained by Kirchhoff's law. For bi-junction solar cells, the V_{OC} was found to be the sum of the V_{OC}s of both sub-cells. For triple-junction solar cells, about 89% of the maximal open circuit voltage was achieved. The decline in J_{SC} with increasing number of stacked sub-cells can be explained by the photo-current generation. According to Kirchhoff's law, the short-circuit current density of a multi-junction solar cell is limited by the minimum J_{SC} of each contributing sub-cell.[34] Hence, a smaller fraction of absorbed light can be proposed for the back cell and thus limiting the overall J_{SC} and PCE of the multi-junction solar cells. However, increasing the number of stacked sub-cells leaded to higher layer thicknesses corresponding to an improved light absorption behavior (Figure 30). Moreover, the R_s-value increased and the FF declined with higher number of stacked sub-cells. Single- and bi-junction solar cells exhibited comparable efficiencies, whereas the PCE-value significantly decreased for the triple-junction device. This is due to the tremendous increase in the series resistance and the lower FF, which can be assigned to the s-shaped curves obtained from the I-V measurements of the triple-junction solar cells. Since a V_{OC} and V_{mpp} exceeding 1.15 V was achieved with the tandem approach, bi-junction solar cells were used as photovoltaic system for the integrated solar battery hybrid device.

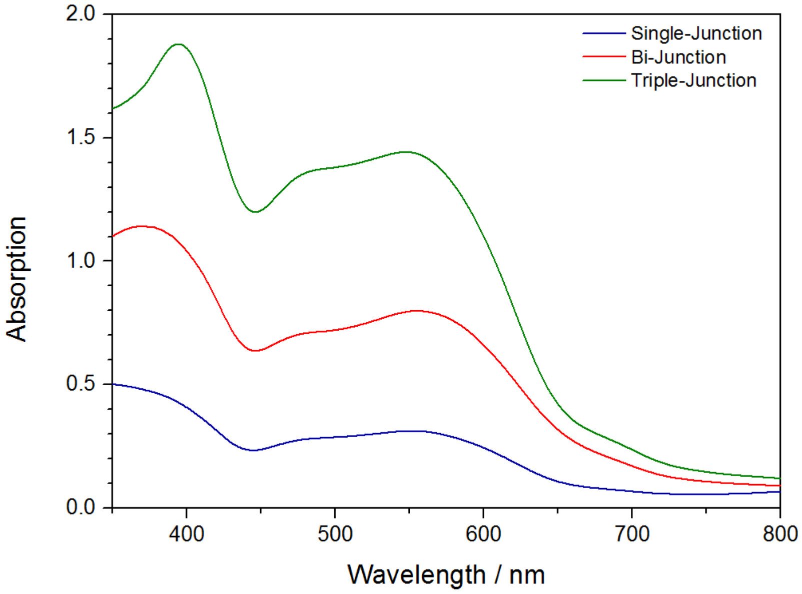

Figure 30: Absorption spectra of PCDTBT:[70]PCBM (1:2 w/w) single-, bi- and triple-junction solar cells in the range of 385-800 nm

2.1.3 Multi-Junction Solar Cells for Solar Battery Hybrid Devices

In order to determine the impact of the electrode geometry and active electrode area on the device performance of multi-junction solar cells, Ti/Cu electrodes with square (0.09 cm²) and circular (0.79 cm²) geometry were used as electrical contact for PCDTBT:[70]PCBM (1:2 w/w) tandem solar cells (Figure 31).

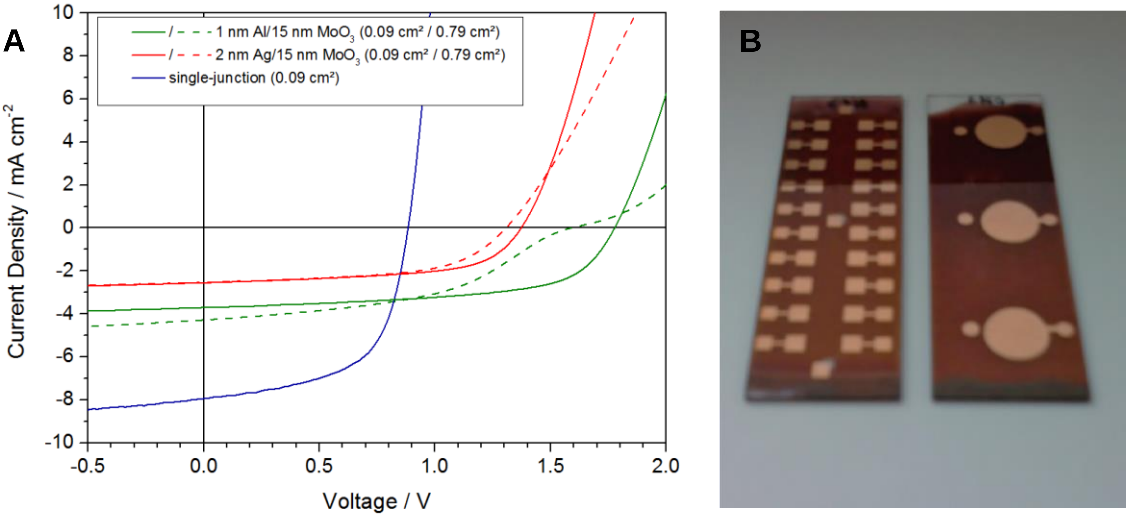

Figure 31: (A) J-V curves of multi-junction solar cells for the solar battery hybrid device with an active area of 0.79 cm² compared to multi-junction solar cells with 0.09 cm² electrode area and a single-junction solar cell. (B) PCDTBT:[70]PCBM multi-junction solar cells with square and circular electrode geometry.

For tandem solar cells with Ag/MoO_3 intermediate layers, the geometry of the electrode and the active electrode area exhibited only a minor effect on the device performance. Using square electrodes, for example, a slight decline in V_{OC}, FF and thus in PCE were obtained, whereas the J_{SC} was unaffected. Compared with tandem solar cells with Al/MoO_3 intermediate layers, a significant influence of electrode geometry and active area on the device performance was observed. Using square electrodes an s-shaped J-V curve was obtained yielding a drop in V_{OC}, FF and PCE but a slight increase in the J_{SC}. Even though solar cells with square electrode geometry showed better photovoltaic characteristics, solar cells with circular electrode geometry were required for the fabrication of integrated solar battery hybrid devices. The average series resistance R_s and shunt resistance R_{sh} of standard tandem solar cells for the hybrid device with a 1 nm Al and 15 nm MoO_3 intermediate layer was determined to be 240±70 Ω cm² and 1.83±0.68 kΩ cm², respectively.

2.1.4 Characterization

2.1.4.1 Optical Band Gap Determination

In order to determine the optical band gap (E_g) of various conjugated polymers (PCDTBT, PSiF-DBT, PCPDTBT, F8T2), polymer thin films were prepared by doctor blading of the respective polymer solution (10 mg/mL, in chlorobenzene) onto pre-cleaned and oxygen plasma etched microscope slides. The optical band gaps were ascertained from the onset of the absorption spectra of the polymer thin films. Figure 32 shows absorption spectra of polymer thin films for determination of the optical band gaps. The experimental optical band gaps of PCDTBT (1.85 eV), PSiF-DBT (1.82 eV), PCPDTBT (1.45 eV) and F8T2 (2.38 eV) matched with the E_g-values reported in the literature.[69,95–97]

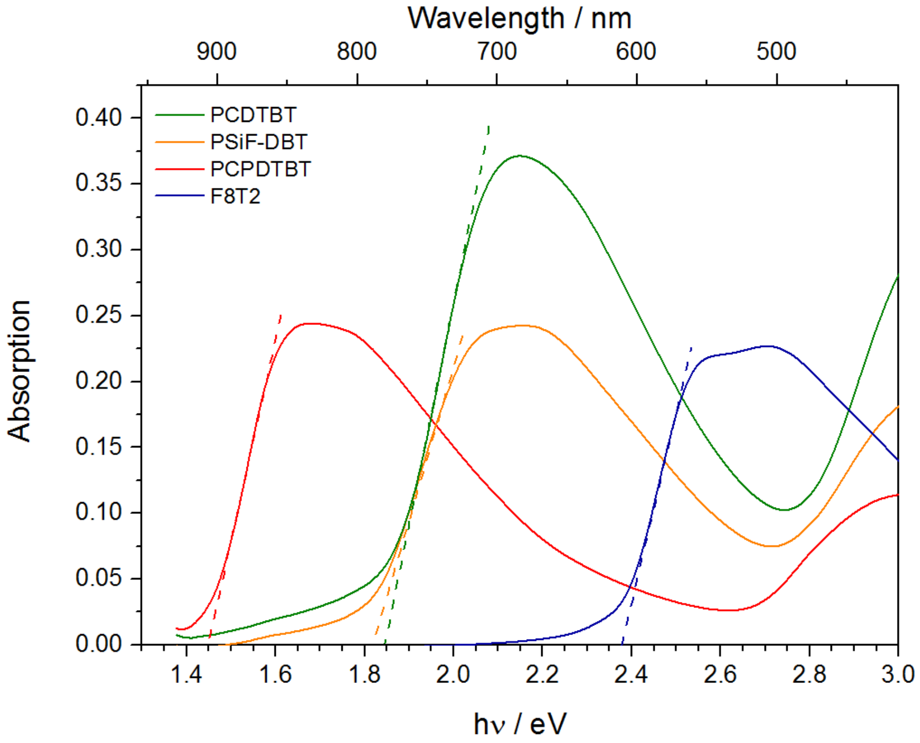

Figure 32: Optical band gaps of PCDTBT, PSiF-DBT, PCPDTBT and F8T2 polymer thin films determined from the onset of the absorption spectra

2.1.4.2 External Quantum Efficiency (EQE)

For the determination of the external quantum efficiency, single-junction solar cells with a MoO_3 hole-transport layer, a PCDTBT:[70]PCBM (1:2 w/w) active layer, and a Ti/Cu top electrode were prepared as described in Chapter 3.2. The external quantum efficiency was measured under nitrogen atmosphere in the range of 350-800 nm using an IPCE (incident photon-to-current efficiency) measuring unit. The recorded EQE-spectra of two single-junction solar cells with different layer thicknesses, and the absorption spectra of a PCDTBT thin film and a PCDTBT:[70]PCBM (1:2 w/w) single-junction solar cell are shown in Figure 33.

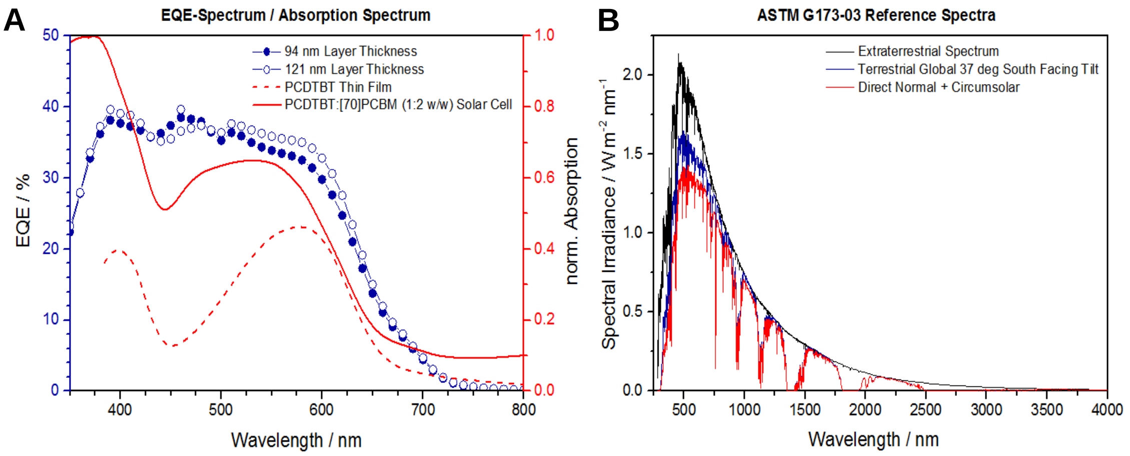

Figure 33: (A) External quantum efficiency in the visible region of two single-junction solar cells with PCDTBT:[70]PCBM active layers having a total layer thickness of 94 nm and 121 nm, and absorption spectra of a PCDTBT thin film and a PCDTBT:[70]PCBM (1:2 w/w) single-junction solar cell. (B) Reference AM 1.5 Spectra (ASTM G173-03 solar AM 1.5 emission spectrum)[98,99]

Considering the recorded EQE-spectra, PCDTBT:[70]PCBM solar cells showed a broad wavelength range for high photo-current generation with EQE-values over 35% between 380-520 nm and 380-580 nm depending on active layer thickness. Furthermore, EQE peak maxima at 390 nm, 460-480 nm, and 510 nm with EQE-values exceeding 36% were determined. In this way, the most important part of the solar emission spectrum (AM 1.5, Figure 33), namely the peak maximum in the solar emission spectrum, is covered.

With regard to the determined EQE-values, approx. 1/3 of the incident photons succeed in the formation of a separated pair of charge carriers that are collected at the electrodes. The prepared single-junction solar cells exhibited similar EQE-spectra but lower EQE-values in comparison to the ones reported in the literature for PCDTBT:[70]PCBM-based BHJ solar cells with a PEDOT:PSS hole-transport layer and Al electrodes (40-50% in the range of 350-600 nm).[7] A further improvement of EQE-values (about 60% in the range of 380-590 nm) was reported by spin-casting of the active layer from DCB, by adjusting the donor:acceptor ratio (1:4 w/w) and by modifying the top electrode (TiO_x/Al or LiF/Al).[65,100]

2.2 Lithium-Ion Battery Electrode Materials

Lithium-ion battery electrode materials, namely lithium titanate ($Li_4Ti_5O_{12}$), cobalt diantimonide ($CoSb_2$) and cobalt triantimonide ($CoSb_3$), were prepared and investigated with regard to an application in integrated solar battery hybrid devices. These materials were chosen for the assembling of low-voltage lithium-ion batteries providing a battery voltage up to 1.15 V vs. Li/Li^+. This was necessary since the battery voltage needed to be matched to the relatively low voltage supplied by the photovoltaic system, which was up to about 1.40 V (V_{mpp}), in order to charge the battery upon illumination of the solar cell. The electrode materials were characterized in half- and full-cell configuration using three-electrode Swagelok cells via common electrochemical methods such as cyclic voltammetry (CV), galvanostatic cycling with potential limitation (GCPL), galvanostatic intermittent titration technique (GITT), and potentio electrochemical impedance spectroscopy (PEIS) in order to get information about the electrochemical behavior of the active materials such as the specific charge/discharge capacity, the Coulombic efficiency, the cycling stability, the Li^+ diffusion coefficient in the active materials and the dynamic resistance of the galvanic cell.

2.2.1 Lithium Titanate ($Li_4Ti_5O_{12}$, LTO)

Lithium titanate is a promising anode material for rechargeable lithium-ion batteries because of a high theoretical specific capacity (175 mAh/g), a good cycling behavior with highly reversible Li ion insertion/extraction, structural stability upon lithiation/de-lithiation processes, a good mobility of Li ions, and a stable voltage plateau at about 1.55 V vs. Li/Li^+.[48–53] This discharge/charge plateau is attributed to the redox reaction of Ti^{4+}/Ti^{3+} in the lithium titanate host lattice and the corresponding two-phase transition between spinel LTO ($Li_4Ti_5O_{12}$) and rock-salt LTO ($Li_7Ti_5O_{12}$) upon reversible Li ion insertion/extraction processes (Scheme 1).[50,101] This implies that Li ions are inserted into the spinel-structured LTO under formation of rock-salt LTO during discharge, and that Li ions are extracted out of the rock-salt LTO, forming spinel LTO during charging.[48,101] Upon discharging, up to three Li ions are inserted per formula unit without considerable volume change (zero-strain insertion).[51] The insertion reaction corresponds to the reduction of three Ti^{4+} ions to Ti^{3+} and the extraction process to the oxidation of three Ti^{3+} ions to Ti^{4+}.

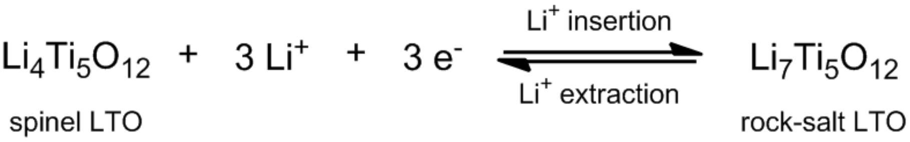

Scheme 1: Two-phase transition reaction of lithium titanate upon reversible Li ion insertion/ extraction processes[50]

Because of these advantageous characteristics, lithium titanate was selected as electrode material for solar battery hybrid devices. For this purpose, lithium titanate composite electrodes were prepared by ball milling and doctor blading of the LTO-based slurry composite on a copper foil as described in Chapter 3.3.1. The electrode material was electrochemically characterized in half-cell configuration via cyclic voltammetry in order to get information about the practical capacity and the chemical diffusion coefficient of Li^+ in the lithium titanate host lattice. In addition to that, galvanostatic cycling measurements were made to determine the discharge/charge capacity, the Coulombic efficiency and the cycling stability of the electrode material.

2.2.1.1 Cyclic Voltammetry

For electrochemical characterization of lithium titanate, the electrode material was assembled as working electrode in a three-electrode Swagelok cell in half-cell configuration with lithium metal as both counter and reference electrode. Figure 34 shows the cyclic voltammogram of lithium titanate, which was recorded in the range of 1.0-2.0 V vs. Li/Li^+ using different scan rates.

The CV measurement started with a reduction reaction resulting in a cathodic potential peak $E_{p,c}$ at 1.49 V vs. Li/Li$^+$, followed by an oxidation with an anodic potential peak $E_{p,a}$ at 1.64 V vs. Li/Li$^+$. During these steps, Li ions are inserted into and extracted out of the electrode material accompanied by the reversible two-phase transition between spinel- and rock-salt-structured LTO. In the subsequent reductive and oxidative half-cycles the cathodic and anodic potential peaks were located in the range of 1.47-1.51 V and 1.63-1.77 V vs. Li/Li$^+$, respectively.

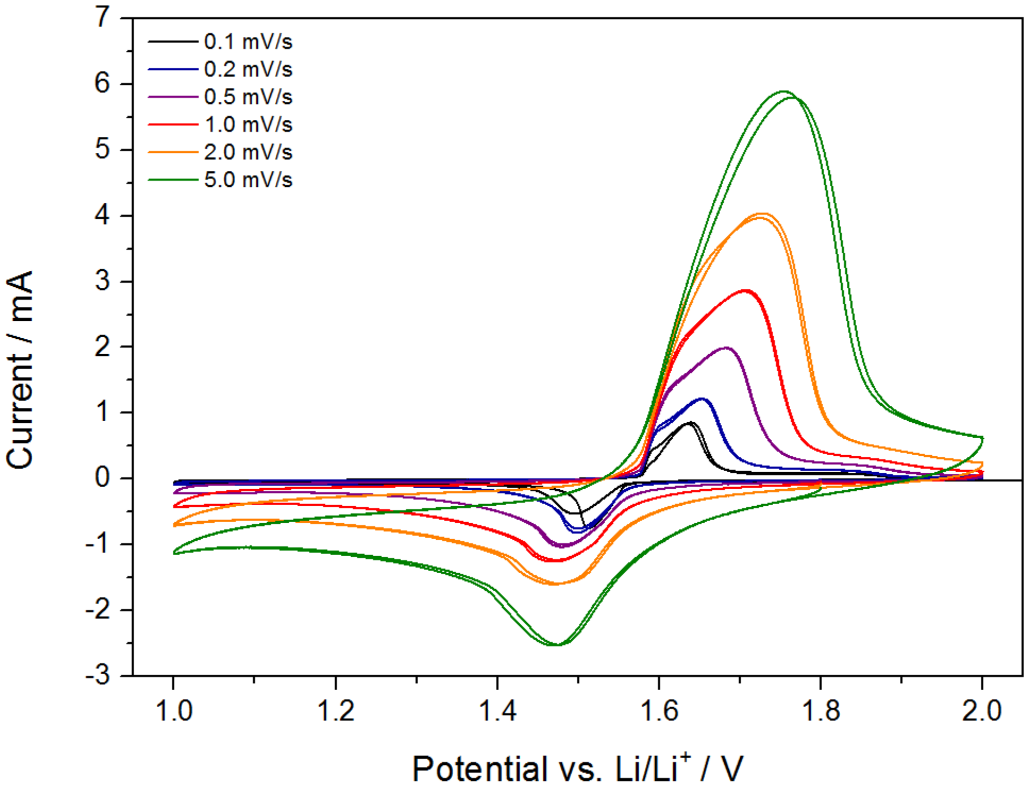

Figure 34: Cyclic voltammogram of lithium titanate in the potential range of 1.0-2.0 V vs. Li/Li$^+$ at various scan rates. Cathodic/anodic peaks are associated with Li ion insertion/extraction processes.

The formal potential $E^{0'}$, which is the arithmetic mean of cathodic ($E_{p,c}$) and anodic peak potentials ($E_{p,a}$)[102]

$$E^{0'} = \frac{E_{p,c} + E_{p,a}}{2}$$

(Eq. 1)

was determined to be 1.59±0.02 V vs. Li/Li$^+$. The corresponding cathodic/anodic peaks can be attributed to the reversible redox reaction of the Ti^{4+}/Ti^{3+} redox couple in the lithium titanate lattice, which is reported to take place at 1.55 V vs. Li/Li$^+$.[48]

The peak separation ΔE_p for a reversible system, which is defined as the difference in anodic and cathodic peak potentials,

$$\Delta E_p = E_{p,a} - E_{p,c}$$

(Eq. 2)

is independent from the scan rate and should present a ΔE_p-value of about 59 mV for a fully reversible one-electron reaction.[102] With regard to the examined LTO electrode material, the peaks in the cyclic voltammogram got broader and the anodic potential peaks were shifted to higher values by increasing the scan rate, whereas the cathodic ones remained constant. This means that the peak separation ΔE_p increased at higher scan rates and thus indicates electrochemical quasi-reversible or irreversible behavior of the redox system. This might be based on slow electron transfer processes at the electrode surface[102] or, more likely in this case, is due to a slow diffusivity (mass transport) of Li ions from the surface to the bulk of the LTO material.

In addition to that, the peak current ratio, which is calculated from the modulus of the ratio of the cathodic ($i_{p,c}$) and anodic ($i_{p,a}$) peak currents, decreased with increasing scan rate and was determined to be below 1.0 for all scan rates.

$$Peak\ Current\ Ratio = \left| \frac{i_{p,c}}{i_{p,a}} \right|$$

(Eq. 3)

The peak current function, which is defined as the ratio of the peak current i_p to the square root of the scan rate, $v^{1/2}$,

$$Peak\ Current\ Function = \frac{i_p}{v^{1/2}}$$

(Eq. 4)

of the examined lithium titanate electrode material was found to show a slight dependence on varying scan rates. This gives information about an irreversible behavior of the electrode material, which can be due to aforementioned slow electron transfer processes at the electrode surface[102] or to relatively sluggish ion transport in the active material.

A graphical representation of the peak separation, the peak current ratio and the peak current function as function of the logarithm of the scan rate for the respective first and second cycles is shown in Figure 35.

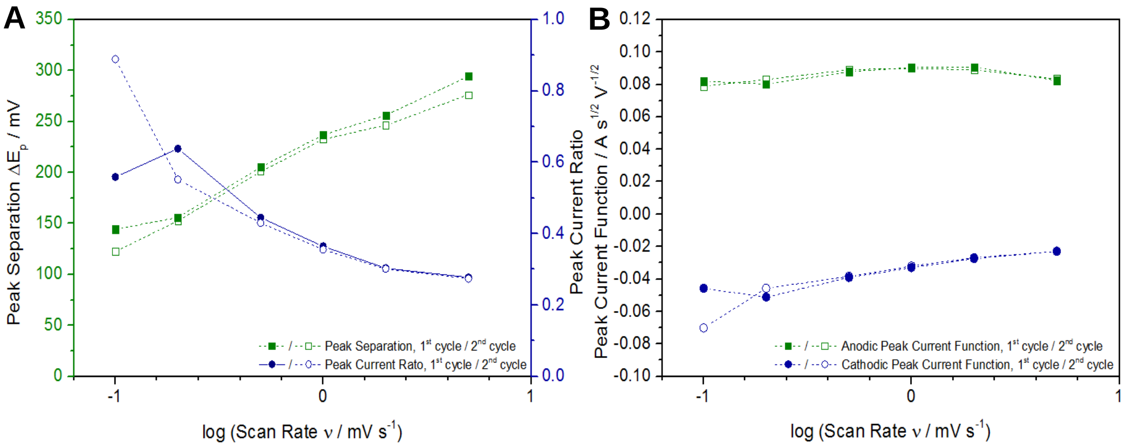

Figure 35: (A) Peak separation ΔE_p and peak current ratio, and (B) peak current function as function of the logarithm of the scan rate ν of lithium titanate

The practical capacity of lithium titanate was determined from the first anodic half-cycle of the cyclic voltammogram via peak integration. The specific practical capacity of lithium titanate was 112.5 mAh/g, which is significant lower compared to the theoretical capacity (175 mAh/g).[48] This can be ascribed to the non-optimized electrode preparation. In this case, not all of the LTO active material is in electronic contact, through the conductive carbon, with the copper current collector. It has to be noticed that lithium titanate has a significantly lower theoretical specific capacity compared to metallic lithium (3,860 mAh/g).[103] With regard to the theoretical gravimetric capacity, lithium titanate would be a less favorable electrode material compared to metallic lithium but lithium metal electrodes have to face problems with lithium dendrites growth and low Coulombic efficiencies.[103] Thus, metallic lithium in its pristine form is not an alternative for good performance battery.

In order to determine the chemical diffusion coefficient D of Li^+ in the lithium titanate electrode material via cyclic voltammetry, the Randles-Sevcik equation for an irreversible electrochemical reaction at planar electrodes was used.[104,105]

$$i_p = 0.4958 \times nFACD^{1/2} \times \left(\frac{\alpha n_a F}{RT}\right)^{1/2} \times \nu^{1/2}$$

(Eq. 5)

where i_p is the peak current in A, n and n_a are the numbers of electrons, F is the Faraday constant in As mol^{-1}, A is the surface area of the electrode in cm², C is the concentration of maximum obtainable Ti^{3+} centers in the lattice, i.e., 22.9×10^{-3} mol cm^{-3}, D is the chemical diffusion coefficient of the electro-active species in cm² s^{-1}, α is the transfer coefficient taken as 0.5, R is the ideal gas constant in J mol^{-1} K^{-1}, T is the absolute temperature in K, ν is the scan rate in V s^{-1}.

The surface area of the electrode was estimated from the mean particle size of LTO EXM 1037 (Süd-Chemie) electro-active material. The average particle size determined via light scattering was found to be 2.4±0.1 µm, which matched quite well with the d_{50}-value of ca. 2.3 µm reported for the particle size distribution in the specification sheet of LTO EXM 1037.[106] Assuming spherical particles, the developed electrode surface area corresponding to the LTO active material was calculated to be about 13 cm² for an electrode disk 9.5 mm in diameter. The specific surface area was estimated to be 0.74 m²/g, which is only about a fourth of the typical specific surface area of the active material determined by Brunauer-Emmet-Teller (BET) analysis.[106]

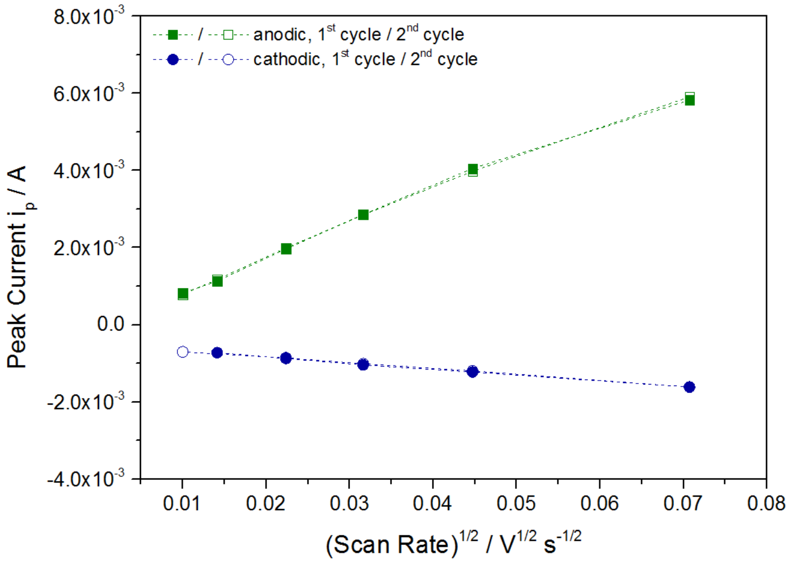

Figure 36: Determination of the chemical diffusion coefficient of Li^+ in lithium titanate via Randles-Sevcik method: Cathodic and anodic peak currents are plotted versus the square root of ν

Figure 36 shows the anodic and cathodic peak current i_p as function of the square root of the scan rate, $\nu^{1/2}$. The peak currents show linear dependence on $\nu^{1/2}$. Based on this graphical representation, the chemical diffusion coefficient D was calculated from the slope of the regression line. The chemical diffusion coefficient of Li^+ in the lithium titanate host lattice was determined to be 1.8×10^{-12} cm²/s / 6.0×10^{-14} cm²/s (using anodic/cathodic peak currents). The results match quite well with the values reported in the literature, where chemical diffusion coefficients in the range of 10^{-8}-10^{-15} cm²/s were determined, depending on the particle size, the preparation procedure and the electrochemical method.[51,107–109] Consequently, Li ion extraction processes in the prepared LTO electrodes take place at a higher rate compared to the insertion processes and therefore are kinetically preferred.

2.2.1.2 Galvanostatic Cycling with Potential Limitation

Based on the data of the previous CV experiment, the potential limits for the GCPL experiment of lithium titanate were set to 1.0 and 1.8 V vs. Li/Li^+. The galvanostatic cycling measurement was performed at two different C-rates, namely C/2 and C/5, each one for 50 cycles.

Figure 37 shows the discharge and charge cycling performance as well as the Coulombic efficiency of lithium titanate. The initial discharge/charge capacity was determined to be 157 / 74 mAh/g. The discharge capacity significantly dropped to 87 mAh/g in the 2nd cycle, whereas the charge capacity slightly increased to 78 mAh/g. Afterwards both values stabilized at about 80 mAh/g at a C-rate of C/2 and at 100 mAh/g at C/5. In addition to that, lithium titanate showed a low initial Coulombic efficiency of only 47%. The Coulombic efficiency value increased to 97% in the 10th cycle, first exceeded 98% in the 16th cycle and stabilized at about 99% in the following cycles. Lithium titanate showed a quite good electrochemical behavior and cycling stability.

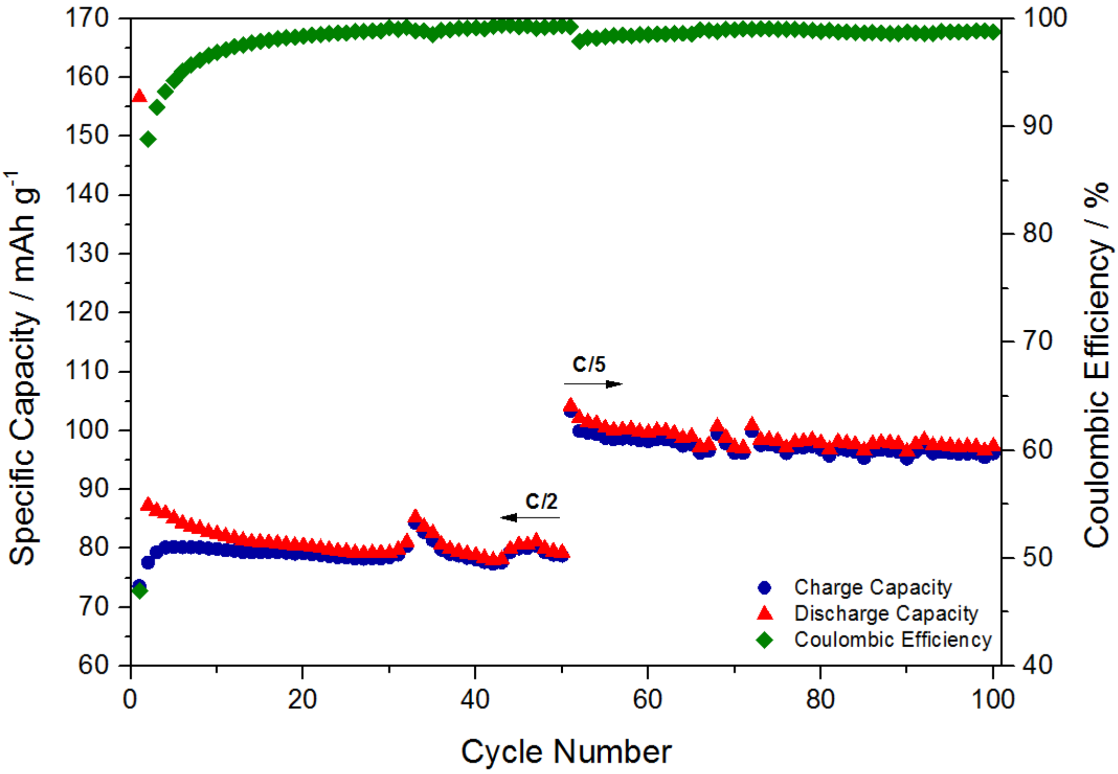

Figure 37: Discharge and charge cycling performance as well as the Coulombic efficiency of lithium titanate cycled at C-rates of C/2 and C/5 in the potential range of 1.0-1.8 V vs. Li/Li$^+$

Figure 38 shows voltage profile curves of lithium titanate and the state of Li ion insertion/extraction for various cycles, which where galvanostatically cycled at C/2 in the potential range of 1.0-1.8 V vs. Li/Li$^+$. The discharge/charge voltage profiles of lithium titanate showed a flat voltage plateau at about 1.50-1.55 V vs. Li/Li$^+$ with very low polarization (below 50 mV). This plateau can be assigned to reversible Li ion insertion/extraction processes in the lithium titanate host lattice, which is accompanied by the two-phase transition between spinel- and rock-salt-structured LTO.[50,101] The discharge capacity (lithiation reaction) decreased drastically from an initial capacity of 157 mAh/g to 85 mAh/g in the 5th cycle, followed by a stabilization at about 80 mAh/g up to the 50th cycle. In comparison to that, the charge capacity (de-lithiation reaction) in the initial cycle (74 mAh/g) slightly increased to approximately 80 mAh/g in the following cycles.

With regard to the composition of the lithium titanate material, $Li_{4+x}Ti_5O_{12}$ (x = 2.68) was initially formed upon Li$^+$ insertion during galvanostatic cycling. In the subsequent

Li^+ extraction process, most of the inserted alkali metal ions were removed giving an averaged composition of $Li_{4+x}Ti_5O_{12}$ (x = 1.26). The lithium titanate composition stabilized at x = 1.3-1.4 in the followed cycles.

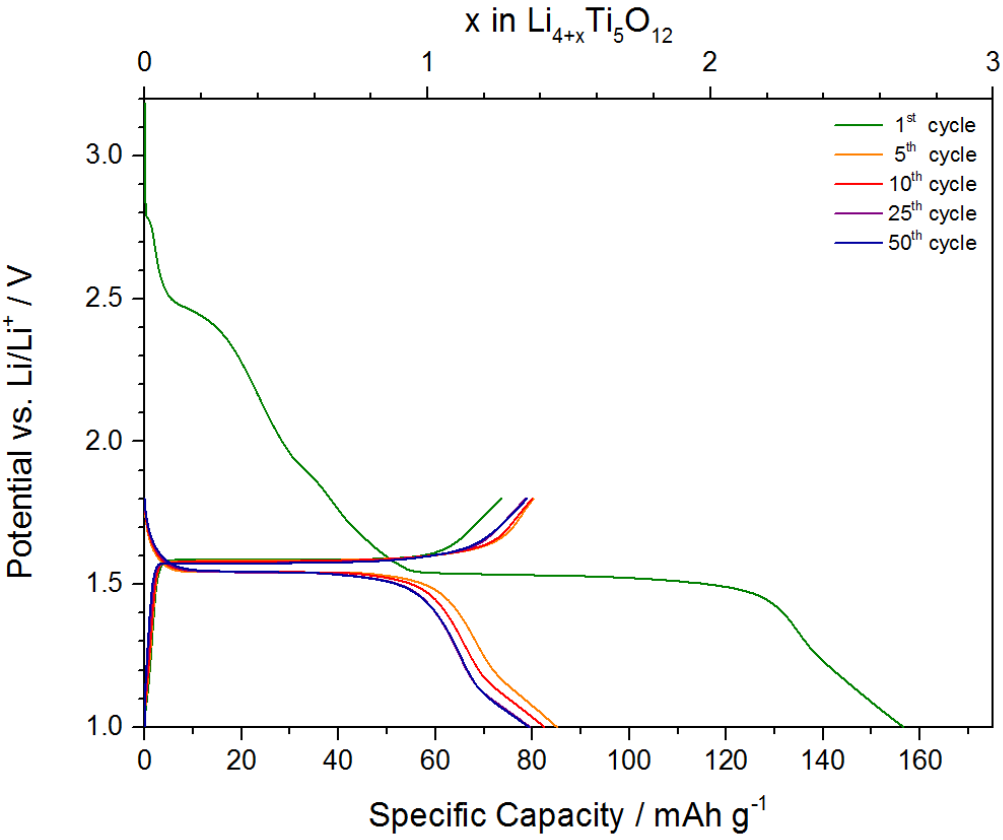

Figure 38: Galvanostatic discharge/charge voltage curves and state of Li ion insertion/extraction of lithium titanate cycled at C/2 for the 1st, 5th, 10th, 25th, and 50th cycle

2.2.2 Cobalt Diantimonide ($CoSb_2$) and Cobalt Triantimonide ($CoSb_3$)

Co-Sb intermetallic compounds such as $CoSb_2$ and $CoSb_3$ are potential alternative anode materials for rechargeable lithium-ion batteries because of a good electrochemical performance, improved theoretical capacities ($CoSb_2$: 530 mAh/g[110], $CoSb_3$: 569 mAh/g[111]) compared to graphite (372 mAh/g)[55], flat voltage plateaus, a good cycling stability, and less volume change problems compared to pure antimony.[54,55] This reduced volume expansion is due to the presence of Li-inert cobalt.[54,55] Two possible reactions of Co-Sb intermetallic compounds ($CoSb_y$) with Li ions can be proposed (Scheme 2): Lithium reacts with Co-Sb intermetallics under formation of (i) a Li-based ternary Li_xCoSb_y phase by an insertion/addition reaction or (ii) a Li_3Sb phase well-dispersed in a cobalt matrix through a conversion reaction.[54,57]

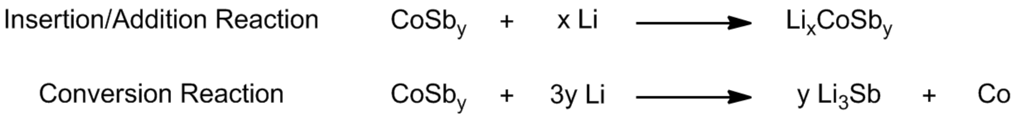

Scheme 2: Insertion/addition reaction and conversion reaction of Co-Sb intermetallic compounds with lithium[54]

Because of these advantageous characteristics, cobalt diantimonide and cobalt triantimonide were selected as electrode materials for solar battery hybrid devices. For this purpose, $CoSb_2$ and $CoSb_3$ electrodes were prepared via mechanical alloying by ball milling of stoichiometric amounts of the respective metal powders and doctor blading of the Co-Sb-based slurry on a copper foil as described in Chapter 3.3.2. Subsequently, the Co-Sb intermetallic compounds were electrochemically characterized in half-cell configuration via cyclic voltammetry in order to get information about the practical capacity and the diffusion coefficient of Li^+ in the $CoSb_2$ and $CoSb_3$ lattice. In addition to that, galvanostatic cycling measurements were made to determine the discharge/charge capacity, the cycling stability and electrochemical behavior of the electrode materials.

2.2.2.1 Cyclic Voltammetry

For electrochemical characterization of cobalt di- and triantimonide via cyclic voltammetry, the electrode materials were assembled as working electrode in three-electrode Swagelok cells in half-cell configuration with lithium metal as both counter and reference electrode. Figure 39 shows the cyclic voltammogram of $CoSb_2$ and $CoSb_3$, which was recorded in the region of 0.1-2.0 V vs. Li/Li^+ using different scan rates.

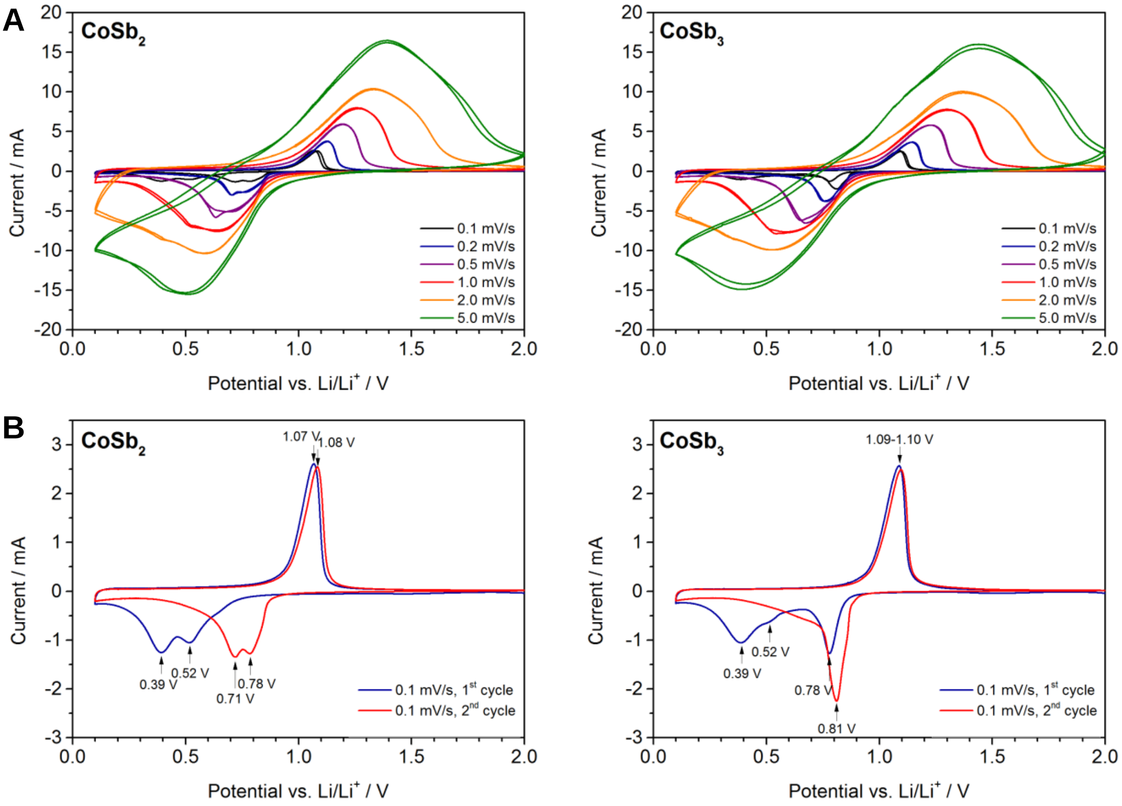

Figure 39: (A) Cyclic voltammogram of $CoSb_2$ and $CoSb_3$ in the potential range of 0.1-2.0 V vs. Li/Li^+ at various scan rates. (B) 1st and 2nd cycle of the cyclic voltammogram of $CoSb_2$ and $CoSb_3$ at a scan rate of 0.1 mV/s.

Basically, cathodic peaks occurring in the reductive half-cycle and anodic peaks in the oxidative half-cycle correspond to Li ion insertion/extraction processes with respect to the electrode material. For $CoSb_2$, the initial cathodic and anodic potentials peaked at 0.39 V / 0.52 V and 1.07 V vs. Li/Li^+, respectively. In the second cycle, the cathodic peaks were shifted to 0.71 V and 0.78 V, whereas the anodic one remained constant. For subsequent reduction-oxidation half-cycles, the $E_{p,c}$ and $E_{p,a}$ values were located in the range of 0.50-0.72 V and 1.08-1.39 V vs. Li/Li^+. The initial reductive and oxidative potentials of $CoSb_3$ were located at 0.39 V / 0.78 V with a shoulder at 0.52 V, and 1.09 V vs. Li/Li^+. In the second cycle, the cathodic peaks were shifted to 0.81 V, whereas the anodic one remained constant. For the subsequent reduction-oxidation processes, the peak potentials were found in the range of 0.40-0.81 V and 1.09-1.44 V vs. Li/Li^+. Shifts of the cathodic potential peaks from the first to the second cycle give information about irreversible processes occurring during the first reduction reaction. During the first reductive half-cycle, an irreversible decomposition of the $CoSb_y$ (y = 2,3) solid takes place concomitant with the reaction with lithium under formation of a Li_3Sb phase well-dispersed in a cobalt matrix via a conversion reaction.[54,57] The peak in the first oxidative half-cycle can be attributed to the de-alloying of the Li_3Sb phase forming antimony dispersed in a cobalt matrix without reconstructing $CoSb_y$.[54,112] Because of this irreversible decomposition, the cathodic peaks shifted to 0.71-0.81 V vs. Li/Li^+ in the second cycle. The oxidation peaks, in contrast, remained unaffected. The reduction/oxidation peaks in the subsequent cycles can be assigned to reversible antimony alloying/de-alloying processes.

The formal potential $E^{0'}$ of the examined Co-Sb intermetallics was determined to be 0.94±0.02 V vs. Li/Li^+ (for $CoSb_2$) and 0.94±0.01 V vs. Li/Li^+ (for $CoSb_3$). The corresponding cathodic peaks are attributed to the formation of the binary Li_3Sb phase (0.948 V) and cobalt, whereas the oxidation peaks are assigned to the de-alloying of the Li_3Sb phase forming amorphous antimony dispersed in a cobalt matrix without reconstruction of $CoSb_y$.[44,54,57,112]

By increasing the scan rate, the cathodic and anodic potential peaks in the cyclic voltammogram of both $CoSb_2$ and $CoSb_3$ got broader and were shifted tendentially to lower and higher values. Consequently, the peak separation ΔE_p showed non-linear dependence on the scan rate (Figure 40), which might be based on slow electron transfer processes at the electrode surface[102] or, more likely in this case, is due to a slow diffusivity (mass transport) of Li^+ from the surface to the bulk of the cobalt antimonide material. This indicates a quasi-reversible or irreversible behavior of the redox system, which is supported by a peak separation exceeding 59 mV for a one-electron reaction.

Comparing the cathodic and anodic current peaks in the cyclic voltammogram, $CoSb_2$ exhibited slightly higher currents and hence improved electrochemical activities compared to $CoSb_3$. In addition to that, the peak current ratio increased at higher scan rates for both $CoSb_2$ and $CoSb_3$ (Figure 40). A current ratio exceeding 1.0 was found for scan rates higher than 1 mV/s for $CoSb_2$ compared to 0.2 mV/s for $CoSb_3$. The peak current function exhibited only a minor dependence on the scan rate in particular at higher scan rates.

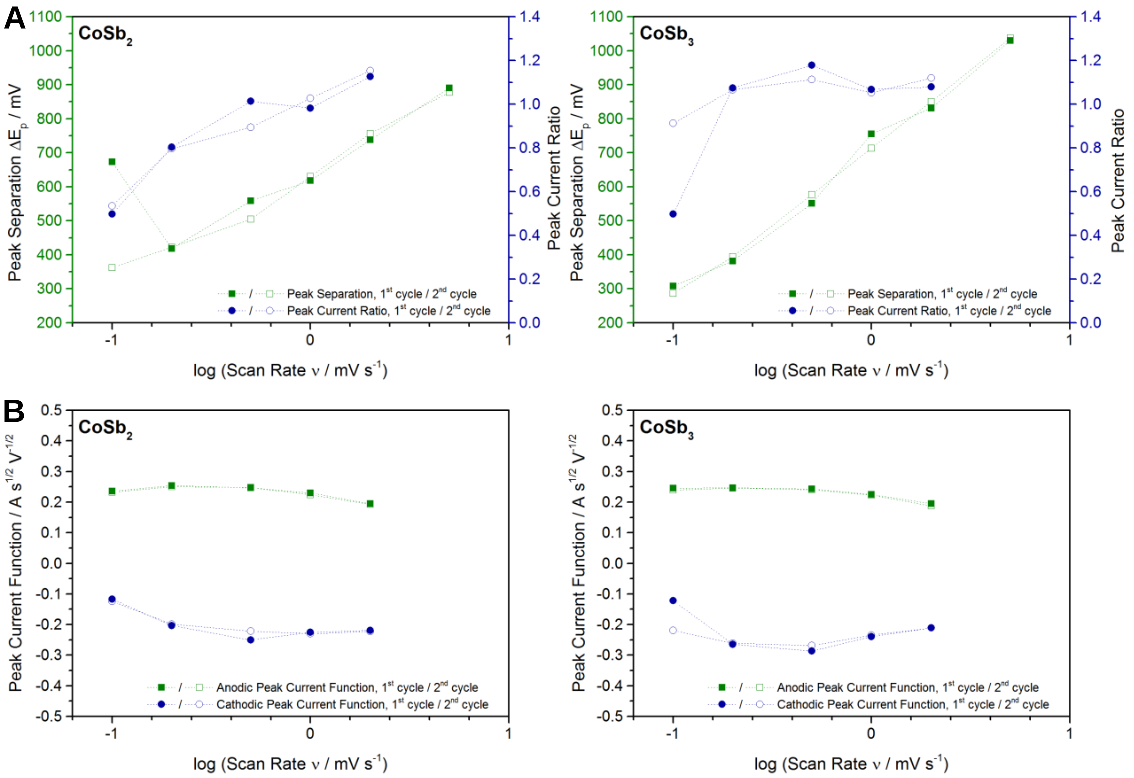

Figure 40: (A) Peak separation ΔE_p and peak current ratio, and (B) peak current function as function of the logarithm of the scan rate ν of $CoSb_2$ and $CoSb_3$

The specific practical capacities of $CoSb_2$ and $CoSb_3$ were calculated from the second and first anodic half-cycle of the cyclic voltammogram by peak integration. Hence, the specific capacities of $CoSb_2$ and $CoSb_3$ were determined to be 350 mAh/g and 373 mAh/g, respectively. Both values are far below the theoretical capacities of $CoSb_2$ (530 mAh/g)[110] and $CoSb_3$ (569 mAh/g)[111] reported in the literature. The Co-Sb intermetallics exhibited a significant lower theoretical capacity compared to pure antimony (660 mAh/g, based on the formation of Li_3Sb), which is due to the presence of Li-inert cobalt.[55,113] Nevertheless, cobalt antimonides show preferable electrochemical characteristics since pure antimony electrodes face structural stability problems based on large volume expansion resulting from repetitive discharge/charge reactions.[54]

The chemical diffusion coefficients D of Li^+ in the $CoSb_2$ and $CoSb_3$ electrode materials were determined via cyclic voltammetry using the Randles-Sevcik equation for an irreversible electrochemical reaction at planar electrodes[104], as described in Eq. 5. The concentration of maximum obtainable Sb centers in the lattice was 55.2×10^{-3} mol/cm^3 for $CoSb_2$ and 54.0×10^{-3} mol/cm^3 for $CoSb_3$. The surface areas of the electrodes were estimated from the mean particle sizes of the ball milled cobalt antimonides. The average particle sizes of $CoSb_2$ (2.6±0.4 µm) and $CoSb_3$ (4.1±1.2 µm) were determined via light scattering. Assuming spherical particles, the electrode surface areas were calculated to be 5.6 cm^2 ($CoSb_2$) and 3.7 cm^2 ($CoSb_3$) for an electrode disk 9.5 mm in diameter. The corresponding specific surface area values of 0.26 m^2/g ($CoSb_2$) and 0.19 m^2/g ($CoSb_3$) are in good agreement with the BET surface for $CoSb_3$ (0.26 m^2/g) reported in the literature.[114] The peak currents were found to show a linear dependence on $v^{1/2}$ for both $CoSb_2$ and $CoSb_3$ (Figure 41). Based on this graphical representation, the chemical diffusion coefficients D of Li^+ in the Co-Sb intermetallic lattices were calculated from the slope of the regression line.

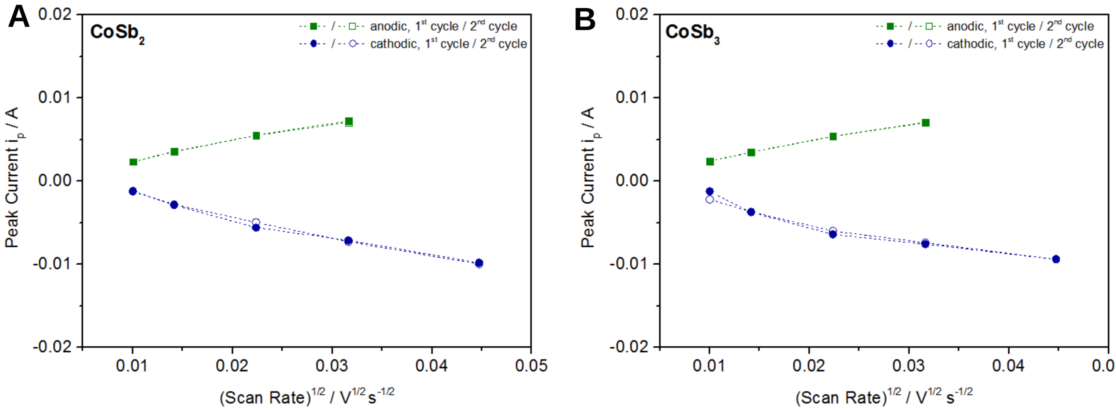

Figure 41: Determination of the chemical diffusion coefficients of Li^+ in cobalt antimonides via Randles-Sevcik method: Cathodic and anodic peak currents are plotted versus $v^{1/2}$ for (A) $CoSb_2$ and (B) $CoSb_3$

Table 4 shows that the Li^+ diffusion coefficients in both $CoSb_2$ and $CoSb_3$ are in a similar range of $1.1\text{-}2.5\times10^{-11}$ cm^2/s but are higher for the alkali metal ion diffusion in the cobalt triantimonide. However, both cobalt antimonides have significant higher chemical diffusion coefficients of one to three orders of magnitudes compared to lithium titanate.

Table 4: Chemical diffusion coefficient D of Li^+ in cobalt antimonides determined via cyclic voltammetry

	Chemical Diffusion Coefficient of Li^+ [cm²/s]	
	using anodic peak currents	using cathodic peak currents
$CoSb_2$	1.1×10^{-11}	1.4×10^{-11}
$CoSb_3$	2.5×10^{-11}	2.4×10^{-11}

2.2.2.2 Galvanostatic Cycling with Potential Limitation

Galvanostatic cycling measurements of $CoSb_2$ and $CoSb_3$ were performed at two different C-rates, namely C/2 and C/5, each one for 50 cycles in the potential range of 0.75 V to 1.1 V vs. Li/Li^+. Because of relative low discharge and charge capacities, an initial galvanostatic cycling sequence was introduced, which consisted of four cycles cycled at C/2 within the potential limits of 0.2-1.1 V vs. Li/Li^+. The low potential limit in the first cycles was used to allow the formation of the electrode, as noticed in the cyclic voltammetry experiment. Consequently, higher discharge and charge capacities were obtained, which is due to the initial formation step occurring at lower potentials. The discharge and charge cycling performance as well as the Coulombic efficiency of $CoSb_2$ and $CoSb_3$ without and with the initial formation step are shown in Figure 42 and Figure 43, respectively. Electrochemical characteristics of $CoSb_2$ and $CoSb_3$ are summarized in Table 5.

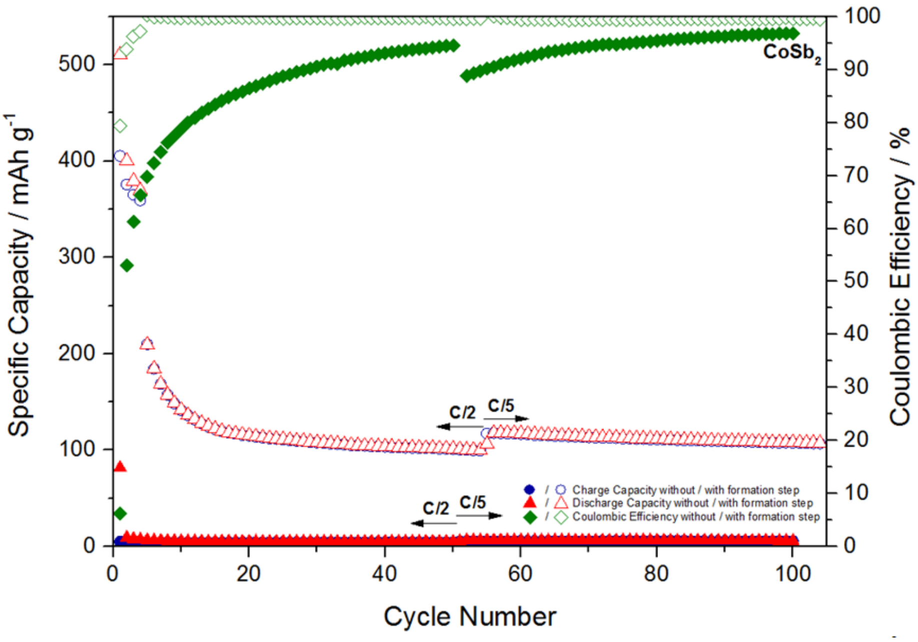

Figure 42: Discharge and charge cycling performance as well as the Coulombic efficiency of $CoSb_2$ cycled at C-rates of C/2 and C/5 (a) without and (b) with the initial formation step

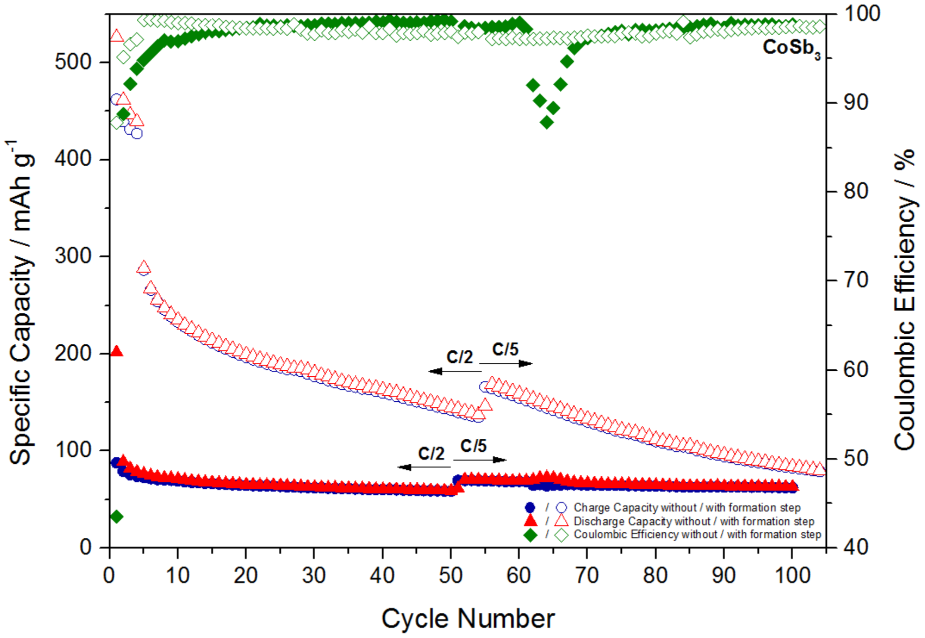

Figure 43: Discharge and charge cycling performance as well as the Coulombic efficiency of $CoSb_3$ cycled at C-rates of C/2 and C/5 (a) without and (b) with the initial formation step

Table 5: Electrochemical characteristics of $CoSb_2$ and $CoSb_3$ determined by galvanostatic cycling (a) without and (b) with the initial formation sequence

Electrode	**Formation Sequence**	**1st discharge capacity [mAh g^{-1}]**	**1st charge capacity [mAh g^{-1}]**	**Initial Coulombic efficiency [%]**
$CoSb_2$	without formation step	82	5	6
$CoSb_2$ (initial / after formation step)	with formation step	511 / 210	405 / 210	79 / 100
$CoSb_3$	without formation step	202	88	44
$CoSb_3$ (initial / after formation step)	with formation step	526 / 288	462 / 286	88 / 99

Li insertions/extractions correspond to discharging/charging reactions. During the first discharge cycle, an irreversible decomposition of the $CoSb_y$ (y = 2,3) solid takes place concomitant with the reaction with lithium under formation of a binary Li_3Sb phase well-dispersed in a cobalt matrix via a conversion reaction.[54,57] In the first charging cycle, Li ions are extracted from the Sb-alloy forming amorphous antimony dispersed in cobalt without reconstructing $CoSb_{y.}$[54,112] In case of nanostructured metals within this composite, Tarascon et al. reported the conversion back to $CoSb_3$ based on a chemical reaction between antimony and cobalt nanograins during the Sb-dealloying process.[115] However, upon galvanostatic cycling, reversible Li insertion/extraction steps can be proposed concomitant with Li-Sb reactions at about 0.8 V vs. Li/Li^+ involving Sb-alloy formation/decomposition processes (Scheme 3).[54,57]

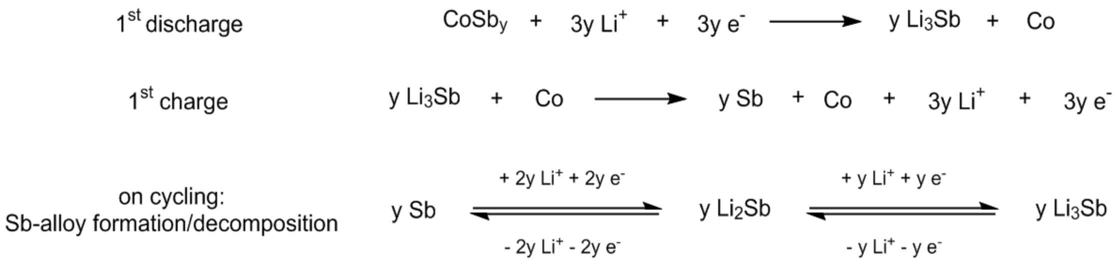

Scheme 3: Reaction mechanism of Li insertion/extraction during the first discharge/charge cycle and on galvanostatic cycling of Co-Sb intermetallic compounds ($CoSb_y$, with y = 2,3)[54,115]

Comparing the cycling performances, lowering the potential limits for an initial sequence in galvanostatic cycling measurements of $CoSb_2$ and $CoSb_3$ yielded a drastic increase in both the discharge and charge capacity. $CoSb_2$ exhibited a very poor electrochemical behavior during first investigations with an initial discharge/charge capacity of 82 / 5 mAh/g. By lowering the initial potentials in the galvanostatic cycling experiment, the electrochemical performance drastically improved. The initial discharge/charge capacity of $CoSb_2$ in the first cycle was determined to be 511 / 405 mAh/g. A similar trend was also observable for cobalt triantimonide. The discharge/charge capacity of $CoSb_3$ in the first cycle increased from 202 / 88 mAh/g to 526 / 462 mAh/g. However, the initial discharge capacities of both examined cobalt antimonides are lower compared to the theoretical capacities of $CoSb_2$ (530 mAh/g[110]) and $CoSb_3$ (569 mAh/g[111]).

Both materials showed an improved discharge/charge capacity after the initial formation sequence with 210 / 210 mAh/g ($CoSb_2$) and 288 / 286 mAh/g ($CoSb_3$). Although $CoSb_3$ exhibited better discharge/charge capacities compared to $CoSb_2$ in the first cycle after the formation sequence, $CoSb_2$ showed a better electrochemical behavior and cycling stability during prolonged galvanostatic cycling. The discharge/charge capacities of $CoSb_2$ stabilized after about 15 cycles and remained constant afterwards, whereas the discharge/charge capacities of $CoSb_3$ dropped during prolonged cycling showing a significant capacity fading with increasing number of cycles. Especially for longer galvanostatic cycling experiments, $CoSb_2$ showed a higher discharge/charge capacity compared to $CoSb_3$. The poor cycling stability and electrochemical behavior of $CoSb_3$, in particular the rapid decline in discharge/charge capacities, might be due to tremendous volume changes resulting from repeated Li ion insertion/extraction during discharge/charge reactions.[55] According to Park et al., the same problem is basically known for Sb-based systems.[54] This volume expansion can be reduced by adding Li-inert cobalt to the Li-active antimony with the obvious drawback of having even lower capacities than $CoSb_3$ with respect to pure antimony (660 mAh/g).[54,55] Indeed, an improved cycling stability and better electrochemical behavior was recorded for $CoSb_2$ because of higher amounts of the Li-inert cobalt and thus less problems with regard to the aforementioned volume expansion of the electrodes. These irreversible capacities of $CoSb_3$ are associated with the lower potentials set for the initial formation sequence. This is supported by the improved cycling behavior of $CoSb_3$ galvanostatically cycled without the formation step but significant lower discharge/charge capacities were obtained.

In addition to that, lowering the initial potential limits in galvanostatic cycling of Co-Sb intermetallic compounds greatly affected the initial Coulombic efficiency. As a result, the initial Coulombic efficiency in the 1st cycle increased from 6% to 79% (for $CoSb_2$) and from 44% to 88% (for $CoSb_3$). Hence, both electro-active materials showed a high initial Coulombic efficiency in the low-potential formation sequence. The Coulombic efficiencies in the first cycle after the formation step were quite high (100% for $CoSb_2$, and 99% for $CoSb_3$). During long-term galvanostatic cycling, $CoSb_2$ showed a higher Coulombic efficiency exceeding 99% and a high-reversible cycling behavior compared to $CoSb_3$ (97-99%).

As mentioned before, a positive impact on the cycling performance, discharge/charge capacities and initial Coulombic efficiencies of both $CoSb_2$ and $CoSb_3$ was determined by introducing an initial formation sequence with lower potential limitations. This formation sequence is essential for a good cell performance, in particular for high-capacity applications. It is based on the irreversible decomposition of the $CoSb_y$ solid concomitant with the formation of a binary Li_3Sb phase at a potential of about 0.5 V vs. Li/Li^+.[54,57] Since galvanostatic cycling without the formation sequence was performed in the potential range of 0.75 V to 1.1 V vs. Li/Li^+, the Li_3Sb phase was not formed or only in small amounts leading to significant lower capacities. Lowering the potential limits for galvanostatic cycling to 0.2-1.1 V vs. Li/Li^+ was necessary for the Li_3Sb phase formation upon discharging, yielding a significant increase in the capacity values. As a result of this formation sequence, a reversible alloying/de-alloying of antimony upon galvanostatic cycling with enhanced discharge/charge capacities can be proposed.

This is supported by the voltage profile curves of $CoSb_2$ and $CoSb_3$ shown in Figure 44. During the initial discharge sequence of the formation step, small voltage plateaus at 0.87 V and 0.73 V vs. Li/Li^+ were found for $CoSb_3$, which are based on the irreversible decomposition of the $CoSb_y$ solid and successive formation of Li_2Sb and Li_3Sb phases.[116] Moreover, $CoSb_2$ and $CoSb_3$ both exhibited an edge at about 0.4-0.5 V vs. Li/Li^+, which can be assigned to the conversion to the Li_3Sb alloy. The subsequent discharge voltage plateaus were located at about 0.87 V vs. Li/Li^+ and thus give information about the presence of aforementioned irreversible reactions taking place in the initial discharge process. However, the charge voltage curves remained unaffected and were located at about 1.0 V vs. Li/Li^+ corresponding to reversible de-alloying of the formed Li_3Sb phase.

Focusing on the voltage profile curves after the initial formation sequence (Figure 44, B), both examined Co-Sb intermetallic compounds exhibited a voltage plateau at about 0.94 V vs. Li/Li^+ with a low polarization in the range of 150-200 mV. This relative flat plateau, in particular in the first cycles, can be assigned to the formation of Li_3Sb (0.948 V vs. Li/Li^+) upon irreversible decomposition of the $CoSb_y$ solid.[44]

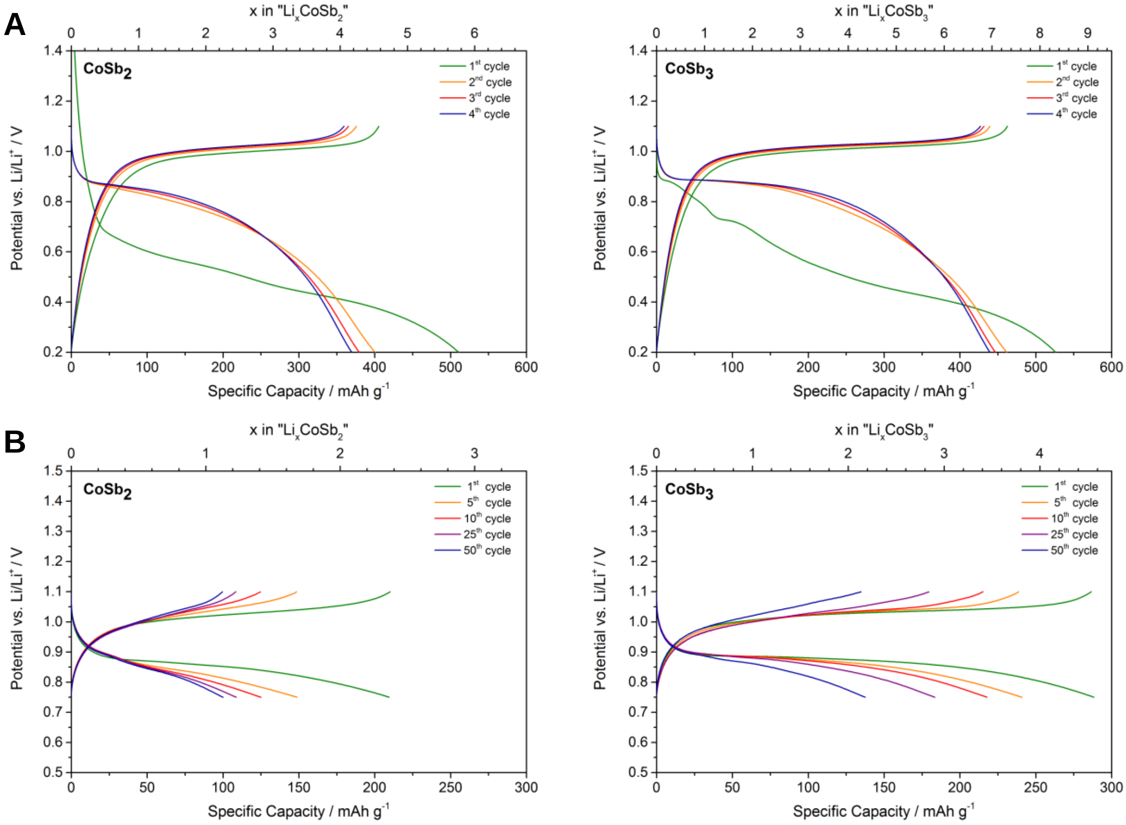

Figure 44: Galvanostatic discharge/charge voltage profile curves cycled at a C-rate of C/2 for (A) the initial formation sequence of $CoSb_2$ and $CoSb_3$ and of (B) the 1st, 5th, 10th, 25th, and 50th cycle after initial formation step of $CoSb_2$ and $CoSb_3$

Upon Li ion insertion in the initial discharge cycle, a reversible uptake of 2.4 Li (for $CoSb_2$) and 4.6 Li (for $CoSb_3$) per formula unit were obtained. The subsequent charging step showed highly reversible behavior since almost all inserted alkali metal ions were extracted again. The composition of both Co-Sb intermetallics at the 50th cycle after the initial formation sequence stabilized at about 1.15 Li (for $CoSb_2$) and 2.2 Li (for $CoSb_3$) per formula unit in discharged state, which is approximately half the value compared to the initial discharge cycle.

With regard to the application of the electrode materials in full-cell configuration, $CoSb_2$ showed better electrochemical behavior, cycling stability and Coulombic efficiencies during galvanostatic cycling but presented lower discharge/charge capacities than $CoSb_3$. The discharge/charge capacities of both $CoSb_2$ and $CoSb_3$ were higher compared to lithium titanate (LTO), which limits the capacity of the full-cell. Because of the advantageous electrochemical behavior of $CoSb_2$ compared to $CoSb_3$, the cobalt diantimonide was preferably used for the full-cell configuration tests.

2.2.3 Characterization of Electrode Materials in Full-Cell Configuration

After electrochemical characterization of the electro-active species (lithium titanate, cobalt di- and triantimonide) in half-cell configuration, the performance of the electrode materials was evaluated in full-cell configuration in three-electrode Swagelok cells. Lithium titanate and the Co-Sb intermetallic compounds both are negative electrode materials in conventional lithium-ion batteries operating at different electrochemical potentials. For the assembling of a battery in full-cell configuration, LTO was used as positive electrode (about 1.55 V vs. Li/Li^+[48]), $CoSb_y$ (y = 2,3) as negative electrode (about 0.95 V vs. Li/Li^+[44]) and metallic lithium as reference electrode. The theoretical potential difference between the positive and negative electrode is therefore about 0.6 V vs. Li/Li^+, which should match with the voltage at the maximum power point (V_{mpp}) supplied by the tandem solar cell. This is important for charging and discharging of the battery since this set-up should be used in the integrated power pack.

The electrochemical characterization of the electrode materials in full-cell configuration included a GITT experiment in order to pre-lithiate the Co-Sb intermetallic compounds for subsequent galvanostatic cycling measurements. This is a necessary step since none of the chosen materials contain lithium in their pristine form. GCPL tests were performed in order to evaluate the cycling stability and electrochemical behavior (discharge/charge capacity, Coulombic efficiency) of the battery. PEIS measurements were carried out in order to determine the dynamic resistance and impedance of the battery.

2.2.3.1 Galvanostatic Intermittent Titration Technique

For pre-lithiation of the Co-Sb intermetallic electrodes for subsequent GCPL tests, a GITT experiment was performed comprising a series of galvanostatic current pulses at a C-rate of C/20 interrupted by 30 min relaxation periods. During these negative current pulses, Li ions are inserted into the electrode material under formation of pre-lithiated $CoSb_y$ electrodes, which are referred to as "Li_xCoSb_2" and "Li_xCoSb_3" in the following chapters. Figure 45 shows the GITT curves for the lithiation process of $CoSb_2$ and $CoSb_3$.

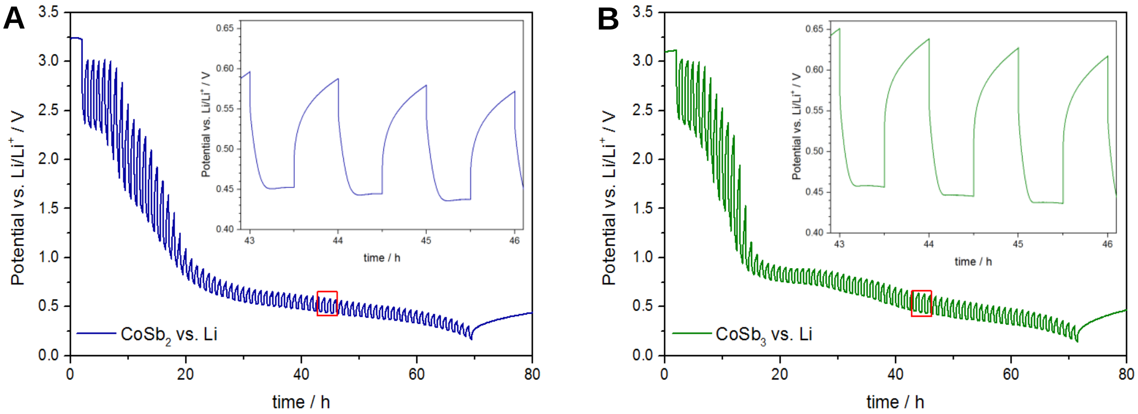

Figure 45: Galvanostatic intermittent titration technique curves for the pre-lithiation of (A) $CoSb_2$ and (B) $CoSb_3$ in three-electrode Swagelok cells. Insets show potential curves as function of time.

During the insertion of Li ions into the Co-Sb intermetallic compound electrodes, an irreversible decomposition of the $CoSb_y$ solid takes place concomitant with the reaction with lithium forming a well-dispersed mixture of a binary Li_3Sb phase dispersed in cobalt via a conversion reaction.[54,57] The plateaus in the GITT curves can be assigned to Li-Sb reactions upon successive formation of Li_2Sb and Li_3Sb phases during Li ion insertion.[54,116]

2.2.3.2 Galvanostatic Cycling with Potential Limitation

In order to determine the cycling performance of the examined electrode materials in full-cell configuration, three-electrode Swagelok cells from the GITT experiment were used comprising LTO as working electrode (WE), lithiated Co-Sb intermetallic compounds (“Li_xCoSb_2” and “Li_xCoSb_3”) as counter electrode (CE) and lithium metal as reference electrode (RE). The galvanostatic cycling experiments were performed at C-rates of C/2 and C/5 with respect to the LTO electrode each one for 26 cycles. The potential limits of LTO (1.3-1.8 V vs. Li/Li$^+$), “Li_xCoSb_2” (0.65-1.0 V vs. Li/Li$^+$) and “Li_xCoSb_3” (0.65-1.1 V vs. Li/Li$^+$) were chosen based on preliminary experiments. The respective galvanostatic cycling curves over time are shown in Figure 46.

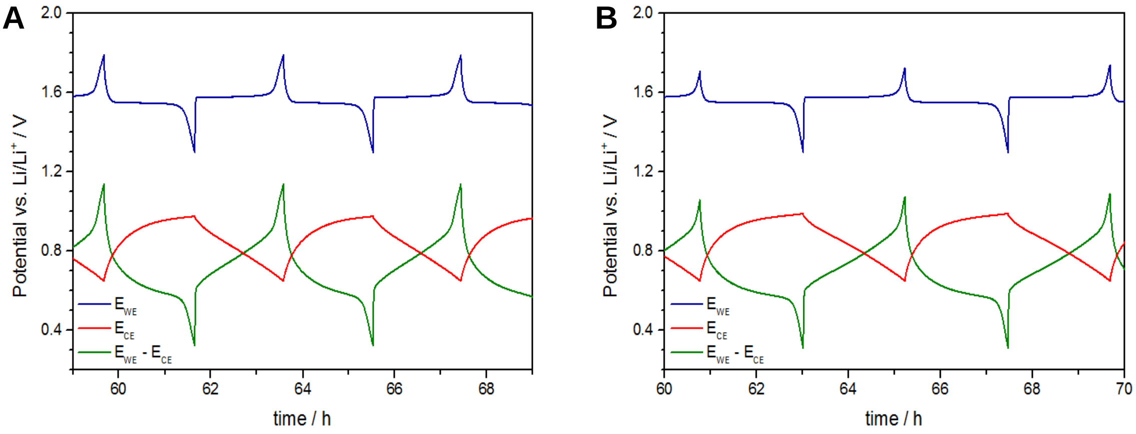

Figure 46: Galvanostatic cycling curves over time for (A) “Li$_x$CoSb$_2$”/LTO and (B) “Li$_x$CoSb$_3$”/LTO. E_{WE} refers to the potential at the LTO electrode vs. Li, E_{CE} to potential at the “Li$_x$CoSb$_y$” electrode vs. Li and E_{WE}-E_{CE} to the potential of the full-cell battery device.

Figure 47 shows the discharge and charge cycling performance as well as the Coulombic efficiency of “Li$_x$CoSb$_2$”/LTO and “Li$_x$CoSb$_3$”/LTO full-cells cycled at a C-rate of C/2 and C/5. The respective electrochemical characteristics are summarized in Table 6.

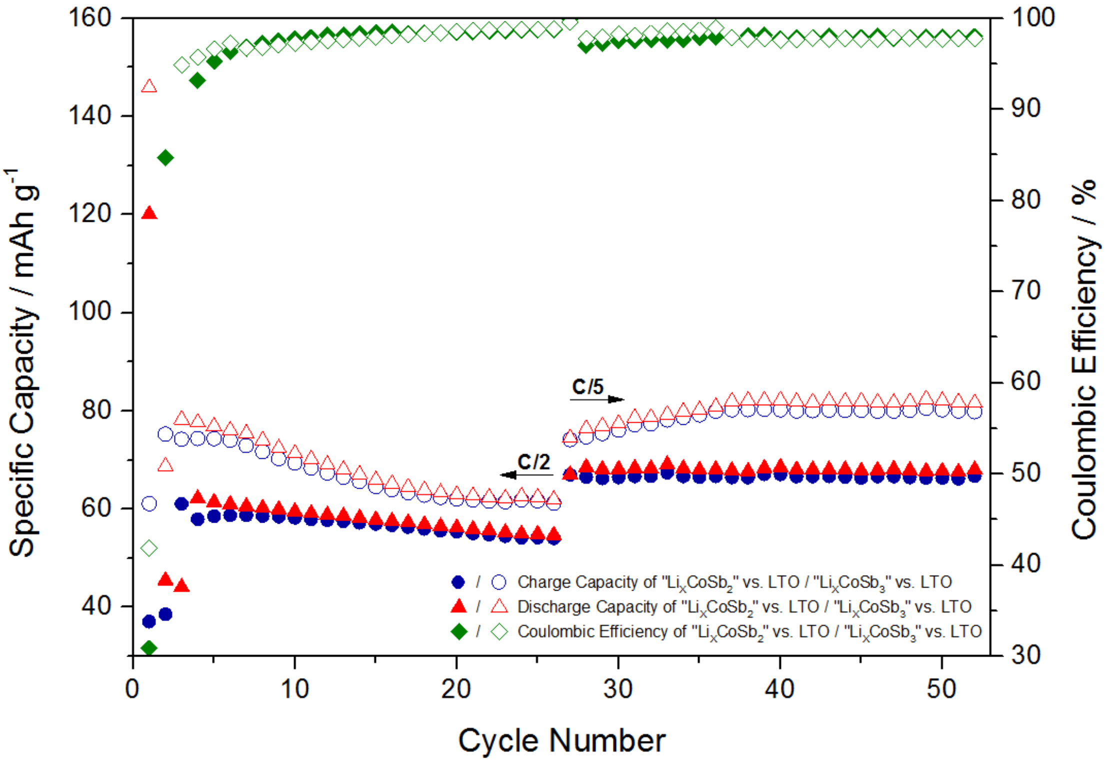

Figure 47: Discharge and charge cycling performance as well as the Coulombic efficiency of “Li$_x$CoSb$_2$”/LTO and “Li$_x$CoSb$_3$”/LTO full-cells cycled at C-rates of C/2 and C/5

Table 6: Electrochemical characteristics of “Li_xCoSb_2”/LTO and “Li_xCoSb_3”/LTO

Battery	1st discharge capacity [mAh g^{-1}]	1st charge capacity [mAh g^{-1}]	Initial Coulombic efficiency [%]
“Li_xCoSb_2” / LTO	120	37	31
“Li_xCoSb_3” / LTO	146	61	42

During discharge processes, Li ions are extracted out of the pre-lithiated Co-Sb intermetallic compounds, namely from the Li_3Sb phase, and inserted into the lithium titanate lattice, which is accompanied by the two-phase transition of the spinel LTO into the rock-salt LTO.[50] The “Li_xCoSb_y” electrode material is converted to disordered antimony and cobalt providing a well-dispersed solid mixture.[54] During charging, Li ions are extracted out of the rock-salt LTO concomitant with the successive Sb-alloy formation at about 0.8 V vs. Li/Li^+.[54,57] The rock-salt LTO material is converted back to the spinel-type LTO.

Comparing the initial capacities of both full-cell assemblies, “Li_xCoSb_3”/LTO showed better discharge/charge capacities (146 / 61 mAh/g) compared to “Li_xCoSb_2”/LTO (120 / 37 mAh/g). However, the “Li_xCoSb_3”/LTO full-cell exhibited a rapid decline of the specific capacity in the first cycles, followed by a significant capacity fading. The values stabilized at about 62 mAh/g (C/2) and 80 mAh/g (C/5). A similar trend was also observed for $CoSb_3$ in half-cell configuration (Chapter 2.2.2.2). In contrast, “Li_xCoSb_2”/LTO showed a better cycling stability and electrochemical behavior during prolonged galvanostatic cycling. After a decline in the discharge capacity in the first cycles, the values remained constant at approximately 55 mAh/g (C/2) and 67 mAh/g (C/5). The charge capacities, on the other hand, increased after the initial cycle, followed by a similar decline compared to the discharge capacity counterpart. Similar to the galvanostatic cycling experiment in half-cell configuration, the “Li_xCoSb_2”/LTO battery showed less capacity decay than the “Li_xCoSb_3”/LTO battery. As mentioned before, the poor cycling stability and electrochemical behavior, namely the rapid decline in discharge/charge capacity, might be caused by volume expansion effects in Sb-based systems resulting from repeated Li-insertion/extraction during galvanostatic cycling.[55]

However, both full-cell assemblies showed low initial Coulombic efficiencies (31% for “Li_xCoSb_2”/LTO, 42% “Li_xCoSb_3”/LTO) but stabilized over 97% after the 10th cycle. During long-term galvanostatic cycling, both batteries showed similar Coulombic efficiencies exceeding 97%.

Figure 48 shows the galvanostatic discharge/charge voltage profiles of “Li_xCoSb_2”/LTO and “Li_xCoSb_3”/LTO batteries cycled at a C-rate of C/2 for a various number of cycles. Both full-cell battery devices showed a flat voltage plateau at about 1.55 V vs. Li/Li^+ with very low polarization in the range of 50-70 mV (“Li_xCoSb_2”/LTO) and 40-60 mV (“Li_xCoSb_3”/LTO). This plateau can be assigned to the insertion/extraction processes of Li ions into the lithium titanate lattice.[50]

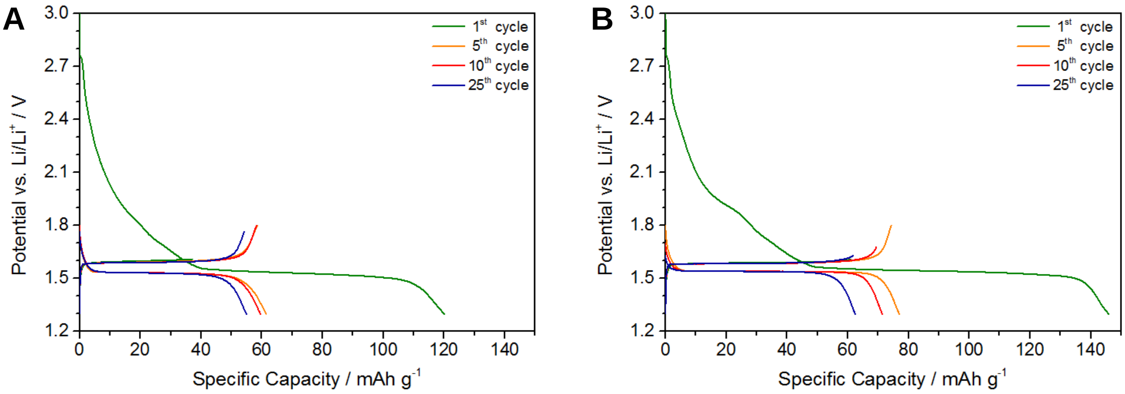

Figure 48: Galvanostatic discharge/charge voltage profile curves of (A) “Li_xCoSb_2”/LTO and (B) “Li_xCoSb_3”/LTO cycled at a C-rate of C/2 for the 1st, 5th, 10th, and 25th cycle

Based on the galvanostatic cycling experiment, “Li_xCoSb_2”/LTO showed better electrochemical behavior and cycling stability but lower initial discharge/charge capacities compared to the “Li_xCoSb_3”/LTO battery. This is why the “Li_xCoSb_2”/LTO set-up was preferably used for integrated solar battery hybrid devices.

2.2.3.3 Determination of the Dynamic Resistance and Impedance

The dynamic resistance and impedance of the full-cell configuration were determined using a series of linked DC (direct current) and AC (alternating current) measurement techniques comprising galvanostatic cycling and potentio electrochemical impedance spectroscopy (PEIS). The method included a series of negative and positive current pulses with a C-rate of C/2 with respect to the LTO electrode in the voltage range of 1.3-1.8 V vs. Li/Li$^+$ at the working electrode. Impedance measurements were performed in the range of 200 kHz-10 mHz with a sinus amplitude of 2 mV after each sequence of discharge and charge. The dynamic resistance was determined from DC measurements.

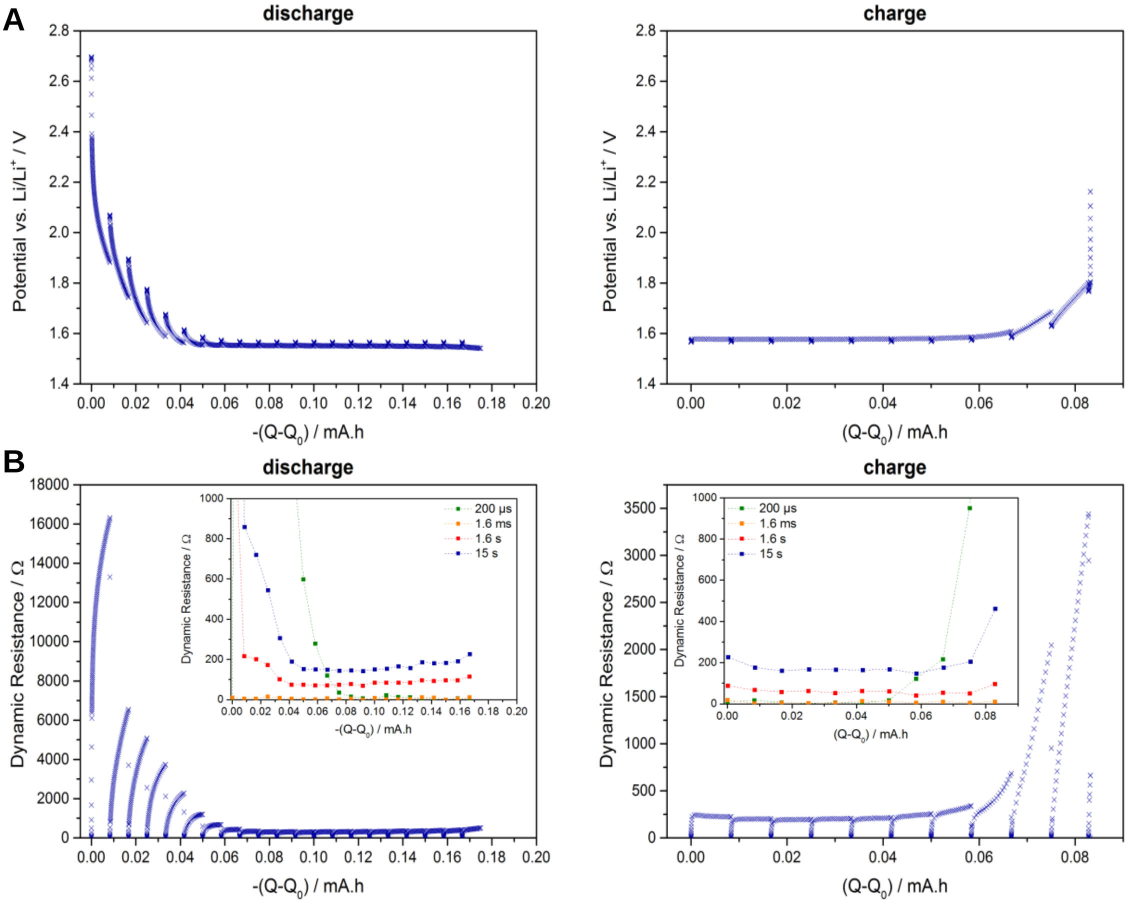

Figure 49: “Li$_x$CoSb$_2$”/LTO: (A) Voltage evolution versus charge during discharge and charge. (B) Dynamic resistance change during the whole discharge and charge. Insets show the dynamic resistance change at a certain period after the pulse: 200 µs, 1.6 ms, 1.6 s, and 15 s for the discharge and charge step

Figure 49 shows the voltage evolution as function of charge for discharging and charging of “Li$_x$CoSb$_2$”/LTO. For discharging processes, the potential at the working electrode stabilized at about 1.55 V vs. Li/Li$^+$ after an initial deep voltage drop, whereas the potential increased during charging after a constant plateau. The dynamic resistance decreased during the whole discharge and increased during the whole charge. The dynamic resistance at a certain period after the pulse rapidly decreased during the discharge step and started to stabilize afterwards. With increasing time after the current pulse, higher dynamic resistances were obtained. Upon charging, the dynamic resistance was found to be quite stable initially but increased drastically afterwards.

For "Li_xCoSb_3"/LTO, a similar trend in voltage evolution as function of charge was found compared to "Li_xCoSb_2"/LTO (Figure 50). After an initial deep voltage drop, a constant voltage plateau at the working electrode at 1.55 V vs. Li/Li^+ upon discharging was reached, whereas after a constant plateau a significant increase in voltage was obtained upon charging. Moreover, the dynamic resistance decreased during the whole discharge and increased during the whole charge. With increasing time after the current pulse, higher dynamic resistances were obtained. Again, the dynamic resistance behavior is quite similar compared to the "Li_xCoSb_2"/LTO counterpart.

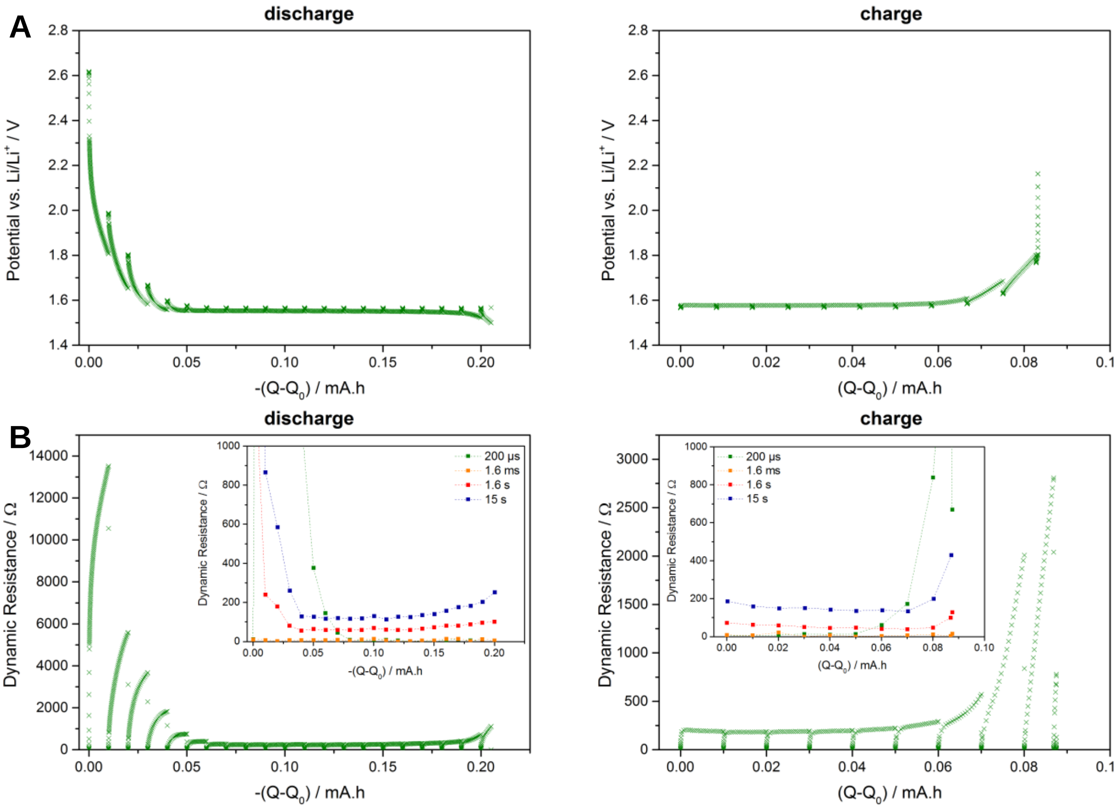

Figure 50: "Li_xCoSb_3"/LTO: (A) Voltage evolution versus charge during discharge and charge. (B) Dynamic resistance change during the whole discharge and charge. Insets show the dynamic resistance change at a certain period after the pulse: 200 µs, 1.6 ms, 1.6 s, and 15 s for the discharge and charge step.

Figure 51 shows the evolution of voltage over time during discharge and charge of “Li$_x$CoSb$_2$“/LTO and “Li$_x$CoSb$_3$“/LTO lithium-ion batteries. After an initial voltage drop to ca. 1.55 V vs. Li/Li$^+$ during discharge, the voltage increased during charge.

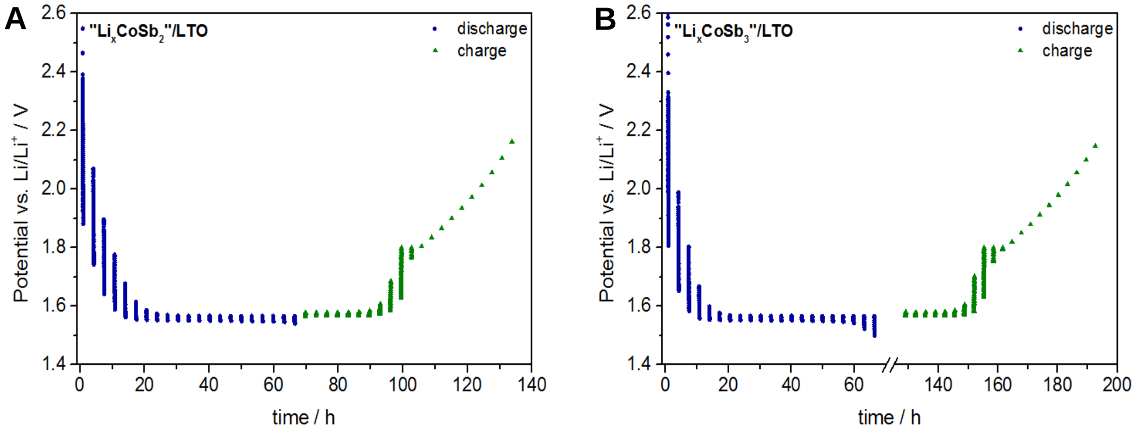

Figure 51: Voltage evolution versus time during discharge and charge of (A) “Li$_x$CoSb$_2$”/LTO and (B) “Li$_x$CoSb$_3$”/LTO

The impedance of “Li$_x$CoSb$_y$”/LTO lithium-ion batteries was determined via an AC measurement technique, namely potentio electrochemical impedance spectroscopy (PEIS). The obtained impedance diagrams were fitted with a Z Fit EC-LAB® software using equivalent electrical circuits. Figure 52 shows the equivalent electrical circuit used to fit the data acquired for the “Li$_x$CoSb$_y$”/LTO lithium-ion batteries, where R$_e$ is the resistance of the electrolyte, R$_{ct}$ is the charge transfer resistance, CPE is the constant phase element and W is the Warburg element.

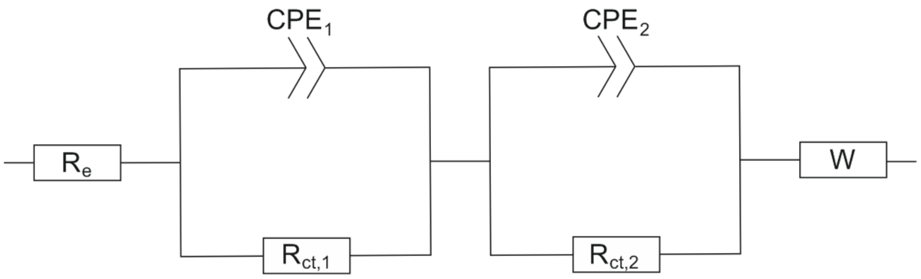

Figure 52: Equivalent electrical circuit for a “Li$_x$CoSb$_y$”/LTO lithium-ion battery

Figure 53 shows the evolution of the charge transfer resistance (R$_{ct,2}$) and of the exponent (a) of the constant phase element (CPE$_2$) over the number of GCPL-PEIS cycles, which were obtained from AC measurements after galvanostatic discharging and charging. In all cases, the exponent of the constant phase element was in the range of 0.6-0.8 and therefore showed a behavior between a Warburg element (a = 0.5) and an ideal capacitor (a = 1).

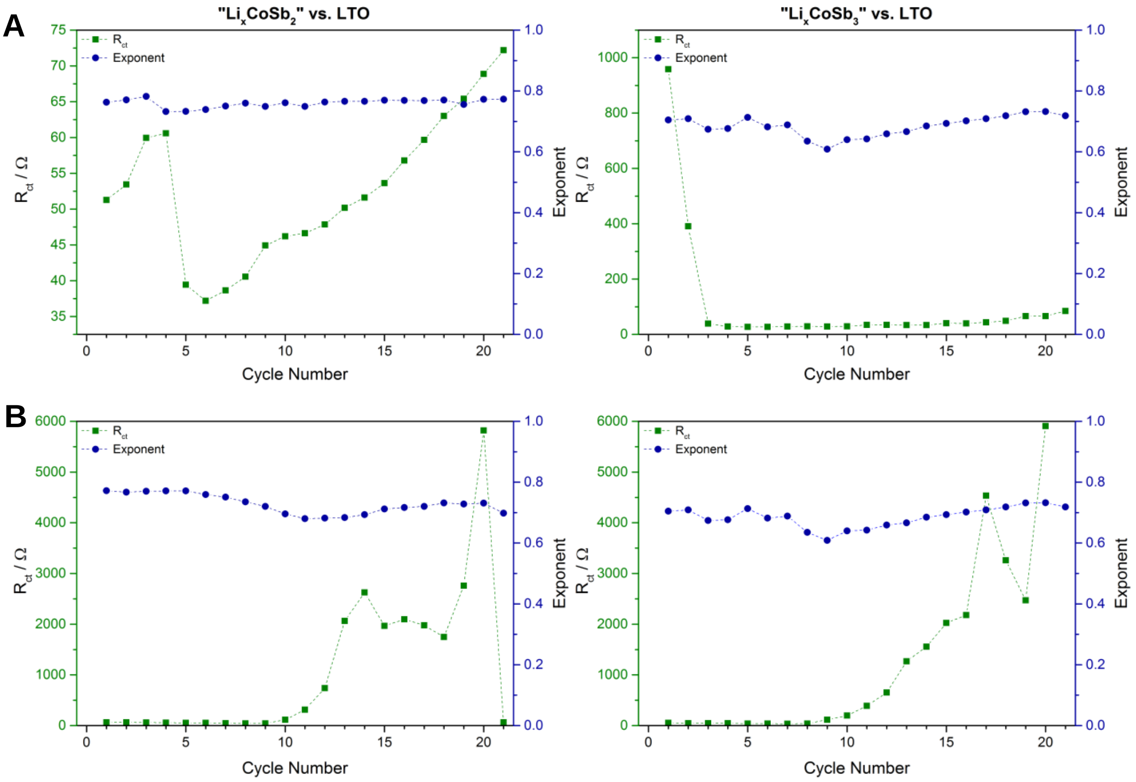

Figure 53: Evolution of the charge transfer resistance (R_{ct}) and the exponent of the constant phase element as function of the number of GCPL-PEIS cycles for "Li$_x$CoSb$_2$"/LTO and "Li$_x$CoSb$_3$"/LTO lithium-ion batteries after (A) discharging and (B) charging.

The chemical diffusion coefficient of Li^+ in the electrode materials ($Li_4Ti_5O_{12}$, $CoSb_2$, $CoSb_3$) was determined from PEIS measurements via the Warburg impedance (Warburg diffusion element, Z_W) and the modulus of the Warburg element (T_W). The impedance of the Warburg diffusion element as function of frequency $Z_W(\omega)$ for a single charge carrier is given by[117]

$$Z_W\,(\omega) = (j\omega T_W)^{-0.5}$$

(Eq. 6)

where j is the imaginary number, ω is the angular frequency in rad/s, T_W is the modulus of the Warburg element in $\Omega\ s^{-1/2}$.

The modulus of the Warburg element T_W was determined from the slope of the imaginary part of the impedance Z versus $1/\omega^{1/2}$ derived from Eq. 6. According to Hanzu et al., the chemical diffusion coefficient was calculated from[117]

$$T_W = \frac{RT}{n^2F^2AC\sqrt{2D}} \tag{Eq. 7}$$

where R is the ideal gas constant in J mol^{-1} K^{-1}, T is the absolute temperature in K, n is the number of exchanged electrons, F is the Faraday constant in As mol^{-1}, A is the active electrode area in cm², C is the concentration of inserted species in mol cm^{-3}, D is the chemical diffusion coefficient in cm² s^{-1}.

The active electrode areas were estimated from the average particle sizes of LTO (2.4±0.1 µm), $CoSb_2$ (2.6±0.4 µm) and $CoSb_3$ (4.1±1.2 µm), which were determined via dynamic light scattering. Assuming spherical particles, the electrode areas were determined to be in the range of 3.8-12.8 cm² for an electrode disk 9.5 mm in diameter. The concentration of inserted Li ions in the solid was determined by peak integration of the reduction peak of the second cycle of the cyclic voltammogram with respect to time.

Table 7 shows the chemical diffusion coefficients D of Li^+ in the examined electrode materials determined via PEIS measurement. The chemical diffusion coefficient of Li^+ in the lithium titanate host lattice was determined to be $(7.6\pm4.0)\times10^{-13}$ cm²/s, which matches quite well with the values obtained by the Randles-Sevcik method (10^{-12}-10^{-14} cm²/s) and the values reported in the literature (10^{-8}-10^{-15} cm²/s).[51,107–109] The chemical diffusion coefficients of Li^+ in the cobalt antimonides were determined to be in a similar range of 10^{-13}-10^{-14} cm²/s but slightly lower compared to lithium titanate. The values were found to be two to three orders of magnitude lower compared to the chemical diffusion coefficients obtained by the Randles-Sevcik method (10^{-11} cm²/s).

Table 7: Chemical diffusion coefficient D of Li^+ in various electro-active materials determined via potentio electrochemical impedance spectroscopy

Electro-Active Material	A [cm²]	C [mol/cm³]	Diffusion Coefficient D [cm²/s]
$Li_4Ti_5O_{12}$	12.8	7.2×10^{-4}	$(7.6\pm4.0)\times10^{-13}$
$CoSb_2$	5.6	4.3×10^{-3}	$(4.3\pm5.0)\times10^{-14}$
$CoSb_3$	3.8	4.5×10^{-3}	$(1.3\pm1.4)\times10^{-13}$

2.2.4 Electrode Materials for Solar Battery Hybrid Devices

In order to fabricate solar battery hybrid devices pre-lithiated electrode materials were required. Hence, either the positive or the negative electrode needed to be lithiated prior to assembling of the solar battery hybrid device. This was necessary since a lithiation process after assembling was not possible. For this purpose, pouch-type cells in two-electrode configuration were assembled consisting of the respective composite electrode material ($Li_4Ti_5O_{12}$, $CoSb_2$, $CoSb_3$) as working electrode and lithium metal as counter and reference electrode. Subsequently, GITT experiments comprising a series of negative galvanostatic current pulses at a C-rate of C/20 interrupted by relaxation periods (30 min) were performed for the pre-lithiation process. Consequently, the lithiated electrode materials were used as positive and negative electrode in the integrated solar battery hybrid devices.

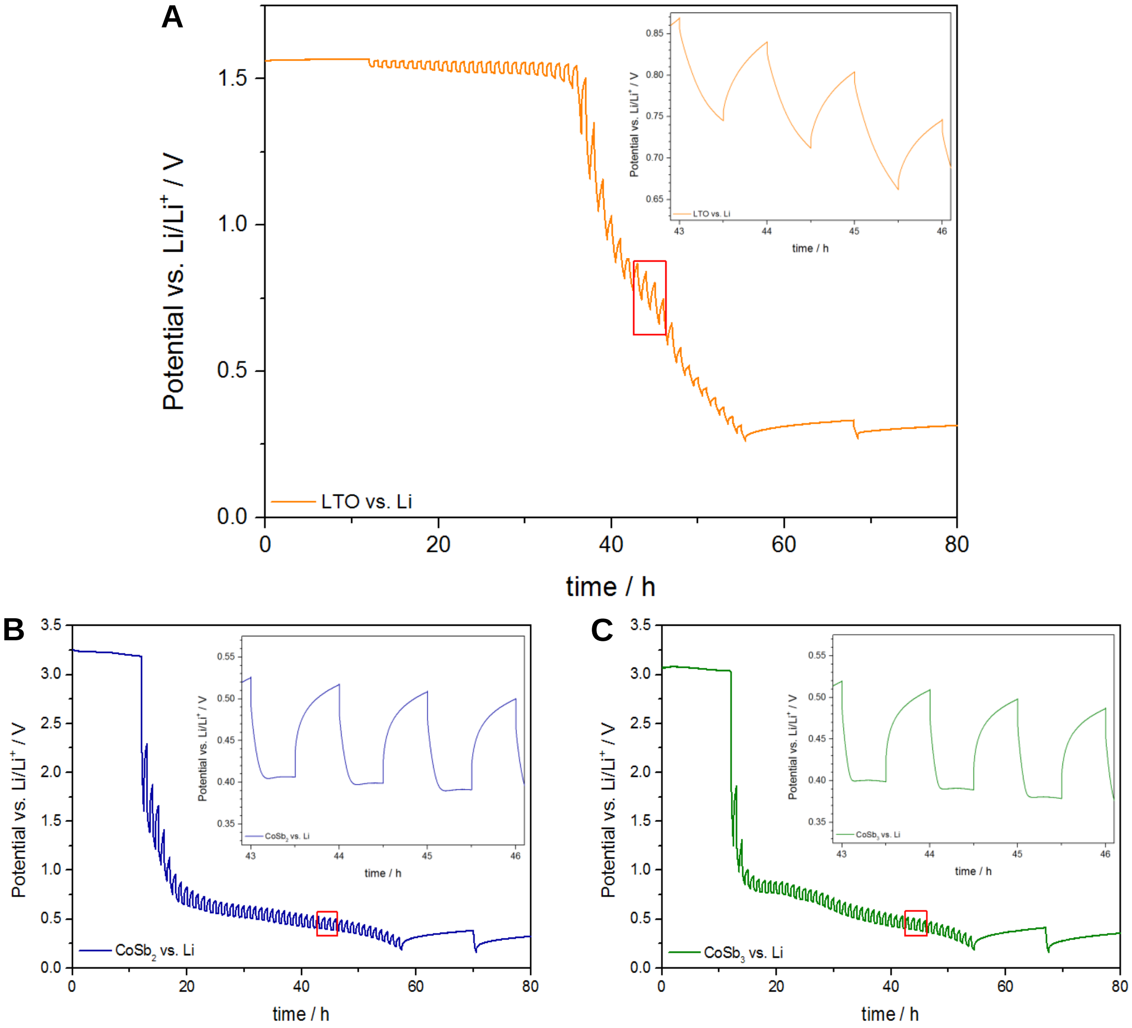

Figure 54: Galvanostatic intermittent titration technique curves for the pre-lithiation of (A) LTO, (B) $CoSb_2$ and (C) $CoSb_3$ in pouch-type cells. Insets show potential curves as function of time.

Figure 54 shows GITT curves for pre-lithiation of LTO, $CoSb_2$ and $CoSb_3$. During the galvanostatic discharge pulses, Li ions are inserted into the electrode material. In case of spinel LTO ($Li_4Ti_5O_{12}$) electrodes, the insertion resulted in the formation of rock-salt LTO ($Li_{4+x}Ti_5O_{12}$). In case of $CoSb_y$ electrodes, an irreversible decomposition of the solid takes place concomitant with Li-Sb reactions forming a well-dispersed mixture of a Li_3Sb phase and cobalt via a conversion reaction.[54,57] The plateaus in the GITT graph of $CoSb_3$ can be attributed to the successive formation of Li_2Sb and Li_3Sb phases upon decomposition of the skutterudite structure and Li-Sb reactions.[116]

The chemical diffusion coefficients D of Li^+ in the examined electrode materials were determined from the GITT curves according to Eq. 8 derived from W. Weppner and R. A. Huggins[118]

$$D = \frac{4}{\pi\tau}\left(\frac{m_i\,V_M}{M_i\,S}\right)^2\left(\frac{\Delta E_S}{\Delta E_t}\right)^2 \quad \tau \ll L^2/D$$

(Eq. 8)

where D is the chemical diffusion coefficient of Li^+ in the electrode material in cm²/s, τ is the period of the galvanostatic current pulse in s, m_i is the mass of active material of component i in the electrode in g, V_M is the molar volume in cm³/mol, M_i is the molecular weight of component i in g/mol, S is the electrode surface area in cm², ΔE_s is the change of the steady-state voltage during the current pulse in volt, ΔE_t is the total transient change of the cell voltage during the current pulse in volt.

The surface areas of the electrodes S were estimated from the mean particle sizes of LTO (2.4±0.1 µm), $CoSb_2$ (2.6±0.4 µm) and $CoSb_3$ (4.1±1.2 µm), which were determined via dynamic light scattering. Assuming spherical particles, the electrode surface areas were determined to be in the range of 11-73 cm².

Table 8 shows that the chemical diffusion coefficients of Li^+ in the electrode materials were in a similar range of 10^{-14} cm²/s but higher for lithium titanate compared to the cobalt antimonides. The Li^+ diffusion coefficient in lithium titanate matched quite well with the values reported in the literature (10^{-8}-10^{-15} cm²/s) and with the ones obtained from cyclic voltammetry via the Randles-Sevcik method (10^{-12}-10^{-14} cm²/s).[51,107–109] Moreover, the Li^+ diffusion coefficient was one order of magnitude lower compared to the values obtained from the Warburg impedance (PEIS). The chemical diffusion coefficients of Li^+ in the cobalt antimonides were up to three orders of magnitude lower compared to the values obtained from the Randles-Sevcik method (10^{-11} cm²/s) but were found to be in a good agreement with the values obtained from the Warburg impedance (10^{-13}-10^{-14} cm²/s).

Table 8: Chemical diffusion coefficient D of Li^+ in various electro-active materials determined via galvanostatic intermittent titration technique

Electro-Active Material	**S [cm²]**	**V_M [cm³/mol]**	**Diffusion Coefficient D [cm²/s]**
$Li_4Ti_5O_{12}$	73	43.7	$(5.2\pm5.5)\times10^{-14}$
$CoSb_2$	17	18.1	$(2.6\pm3.1)\times10^{-14}$
$CoSb_3$	11	18.5	$(1.7\pm1.5)\times10^{-14}$

2.3 Solar Battery Hybrid Devices

An integrated power pack based on the combination of an organic photovoltaic and a battery system was made for efficient energy harvesting and storage in a three-terminal assembly with two positive and a shared negative electrode. The power system was made of an organic multi-junction solar cell connected in series with a lithium-ion battery. In detail, the lower part of the integrated hybrid device consisted of an organic multi-junction solar cell comprising PCDTBT:[70]PCBM (1:2 w/w) active layers with Al/MoO_3 or Ag/MoO_3 intermediate layers and a Ti/Cu electrode with circular geometry (0.79 cm^2 active area). Cu leads were attached to the ITO layer (positive electrode) and to the Ti/Cu top electrode (negative electrode) of the tandem solar cell providing electrical contact. The battery system in the center of the power pack, which was assembled on top of the multi-junction solar cell, based on a combination of (i) pre-lithiated $CoSb_y$ (“Li_xCoSb_y”, y = 2,3) and LTO or (ii) pre-lithiated LTO ($Li_{4+x}Ti_5O_{12}$) and $CoSb_y$ (y = 2,3) electrodes. The pre-lithiation process of the electrode materials was carried out in two-electrode pouch-cells via GITT prior to assembling of the hybrid device since lithiation by an external lithium source after assembling was not possible. The upper part consisted of a current collector comprising a glass / ITO / Cu substrate with a Cu lead attached to the metal contact (positive electrode) to provide electrical contact to the battery system. Figure 55 shows a schematic representation in cross section of the design of the solar battery hybrid power pack.

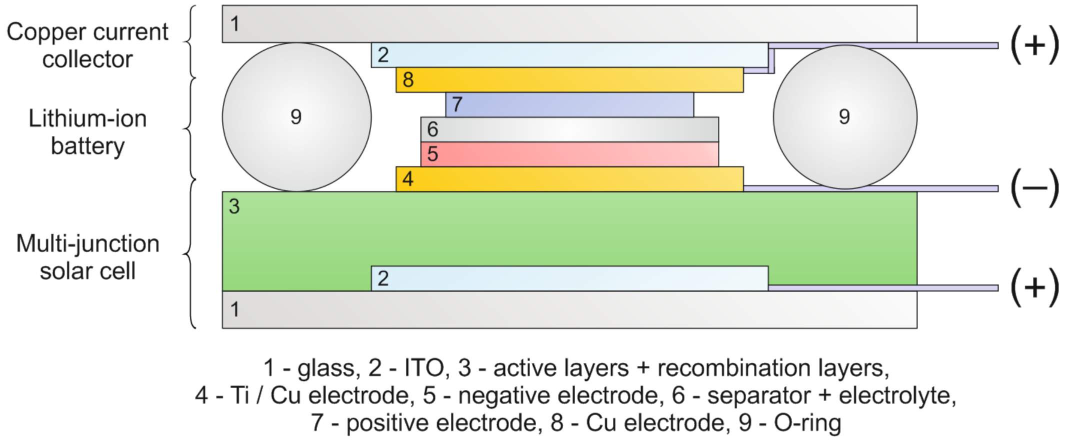

Figure 55: Basic design of the integrated solar battery hybrid power pack in cross section. Two possible configurations can be distinguished: (i) The negative electrode refers to pre-lithiated “Li_xCoSb_y” (y = 2,3) and the positive electrode to the LTO electrode. (ii) The negative electrode refers to $CoSb_y$ and the positive electrode to the pre-lithiated LTO electrode.

Figure 56 shows various components of the integrated power pack such as the current collector, the multi-junction solar cell as well as the fully-assembled solar battery hybrid device. The power pack was assembled and sealed under argon atmosphere by applying pressure onto the O-ring using Plexiglas® plates fixed with screws.

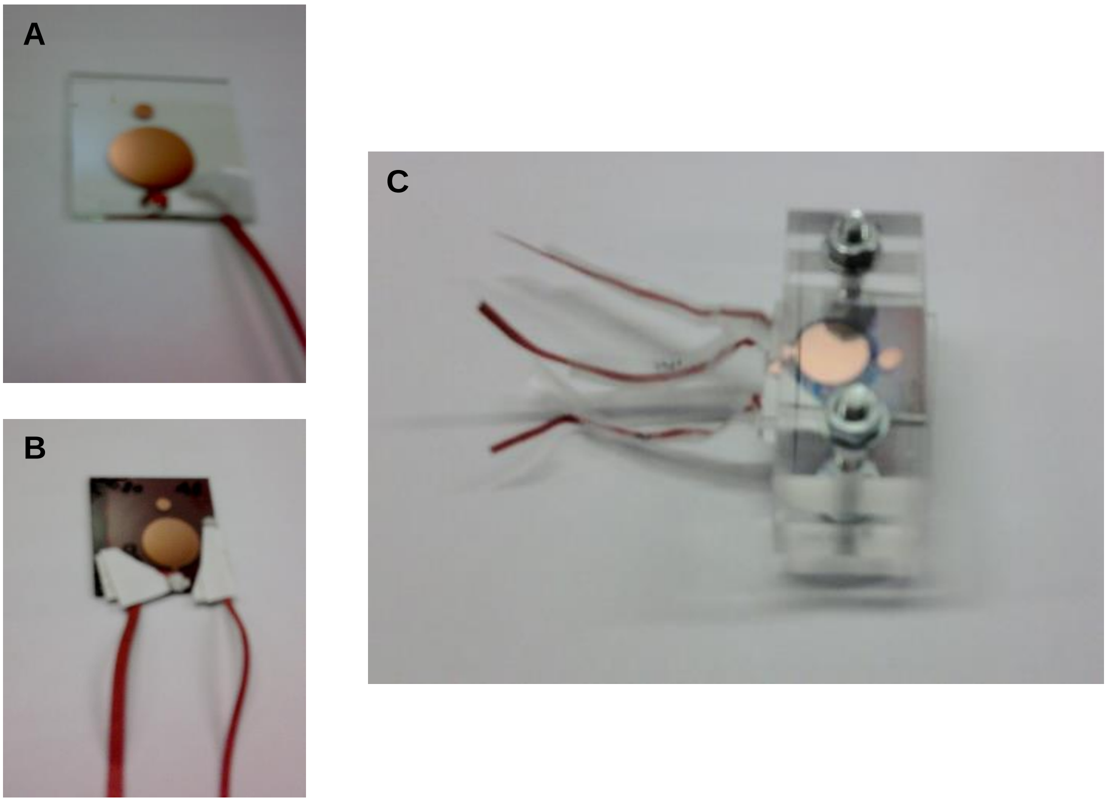

Figure 56: (A) Current collector with a Cu lead, (B) multi-junction solar cell with Cu leads and (C) a fully-assembled solar battery hybrid device

Hybrid device fabrication, characterization and testing were done on the basis of three model systems including “Li_xCoSb_2”/LTO, “Li_xCoSb_3”/LTO and $CoSb_2/Li_{4+x}Ti_5O_{12}$. The three-terminal assembly of the integrated hybrid device allowed the investigation of the performance of both photovoltaic and lithium-ion battery sub-devices. The solar cell performance was evaluated based on J-V curves and photovoltaic characteristic parameters. The performance of the battery system was determined by galvanostatic cycling measurements giving information about the cycling stability and the electrochemical performance.

2.3.1 Performance of Solar Battery Hybrid Devices

The performance of the photovoltaic system in the integrated solar battery hybrid device was determined via I-V measurements. The corresponding J-V characteristics showed that the device performance, in particular the V_{OC}, significantly dropped after the galvanostatic cycling measurements compared to the initial values after the solar cell fabrication. For example, the V_{OC} dropped from 1.24 V to 0.05 V (for a tandem solar cell with Ag/MoO_3 intermediate layers combined with “Li_xCoSb_2”/LTO) and from 1.38 V to 0.41 V (for a tandem solar cell with Al/MoO_3 intermediate layers combined with “Li_xCoSb_3”/LTO). In order to determine the problematic process step responsible for the drop of the J-V characteristics, I-V measurements were performed at several stages of the fabrication process, e.g. after fabrication of the tandem solar cell, after attachment of Cu leads to the metal contact of the tandem solar cell, after assembling of the hybrid device and after the GCPL measurement (Figure 57).

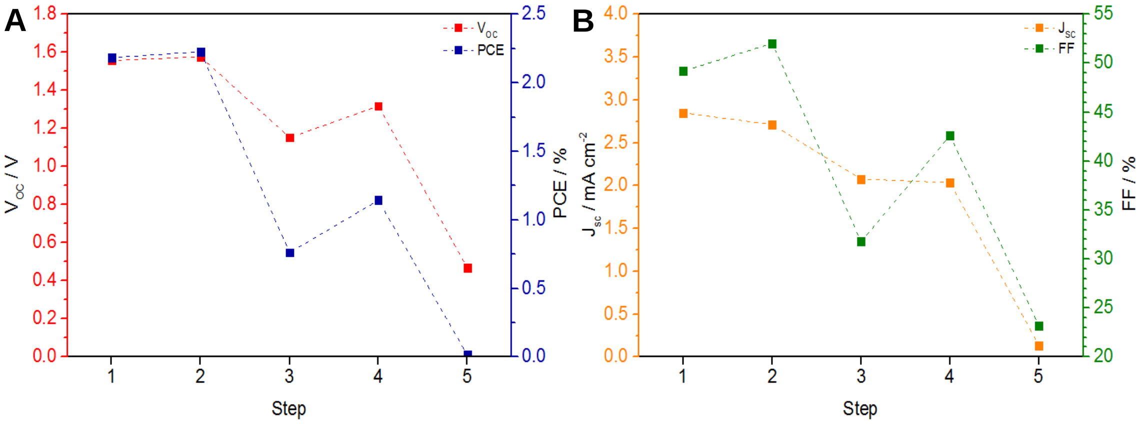

Figure 57: (A) Open circuit voltage and power conversion efficiency, and (B) short-circuit current density and fill factor of a multi-junction solar cell assembled with a $CoSb_2$ vs. $Li_{4+x}Ti_5O_{12}$ lithium-ion battery. I-V measurements were performed at several stages of the fabrication process: Step 1: after fabrication of the tandem solar cell; Step 2: after contacting with Cu leads; Step 3: after drop-coating of $CoSb_2$; Step 4: after assembling of the hybrid device; Step 5: after GCPL measurement.

Figure 57 shows that the solar cell performance significantly decreased from the initial values after the fabrication of the solar cell to the final I-V measurements (for a tandem solar cell with Al/MoO_3 intermediate layers combined with $CoSb_2$/$Li_{4+x}Ti_5O_{12}$). Especially after assembling of the hybrid device (step 4), the open circuit voltage dropped down to values below 0.5 V, which might be due to the contact of the solar cell with the electrolyte (1 M $LiPF_6$ in EC:DMC (1:1, v/v), BASF) of the battery.

In order to investigate the effect of the electrolyte on the solar cell performance, in particular on the open circuit voltage, a Whatman^{TM} glass microfiber filter GF/B (GE Healthcare Life Sciences) soaked with electrolyte was placed on the top electrode of a tandem solar cell and sealed under argon atmosphere using a similar approach as described for the assembling of hybrid devices (Chapter 3.4.2). No temporary effect on the device performance was determined but after three days, a drop in V_{OC} from 1.48 V to 0.67 V and hence in PCE from 2.68% to 1.08% was obtained resulting from the effect of the electrolyte.

In general, the battery system should be operated in a voltage regime matching with the V_{mpp} of the tandem solar cell. This implies that the lithium-ion battery within the hybrid device needed to be run in the range of 0.3-1.1 V (for “Li_xCoSb_2”/LTO and $CoSb_2/Li_{4+x}Ti_5O_{12}$) and 0.2-1.15 V (for “$Li_xCoSb_3$”/LTO). Thus, a minimum V_{mpp} of 1.10-1.15 V was required for charging the lithium-ion battery system during illumination of the solar cell. The results show that the V_{mpp} of the photovoltaic system (below 0.25 V) was too low for charging the lithium-ion battery.

In addition, the cycling performance and electrochemical behavior of the lithium-ion battery was examined by galvanostatic cycling measurements after assembling of the hybrid device. Figure 58 shows the discharge/charge cycling performance as well as the Coulombic efficiency of “Li_xCoSb_2”/LTO, “Li_xCoSb_3”/LTO and $CoSb_2/Li_{4+x}Ti_5O_{12}$ lithium-ion batteries in fully-assembled hybrid devices.

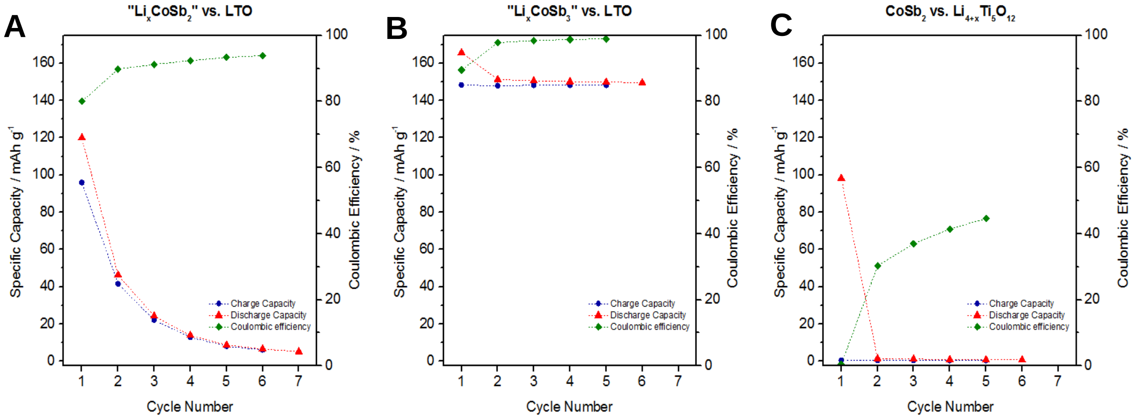

Figure 58: Discharge and charge cycling performance as well as the Coulombic efficiency of (A) “Li_xCoSb_2” vs. LTO, (B) “Li_xCoSb_3” vs. LTO, and (C) $CoSb_2$ vs. $Li_{4+x}Ti_5O_{12}$

Considering the lithium-ion battery systems assembled in integrated power packs, the “Li_xCoSb_2”/LTO battery showed a quite moderate initial discharge/charge capacity (120 / 96 mAh/g) but a poor cycling performance with a rapid capacity fading in the first cycles down to 5.2 / 6.2 mAh/g. The battery exhibited a relatively high initial Coulombic efficiency (80%), which stabilized over 90% after the initial cycle. Moreover, a huge polarization of about 200-300 mV was obtained for this system exceeding the value found for the full-cell assembly in three-electrode Swagelok cells (50-70 mV, Chapter 2.2.3.2). The “Li_xCoSb_3”/LTO battery showed an improved cycling performance compared to the “Li_xCoSb_2”/LTO system having a high initial discharge/charge capacity (166 / 148 mAh/g), which stabilized over 150 mAh/g in the subsequent cycles. Moreover, a quite high initial Coulombic efficiency of 90% was determined stabilizing between 98-99% in the following cycles. Similar to the “Li_xCoSb_2”/LTO system, huge polarization effects (about 250-350 mV) were found compared to the three-electrode Swagelok cell assembly (40-60 mV, Chapter 2.2.3.2). The $CoSb_2$/$Li_{4+x}Ti_5O_{12}$ battery showed a quite low initial discharge/charge capacity (98.1 / 0.5 mAh/g) with a rapid capacity fading down to values below 1 mAh/g accompanied with low Coulombic efficiencies in the range of 0.5-45%. Obviously, this system did not work.

The performance of the solar battery hybrid device, namely the charging of the lithium-ion battery upon illumination of the organic multi-junction solar cell and discharging under dark conditions could not be measured, which is based on two main aspects. On the one hand tandem solar cells showed a poor device performance with V_{mpp}s below 0.25 V after long-term contact with the electrolyte of the lithium-ion battery. This is too low for charging the lithium-ion battery upon illumination of the photovoltaic system. On the other hand some lithium-ion batteries showed a poor cycling performance with rapid capacity fading and thus were not applicable for being charged with the tandem solar cell. As a consequence, several problems need to be overcome when assembling such an integrated power pack such as

- the choice of electrolyte since negative effects on the solar cell performance were determined upon long-term contact with the multi-junction solar cell

- to avoid piercing of the top electrode of the tandem solar cell with sharp edges of the copper current collector of the pre-lithiated “Li_xCoSb_y” electrode material. This problem can be met by introducing a conductive intermediate layer such as an adhesive copper foil or conductive paper, or via drop-coating of the $CoSb_y$ slurry as done in one of the model systems.

- the conditions for sealing of the power pack: The hybrid device should be assembled in an air and moisture free atmosphere, i.e. argon atmosphere, since lithium reacts in moist air under formation of a coating of lithium hydroxide ($LiOH$ and $LiOH\cdot H_2O$), lithium nitride (Li_3N) and lithium carbonate (Li_2CO_3).[119]

- the sealing method: Hybrid devices were sealed with O-rings placed between the tandem solar cell and the glass / ITO / Cu current collector, followed by applying pressure onto the O-ring using Plexiglas® plates fixed with screws. The inner diameter of the O-ring should be large enough to avoid direct contact to the top electrode of the tandem solar cell since a pressure applied on the electrode might destroy the solar cell. The applied pressure should be high enough to provide proper sealing in order to avoid reactions with the ambient atmosphere and to provide a good contact within the lithium-ion battery but low enough to prevent piercing of the tandem solar cell with the electrode materials. Alternatively, the hybrid device could be encapsulated under argon atmosphere using epoxy in order to provide enhanced sealing properties.

These aspects are important since major problems occurred during assembling of hybrid devices. Some tandem solar cells, for example, were destroyed by piercing with the electrode material, by pressing the O-ring on the top electrode or by the effect of the electrolyte. In addition to that, some lithium-ion batteries showed poor electrochemical performance upon galvanostatic cycling, which might be due to inappropriate sealing and contact with ambient atmosphere during long-term storage or by contact problems of the electrode materials with the current collectors.

3 Experimental

3.1 Chemicals and Materials

Table 9 to Table 11 show a summary of used chemicals and materials including their purity grade and supplier. All chemicals and materials were used without further purification unless otherwise stated.

Table 9: List of chemicals

Chemicals	Purity Grade and Description	Supplier
acetone	puriss.	Sigma-Aldrich
aluminum, Al	99.999%, pellets	Kurt J. Lesker Company
antimony, Sb	99.5% (metal basis), powder, ~ 325 mesh	Alfa Aesar
calcium, Ca	99%, granular, ~ 6 mesh	Sigma-Aldrich
cesium carbonate, Cs_2CO_3	99.995% (trace metal basis)	Aldrich Chemistry
chlorobenzene (CB)	99.9%, CHROMASOLV®, for HPLC	Sigma-Aldrich
cobalt, Co	purum, powder	-
copper, Cu	99.9+%, wire, 1.0 mm diam.	Sigma-Aldrich
1,2-dichlorobenzene (DCB)	99%, CHROMASOLV®	Sigma-Aldrich
ethanol	-	-
F8T2	-	ADS

Table 10: List of chemicals (continued)

Chemicals	Purity Grade and Description	Supplier
gold, Au	24 carats, pellets	Ögussa
graphite	C-NERGY^{TM} KS 6L Graphite, conductive carbon	Timcal
ICBA	99%	Solenne
lithium, Li	99.9% (trace metal basis), ribbon, 0.38 mm × 23 mm	Aldrich Chemistry
lithium fluoride, LiF	-	-
lithium titanate, $Li_4Ti_5O_{12}$	LTO EXM 1037, powder	Süd-Chemie
LP 30 electrolyte	1 M $LiPF_6$ in EC:DMC (1:1, v/v)	BASF
Kynar® 761, Kynar Flex® 2801	polyvinylidene fluoride resin	Arkema
1-methyl-2-pyrrolidinone (NMP)	99.5%, anhydrous	Sigma-Aldrich
molybdenum(VI) oxide, MoO_3	99.99% (trace metal basis), 99.98% (trace metal basis)	Sigma-Aldrich
[60]PCBM	99%	Solenne
[70]PCBM	99%	Solenne
PCDTBT	OS 0502	One Material
PCPDTBT	OS 0340	One Material
2-propanol	puriss. p.a., ACS reagent, reag. ISO, reag. Ph. Eur., ≥ 99.8% (GC)	Sigma-Aldrich
PSiF-DBT	OS 0927	One Material
silver, Ag	wire	-
Super C65	conductive carbon	Timcal
titanium, Ti	99.99% (metals basis), wire, 1.0 mm diam.	Sigma-Aldrich, abcr
zinc, Zn	wire	-

Table 11: List of materials

Materials	Purity Grade and Description	Supplier
copper	foil	Coppertex® Daubert VCI. Inc.
copper	99.9%, foil, 17.5 µm	Goodfellow Cambridge Limited
copper	foil, 50 µm, with Cu treatment	Schlenk
FB 2190	separator	Freudenberg
ITO-coated glass	$\leq 10\ \Omega$, 24 × 75 × 1.1 mm	Xinyan Technology co,. Limited
microscope slide	ISO 8037/1, ca. 76 × 26 mm	Roth
O-ring	FPM, 9.5 mm or 14 mm ID	-
pouch foil	-	Dai Nippon Printing Co., Ltd.
Quick Set Epoxy Adhesive	-	RS Components
silver conductive paint	-	RS Components, Conrad
Whatman™ glass microfiber filters GF/B	-	GE Healthcare Life Sciences

3.2 Bulk-Heterojunction Solar Cells

3.2.1 General Procedure for Preparation of Bulk-Heterojunction Solar Cells

Bulk-heterojunction single- and multi-junction solar cells prepared in normal device architecture were used for the determination of the device performance and as photovoltaic system for the integrated solar battery hybrid device. A general procedure for the device fabrication is summarized in following chapters.

3.2.1.1 Cleaning and Activation of the ITO Layer

ITO-coated glass (Xinyan Technology co,. Limited) with a sheet resistance $\leq 10\ \Omega$ was used as substrate for the preparation of solar cells. After removal of a protective foil, the substrates were cleaned with acetone to remove contaminations prior to ultrasonic treatment in 2-propanol (30°C, 30 min, VWR ultrasonic cleaner). Next, the substrates were rinsed with acetone followed by blow-drying with compressed air. The ITO-coated glass substrates were oxygen plasma etched (Femto, Diener Electronics) at a constant oxygen gas flow of 10 sccm for 3 min in order to activate the ITO layer. The cleaned and activated substrates were transferred into a glovebox system (LABmaster dp, MBraun) filled with nitrogen for subsequent process steps.

3.2.1.2 Hole-Transport Layer

MoO_3 (15 nm) was thermally deposited onto activated ITO-coated glass substrates at a rate below 5 Å/s serving as hole-transport layer. Thermal deposition processes of metal and metal oxide layers were performed in an evaporation chamber (MB EVAP, MBraun) equipped with a SQM-160 Deposition Rate/Thickness Monitor (Inficon) recording layer thicknesses and deposition rates at a pressure of approx. 1×10^{-5} mbar unless otherwise stated.

3.2.1.3 Active Layer

The polymer (PCDTBT, PSiF-DBT, PCPDTBT, F8T2) was dissolved in chlorobenzene (10 mg/mL) and stirred overnight to obtain a homogeneous solution. After addition of the fullerene derivative ([60]PCBM, [70]PCBM, ICBA) at varying donor:acceptor ratios, the mixture was stirred for at least 15 min to provide proper mixing. Subsequently, the donor:acceptor blend was doctor bladed onto the glass/ITO/MoO_3 substrate using an Erichsen doctor blading machine (at 40°C, 200 µm casting gap, 7.5 mm/s or 12.5 mm/s), followed by drying at 40°C for slow evaporation of the solvent.

3.2.1.4 Intermediate Layers (for Multi-Junction Solar Cells)

Intermediate layers based on a combination of metal or metal oxides with MoO_3 (15 nm) were deposited onto the active layer. Metals such as Al, Ag, Au, Cu and Ti were thermally deposited with layer thicknesses in the range of 1-4 nm. For evaporation of the metal oxides TiO_x and ZnO, metallic Ti and metallic Zn were thermally deposited (2 nm) onto the active layer under reduced pressure (approx. 10^{-4} mbar) using a BAL-TEC MED020 coating system equipped with a QSG 100 Quartz Film Thickness Monitor unit. Conversion to the respective metal oxides was assumed to occur under ambient atmosphere.[84,85] MoO_3 was thermally deposited on top of the metal or metal oxide layer as described in Chapter 3.2.1.2. Additional metal layers (Ca, Ti) and alkali-metal compound layers (LiF, Cs_2CO_3) were thermally deposited (0.5-1 nm) prior to the physical vapor deposition of the recombination layer in order to investigate the impact of interfacial layers on the device performance. For the preparation of multi-junction solar cells, active layers were doctor bladed onto the intermediate layers as described in Chapter 3.2.1.3.

3.2.1.5 Interfacial Layers and Top Electrodes

Titanium interfacial layers (4 nm) and copper top electrodes (100 nm) were thermally deposited onto the active layer. For single- and multi-junction solar cells, the electrodes were thermally deposited through a shadow mask with square geometry giving an active electrode area of 0.09 cm². For the preparation of multi-junction solar cells for the integrated solar battery hybrid device, a shadow mask with circular geometry (1 cm diam.) was used giving an active electrode area of 0.79 cm².

3.2.2 Characterization

3.2.2.1 I-V Characteristics

I-V curves were monitored under illuminated and dark conditions in the range of 1.5 V to -0.5 V for single-junction, 2.0 V to -2.0 V for tandem, and 3.0 V to -3.0 V for triple-junction solar cells using a Keithley 2400 SourceMeter, a custom-made Lab-View software and a Dedolight DLH400D lamp. The light intensity of the light source was set to 100 mW/cm² providing a spectrum similar to AM 1.5 G. For solar cells with square electrode geometry (0.09 cm² active area), the effective area of the device was defined by shadow masks (3 × 3 mm²), which were put onto the solar cells during the I-V measurements in a custom-made measuring box. Solar cells with circular electrode geometry (0.79 cm² active area) were measured manually with contact pins for the positive and negative electrode. J-V curves were obtained by considering the active electrode area. Thus, photovoltaic characteristic parameters such as V_{OC}, J_{sc}, FF and PCE were determined from the J-V curves and averaged over the best five solar cells. R_s- and R_{sh}-values were extracted from the J-V curves under illumination.

3.2.2.2 UV/VIS-Spectroscopy and Optical Band Gap Determination

Absorption spectra of solar cells, polymer thin films and polymer:fullerene derivative thin films were recorded using a UV/VIS Spectrometer Lambda 35 (Perkin Elmer) equipped with an integrating sphere in the range of 350-1000 nm (slit width: 1 nm, scan speed: 480 nm/min). Solar cells were characterized as prepared. Polymer and polymer:fullerene derivative thin films of various conjugated polymers (PCDTBT, PSiF-DBT, PCPDTBT, F8T2) and fullerene derivatives ([60]PCBM, [70]PCBM, ICBA) were prepared by doctor blading of the respective polymer solution (10 mg/mL, in chlorobenzene) or of the donor:acceptor blend on ultrasonically cleaned (2-propanol, 30°C, 30 min, VWR ultrasonic cleaner) and oxygen plasma etched (3 min, 10 sccm, Femto, Diener Electronics) microscope slides (Roth) in a nitrogen-filled glovebox (LABmaster dp, MBraun), followed by drying at 40°C for slow evaporation of the solvent. Optical band gaps of the polymers were determined from the onset of the absorption spectra.

3.2.2.3 Layer Thickness and Roughness

In order to ascertain the layer thickness and roughness of the solar cells, the samples were scratched with a knife blade, followed by thickness and roughness measurements at four positions using a Dektak XT surface profiler (Bruker; Software: *Vision 64*^{TM}).

3.2.2.4 External Quantum Efficiency (EQE)

EQE measurements were carried out for single-junction solar cells fabricated as described in Chapter 3.2.1. The IPCE (incident photon-to-current efficiency) measuring system consisted of a MuLTImode 4-AT monochromator (Amko) equipped with a xenon lamp (LPS 210-U, Amko) and a Keithley 2400 SourceMeter. In order to contact the ITO layer, the active layer was scratched, followed by applying conductive silver paint. Afterwards, the solar cells were cut into a size of approximately 25 × 25 mm and sealed under nitrogen in a custom made measuring box. After calibration with a photo diode (1.2 mm^2), the EQE spectra of the solar cells (9 mm^2) were monitored in the range of 350-1000 nm.

3.3 Lithium-Ion Battery Electrode Materials

Electro-active materials for lithium-ion batteries such as lithium titanate ($Li_4Ti_5O_{12}$), cobalt diantimonide ($CoSb_2$) and cobalt triantimonide ($CoSb_3$) were used for the preparation of composite electrodes, which were characterized in half- and full-cell configuration using three-electrode Swagelok cells via common electrochemical methods such as cyclic voltammetry (CV), galvanostatic cycling with potential limitation (GCPL), galvanostatic intermittent titration technique (GITT) and potentio electrochemical impedance spectroscopy (PEIS).

3.3.1 Lithium Titanate ($Li_4Ti_5O_{12}$, LTO)

3.3.1.1 Electrode Preparation

The active material LTO EXM 1037 (Süd-Chemie) was dried in a Büchi Glass Oven B-585 (60°C, approx. 10^{-3} mbar) overnight. For the preparation of the composite slurry, 80 wt.% active material, 13 wt.% conductive carbon (Super C65) and 7 wt.% binder (Kynar® 761 or Kynar Flex® 2801) were weighed into a polypropylene vessel and the solvent NMP was added in small portions. The mixture was homogenized in a planetary ball mill (Pulverisette 7, Fritsch) using 10 mm zircona balls at 300 rpm for 4 cycles each with 15 min in forward and reverse operation to obtain a homogeneous, viscous, greyish-black slurry, which was used for the subsequent casting process.

For preparing LTO composite electrodes, the slurry was cast (doctor blade method) with an Erichsen Film Applicator (100 µm, 5 mm/s) on a copper foil (Schlenk), followed by drying of the wet film at 60°C overnight. Next, circular electrodes were punched (9.5 mm diam.), dried in a Büchi Glass Oven B-585 (60°C, approx. 10^{-3} mbar) for at least 6 h and weighed. After further drying at 60°C under reduced pressure, the composite electrodes were transferred into an argon-filled glovebox (MB150 B-G, Braun) with an oxygen and moisture content below 1 ppm, where the electrodes were stored until assembling in Swagelok cells.

3.3.2 Cobalt Diantimonide ($CoSb_2$) and Cobalt Triantimonide ($CoSb_3$)

3.3.2.1 Preparation of $CoSb_2$ and $CoSb_3$ Powders via Mechanical Alloying

$CoSb_2$ and $CoSb_3$ powders were prepared by ball milling of stoichiometric amounts of cobalt and antimony metal powders in a molar ratio of 1:2 (for $CoSb_2$) and 1:3 (for $CoSb_3$) in a planetary ball mill (Pulverisette 7, premium line, Fritsch) with 5 mm zirconia balls under argon atmosphere. The ball to powder weight ratio was 15.2:1. The mechanical alloying process consisted of 48 cycles, each with a 30 min sequence of milling at 600 rpm in forward and reverse operation interrupted by a 15 min resting period. Finally, a black to greyish, slightly shiny powder of $CoSb_2$ and $CoSb_3$ in a quantitative yield was obtained, which was used as active material for subsequent slurry and electrode preparation.

3.3.2.2 Electrode Preparation

For the preparation of the cobalt antimonide composite slurry, 84 wt.% active material ($CoSb_2$ or $CoSb_3$), 10 wt.% conductive carbon (Super C65) and 6 wt% binder (Kynar® Flex 2801) were weighed into a polypropylene vessel and the solvent NMP was added in small portions. The mixture was homogenized in a planetary ball mill (Pulverisette 7, Fritsch) using 10 mm zirconia balls at 300 rpm for 4 cycles each with 15 min in forward and reverse operation to obtain a homogeneous, viscous suspension, which was used for the subsequent casting process.

The slurries were cast (doctor blade) with an Erichsen Film Applicator (100 µm, 5 mm/s) on a Cu foil (Coppertex® Daubert VCI. Inc.), followed by drying of the wet film at 60°C overnight. Next, circular electrodes were punched (9.5 mm diam.), dried in a Büchi Glass Oven B-585 (60°C, approx. 10^{-3} mbar) for at least 8 h and weighed. After further drying at 60°C under reduced pressure, the composite electrodes were transferred into an argon-filled glovebox (MB150 B-G, Braun) with an oxygen and moisture content below 1 ppm, where the electrodes were stored until assembling in Swagelok cells.

3.3.3 Characterization of Electro-Active Materials

3.3.3.1 Dynamic Light Scattering (DLS)

The average particle sizes of LTO EXM 1037, $CoSb_2$ and $CoSb_3$ were determined via dynamic light scattering (DLS) of 0.001 wt.% and 0.01 wt.% particle solutions in ethanol. DLS measurements were performed on a Zetasizer Nano ZS instrument (Malvern Instruments) equipped with a Nano ZS red laser (633 nm) using a Light Scattering Zetasizer software.

3.3.4 Characterization of Electrode Materials in Half-Cell Configuration

All electrochemical characterization measurements in half- and full-cell configuration were performed at room temperature using a multichannel MPG-2 potentiostat (Biologic Science Instruments) with an EC-LAB VIO-34 software unless otherwise stated.

Cyclic voltammetry and galvanostatic cycling experiments were carried out for electrochemical characterization of the prepared $Li_4Ti_5O_{12}$, $CoSb_2$ and $CoSb_3$ composite electrodes. For this purpose, three-electrode Swagelok cells in half-cell configuration were assembled under argon atmosphere using the prepared electrode materials as working electrode and lithium metal as counter and reference electrode. Whatman™ glass microfiber filters GF/B (GE Healthcare Life Sciences) were used as separator. The separator was soaked with a LP 30 electrolyte (BASF), which consisted of a solution of 1 M $LiPF_6$ in a 1:1 (v/v) mixture of ethylene carbonate (EC) and dimethyl carbonate (DMC).

Both experiments started with a 12 h resting period during which an OCV (open circuit voltage) was recorded in order to ensure complete soaking of the separator with the electrolyte providing a good ionic contact prior to electrochemical characterization.

3.3.4.1 Cyclic Voltammetry

Cyclic voltammetry measurements were performed in the range of 1.0-2.0 V vs. Li/Li^+ for LTO and 0.1-2.0 V vs. Li/Li^+ for $CoSb_2$ and $CoSb_3$ using different scan rates (0.1 mV/s, 0.2 mV/s, 0.5 mV/s, 1 mV/s, 2 mV/s and 5 mV/s) with two cycles for each scan rate.

3.3.4.2 Galvanostatic Cycling with Potential Limitation

Galvanostatic cycling experiments were carried out at two different C-rates, namely C/2 and C/5. Using LTO as working electrode, the cells were cycled between 1.0-1.8 V vs. Li/Li^+ for 50 cycles at each C-rate. $CoSb_2$ and $CoSb_3$ half-cells without the initial formation sequence were cycled in the potential range of 0.75 V to 1.1 V vs. Li/Li^+ at C/2 and C/5 each for 50 cycles. $CoSb_2$ and $CoSb_3$ half-cells with the initial formation sequence were cycled for four cycles at C/2 in the potential range of 0.2 to 1.1 V vs. Li/Li^+, followed by 50 cycles at C/2 and 50 cycles at C/5 in the range of 0.75 V to 1.1 V vs. Li/Li^+.

3.3.5 Characterization of Electrode Materials in Full-Cell Configuration

For electrochemical characterization of electrode materials in full-cell configuration, three-electrode Swagelok cells were assembled under argon atmosphere using $CoSb_2$ and $CoSb_3$ as working electrode, LTO as counter electrode and lithium metal as reference electrode. Whatman^{TM} glass microfiber filters GF/B (GE Healthcare Life Sciences) and LP 30 electrolyte (BASF) were used as separator and electrolyte, respectively. In order to ensure complete soaking of the separator with the electrolyte a 12 h resting period was introduced before each electrochemical measurement.

3.3.5.1 Galvanostatic Intermittent Titration Technique

Galvanostatic intermittent titration technique experiments were performed in order to pre-lithiate the $CoSb_2$ and $CoSb_3$ electrodes for subsequent GCPL tests. For this purpose, $CoSb_2$ and $CoSb_3$ were used as working electrode and lithium metal as both counter and reference electrode. The GITT experiments included a series of negative galvanostatic current pulses at a C-rate of C/20, each followed by a relaxation period of 30 min with no current passing through the cell. Pre-lithiated cobalt antimonide electrodes are referred to as “Li_xCoSb_2” and “Li_xCoSb_3” in the following chapters.

3.3.5.2 Galvanostatic Cycling with Potential Limitation

Galvanostatic cycling experiments were carried out at two different C-rates, namely C/2 and C/5, with respect to the LTO electrode material. The full-cells with LTO as working electrode, “Li_xCoSb_2” and “Li_xCoSb_3” as counter electrode and lithium metal as reference electrode were cycled 26 times at each C-rate. The potential limits of LTO (1.3-1.8 V vs. Li/Li^+), “Li_xCoSb_2” (0.65-1.0 V vs. Li/Li^+) and “Li_xCoSb_3” (0.65-1.1 V vs. Li/Li^+) were chosen based on preliminary experiments, giving a limitation for the full-cell of 0.3-1.15 V vs. Li/Li^+ (for “Li_xCoSb_2”/LTO) and 0.2-1.15 V vs. Li/Li^+ (for “Li_xCoSb_3”/LTO).

3.3.5.3 Determination of the Dynamic Resistance and Impedance

The dynamic resistance and impedance of the full-cell configuration were determined using a series of linked DC (direct current) and AC (alternating current) measurement techniques including galvanostatic cycling and potentio electrochemical impedance spectroscopy. The method included a series of negative and positive current pulses at a C-rate of C/2 with respect to the LTO electrode in a voltage range of 1.3-1.8 V vs. Li/Li^+ at the working electrode. Impedance measurements were performed in the range of 200 kHz-10 mHz with a sinus amplitude of 2 mV after each discharge and charge sequence. LTO was used as working electrode, “Li_xCoSb_y” as counter electrode and metallic lithium as reference electrode. Measurements were performed at room temperature using a VMP3 multi-channel potentiostat (Biologic Science Instruments) and an EC-LAB VIO-34 software.

3.3.6 Electrode Materials for Solar Battery Hybrid Devices

$Li_4Ti_5O_{12}$, $CoSb_2$ and $CoSb_3$ electrode materials were pre-lithiated in pouch-type cells (6 × 7 cm, Dai Nippon Printing Co., Ltd.) in two-electrode configuration consisting of the respective composite electrode as working electrode and lithium metal as counter and reference electrode. The electrodes (1.5 × 1.5 cm) were attached on copper current collectors (Goodfellow Cambridge Limited) and dried at 60°C in vacuum (Büchi Glass Oven B-585) prior to assembling under argon atmosphere. FB 2190 (Freudenberg) and LP 30 electrolyte (BASF) were used as separator and electrolyte, respectively.

The electrodes were pre-lithiated via galvanostatic intermittent titration technique. The GITT experiment was started after a 12 h resting period and consisted of a series of negative galvanostatic current pulses with a C-rate of C/20 each one interrupted by relaxation periods of 30 min with no current passing through the cell. The pre-lithiated electrode materials ($Li_{4+x}Ti_5O_{12}$, “Li_xCoSb_2” and “Li_xCoSb_3”) were used for the fabrication of integrated solar battery hybrid devices.

3.4 Solar Battery Hybrid Devices

A general procedure for the preparation of materials for the solar battery hybrid device and for the subsequent assembling and characterization of the integrated power pack is given in following chapters.

3.4.1 Preparation of Materials for Solar Battery Hybrid Devices

3.4.1.1 Multi-Junction Solar Cells

Organic multi-junction solar cells in normal device architecture with a MoO_3 hole-transport layer, PCDTBT:[70]PCBM (1:2 w/w) active layers, Al/MoO_3 or Ag/MoO_3 intermediate layers, a titanium interfacial layer and copper top electrode with circular electrode geometry (0.79 cm² active area) were prepared as described in Chapter 3.2.1. The substrates were cut into a size of approx. 25 × 25 mm. In order to provide electrical contact to the ITO layer (positive electrode) and the Cu top electrode (negative electrode), Cu leads were attached to the metal contact of the tandem solar cell using silver conductive paint, epoxy and paper for electrical insulation.

3.4.1.2 Lithium-Ion Battery Electrode Materials

For integrated solar battery hybrid devices with a “Li_xCoSb_y”/LTO-based lithium-ion battery, the electrode materials ($Li_4Ti_5O_{12}$, $CoSb_2$ and $CoSb_3$) were used as prepared (Chapter 3.3.1-3.3.2) or were pre-lithiated in pouch-type cells (Chapter 3.3.6). For integrated solar battery hybrid devices with a $CoSb_2$/$Li_{4+x}Ti_5O_{12}$-based lithium-ion battery, pre-lithiated LTO (Chapter 3.3.6) and drop coated $CoSb_2$ electrodes were used. For preparation of the $CoSb_2$ slurry for drop coating, 88 wt.% active material ($CoSb_2$) were mixed with the solvent NMP (1:1 w/w with respect to the total amount of solid components of the slurry) in a plastic container on a magnetic stirrer for about 1 h. Conductive carbon (3 wt.% Super C65 and 3 wt.% C-NERGY^{TM} KS 6L Graphite) was added and mixed well overnight. The binder (2 wt.% Kynar Flex$^{®}$ 2801 and 4 wt.% Kynar$^{®}$ 761) was added in small portions over 2 h and mixed over the weekend.

The $CoSb_2$ slurry was directly drop coated onto the copper top electrode of the multi-junction solar cell after contacting with Cu leads, followed by drying at 60°C in drying oven and in a Büchi Glass Oven B-585 (60°C, approx. 10^{-3} mbar) overnight.

3.4.1.3 Copper Current Collectors

Current collectors were prepared by thermal deposition of Cu electrodes with circular geometry (0.79 cm² active area) onto ITO-coated glass substrates (approx. 2.5 × 2.5 cm², Xinyan Technology co,. Limited) after cleaning and activation of the ITO layer as described in Chapter 3.2.1.1. In order to provide an electrical contact, a Cu lead was attached to the metal contact (positive electrode) using silver conductive paint, epoxy and paper for electric insulation.

3.4.2 Assembling of Solar Battery Hybrid Devices

The integrated power pack was assembled and sealed under argon atmosphere. The lower part of the hybrid device was made by the organic multi-junction solar cell with Cu leads in order to provide electrical contact to the ITO layer and the Cu top electrode. For integrated solar battery hybrid devices with a “Li_xCoSb_y”/LTO-based lithium-ion battery, the pre-lithiated “Li_xCoSb_y” electrode (approx. 5 × 5 mm) was placed on the circular top electrode of the solar cell. Next, Whatman™ glass microfiber filters GF/B (8 mm diam., GE Healthcare Life Sciences) were placed on top of the negative electrode, followed by soaking with LP 30 electrolyte (BASF). The LTO electrode (6 mm diam.) was placed on top of the soaked separator. For integrated solar battery hybrid devices with a $CoSb_2/Li_{4+x}Ti_5O_{12}$-based lithium-ion battery, Whatman™ glass microfiber filters GF/B (8 mm diam., GE Healthcare Life Sciences) were placed on top of the $CoSb_2$ electrode, which had already been drop coated on the multi-junction solar cell, followed by soaking with LP 30 electrolyte (BASF). The pre-lithiated $Li_{4+x}Ti_5O_{12}$ electrode (approx. 5 × 5 mm) was placed on top of the soaked separator. The current collector with the Cu lead was placed on top in order to provide electrical contact to the battery system. The whole device was sealed by applying pressure on the O-ring (9.5 mm or 14 mm ID), which was placed between the multi-junction solar cell and the current collector, using Plexiglas® plates fixed with screws.

3.4.3 Characterization

3.4.3.1 I-V Characteristics

I-V measurements of the tandem solar cells (0.79 cm² active area) were performed under illuminated (100 mW/cm², AM 1.5 G) and dark conditions in the range of 2.0 V to -2.0 V at various stages of the fabrication process of the hybrid device as described in Chapter 3.2.2.1. Measurements were performed manually using contact pins for the positive and negative electrode, which were placed on the Cu leads attached to the ITO layer and the Cu top electrode. J-V curves were obtained by considering the active electrode area. Thus, photovoltaic characteristic parameters such as V_{OC}, J_{sc}, FF and PCE were determined from the J-V curves.

3.4.3.2 Galvanostatic Cycling with Potential Limitation

Galvanostatic cycling measurements were performed at room temperature using a multichannel MPG-2 potentiostat (Biologic Science Instruments) with an EC-LAB VIO-34 software. After a 12 h OCV period to ensure sufficient soaking of the separator with the electrolyte, the Li ion test battery in the integrated power pack was cycled five to seven times at a C-rate of C/2 in the potential range of 0.3-1.1 V vs. Li/Li^+ (for “Li_xCoSb_2”/LTO and $CoSb_2/Li_{4+x}Ti_5O_{12}$) and 0.2-1.15 V vs. Li/Li^+ (for “Li_xCoSb_3”/LTO). For “Li_xCoSb_y”/LTO-based systems, “Li_xCoSb_y” served as counter and reference electrode and LTO as working electrode. For $CoSb_2/Li_{4+x}Ti_5O_{12}$-based systems, $CoSb_2$ was used as working electrode and $Li_{4+x}Ti_5O_{12}$ as counter and reference electrode.

4 Summary and Outlook

Integrated power packs combine the advantages of solar energy conversion and storage technologies in a single device comprising a three-terminal assembly with two positive and a shared negative electrode. Such solar battery hybrid devices provide major potential for future applications, for example in self-powering portable and mobile energy systems like mobile phones or wireless sensors.[11,12,14,18] This work introduces a novel concept of an integrated solar battery hybrid device based on the combination of an organic multi-junction solar cell and a low-voltage lithium-ion battery. For this purpose, bulk-heterojunction solar cells and electrode materials for lithium-ion batteries were prepared and characterized, followed by assembling and testing of the integrated power pack.

Bulk-heterojunction (BHJ) single-junction solar cells were prepared in normal device architecture on glass substrates coated with indium tin oxide (ITO) consisting of a MoO_3 hole-transport layer, a blend of conjugated polymers and fullerene derivatives serving as donor and acceptor material, and a titanium/copper top electrode. Different conjugated polymers (PCDTBT, PSiF-DBT, PCPDTBT, F8T2) blended with fullerene derivatives ([60]PCBM, [70]PCBM, ICBA) were evaluated in varying donor:acceptor ratios (1:1 w/w, 1:2 w/w, 1:4 w/w) for the application in BHJ solar cells aiming at a good device performance, in particular a high photo-voltage generation. Amongst the examined donor:acceptor combinations, PCDTBT:[70]PCBM (1:2 w/w)-based solar cells were determined to exhibit the best device performance giving a V_{OC} of 0.87 V, a J_{SC} of 7.86±0.18 mA/cm^2, a FF of 57.3±1.3%, a PCE of 3.86±0.09%, and an external quantum efficiency of 35% (380-580 nm). Single-junction solar cells were further investigated with regard to the effect of the hole-transport layer thickness, the solvent for solution processing and thermal annealing giving following optimized parameters for device fabrication: 15 nm MoO_3, chlorobenzene, and 40°C for slow evaporation of the solvent. Nevertheless, the photo-voltage of the single-junction solar cell was too low for a successful implementation as photovoltaic system in solar battery hybrid devices. This is why organic multi-junction solar cells were prepared in order to supply a voltage exceeding 1.15 V, which is required for charging the low-voltage lithium-ion battery upon illumination of the solar cell.

Tandem solar cells were prepared by stacking PCDTBT:[70]PCBM (1:2 w/w)-based sub-cells with a second sub-cell comprising various donor:acceptor blends. Amongst the examined combinations, the best device performance was obtained using PCDTBT:[70]PCBM (1:2 w/w) as active layer in both sub-cells. In order to investigate the influence of various intermediate layers on the device performance, metals (Al, Ag, Au, Cu, Ti) and metal oxides (TiO_x, ZnO, MoO_3) were combined with MoO_3 serving as electron- and hole-transport layer, respectively. The best photovoltaic characteristics were obtained using a 1 nm Al / 15 nm MoO_3 intermediate layer giving a V_{OC} of 1.78 V, a J_{SC} of 3.71±0.04 mA/cm², a FF of 58.9±0.9%, and a PCE of 3.88±0.03%. Further optimization of the electron- and hole-transport layer thicknesses as well as modification of intermediate layers with additional metal (Ca, Ti) and alkali-metal compound layers (LiF, Cs_2CO_3) did not succeed in improved device performances. However, the photo-voltage provided by PCDTBT:[70]PCBM (1:2 w/w)-based tandem solar cells with Al/MoO_3 intermediate layers upon illumination was in principle high enough to charge the low-voltage lithium-ion battery.

A low-voltage lithium-ion battery with a battery voltage up to 1.15 V vs. Li/Li^+ was chosen as energy storage system of the integrated power pack because of the limitation in the photo-voltage generation by the organic tandem solar cell. For this purpose, composite electrodes based on lithium titanate ($Li_4Ti_5O_{12}$, LTO), cobalt diantimonide ($CoSb_2$) and cobalt triantimonide ($CoSb_3$) were prepared and characterized in half- and full-cell configuration in three-electrode Swagelok cells via common electrochemical methods including cyclic voltammetry (CV), galvanostatic cycling with potential limitation (GCPL), galvanostatic intermittent titration technique (GITT), and potentio electrochemical impedance spectroscopy (PEIS). Lithium titanate showed a very good electrochemical behavior and cycling stability with an initial discharge/charge capacity of 157 / 74 mAh/g, a Coulombic efficiency over 97% after the 10th cycle, a flat voltage plateau at about 1.50-1.55 V vs. Li/Li^+ with very low polarization (below 50 mV) and a specific practical capacity of 112.5 mAh/g, which is significant lower compared to the theoretical capacity (175 mAh/g).[48] The voltage plateau can be attributed to reversible Li ion insertion/extraction processes in the lithium titanate host lattice accompanied by the two-phase transition between spinel and rock-salt LTO.[50,101] $CoSb_2$ and $CoSb_3$ showed an improved electrochemical behavior and discharge/charge capacity as a result of an initial formation sequence with lower potential limits in galvanostatic cycling measurements. This is based on the irreversible decomposition of the $CoSb_y$ (y = 2,3) solid concomitant with the reaction with lithium under formation of a binary Li_3Sb phase well-dispersed in a cobalt matrix during Li ion insertion without reconstruction of $CoSb_y$ upon Li ion extraction.[54,57,112] This irreversible reaction mechanism was supported by CV measurements. However, $CoSb_2$ showed better electrochemical behavior, cycling stability and Coulombic efficiencies during galvanostatic cycling but slightly lower initial discharge/charge capacities (511 / 405 mAh/g) than $CoSb_3$ (526 / 462 mAh/g). The specific practical capacities of both $CoSb_2$ (350 mAh/g) and $CoSb_3$ (373 mAh/g) were lower compared to the theoretical ones ($CoSb_2$: 530 mAh/g[110], $CoSb_3$: 569 mAh/g[111]).

The low-voltage lithium-ion battery with a battery voltage up to 1.15 V vs. Li/Li^+ consisted of lithium titanate as positive electrode and pre-lithiated $CoSb_y$ ("Li_xCoSb_y") as negative electrode. The "Li_xCoSb_2"/LTO battery showed better cycling stability and electrochemical behavior during prolonged galvanostatic cycling but lower discharge/charge capacities (120 / 37 mAh/g) compared to the "Li_xCoSb_3"/LTO battery (146 / 61 mAh/g), which showed a significant higher capacity fading. Both full-cell assemblies showed quite reasonable Coulombic efficiencies over 97% after the 10th cycle. Because of the better characteristics, the "Li_xCoSb_2"/LTO set-up was preferably used as low-voltage lithium-ion battery for solar battery hybrid devices.

Table 12 shows chemical diffusion coefficients of Li^+ in the examined composite electrode materials determined from the Randles-Sevcik method (CV), the Warburg diffusion element (PEIS) and a method derived from W. Weppner and R. A. Huggins (GITT). The chemical diffusion coefficients determined via PEIS and GITT are in good agreement but are up to three orders of magnitude lower compared to the data obtained from the Randles-Sevcik method.

Table 12: Chemical diffusion coefficients of Li^+ in various electrode materials

Electrode Material	**Chemical Diffusion Coefficient D [cm²/s]**		
	CV (Randles-Sevcik)	**PEIS** (Warburg diffusion element)	**GITT** (Weppner-Huggins)
$Li_4Ti_5O_{12}$	1.8×10^{-12} - 6.0×10^{-14}	$(7.6\pm4.0)\times10^{-13}$	$(5.2\pm5.5)\times10^{-14}$
$CoSb_2$	1.1×10^{-11} - 1.4×10^{-11}	$(4.3\pm5.0)\times10^{-14}$	$(2.6\pm3.1)\times10^{-14}$
$CoSb_3$	2.4×10^{-11} - 2.5×10^{-11}	$(1.3\pm1.4)\times10^{-13}$	$(1.7\pm1.5)\times10^{-14}$

The integrated power pack was fabricated by combining an organic multi-junction solar cell with a low-voltage lithium-ion battery in a three-terminal assembly. The lower part consisted of a PCDTBT:[70]PCBM (1:2 w/w)-based tandem solar cell with a Ti/Cu top electrode with circular geometry (0.79 cm^2 active area). The battery system in the center of the power pack was assembled on top of the multi-junction solar cell including a combination of (i) pre-lithiated $CoSb_y$ (“Li_xCoSb_y”) and LTO or (ii) pre-lithiated LTO ($Li_{4+x}Ti_5O_{12}$) and $CoSb_y$ electrodes. The upper part consisted of a current collector made of a glass / ITO / Cu substrate with a Cu lead attached to the metal contact to provide electrical contact to the battery system. The device was assembled and sealed under argon atmosphere by applying pressure onto an O-ring using Plexiglas® plates. The hybrid device was characterized on the basis of the performance of the solar cell and the lithium-ion battery. The results showed that the solar cell characteristics, in particular the open circuit voltage, significantly decreased caused by the influence of the electrolyte (1 M $LiPF_6$ in EC:DMC (1:1, v/v)) of the lithium-ion battery system on the solar cell during long-term contact. With regard to the implemented lithium-ion batteries, only the “Li_xCoSb_3”/LTO battery showed adequate performance during galvanostatic cycling with high initial discharge/charge capacities and Coulombic efficiencies. The other examined battery systems (“Li_xCoSb_2”/LTO, $CoSb_2$/$Li_{4+x}Ti_5O_{12}$) showed poor electrochemical behavior and cycling stability with significant capacity fading.

However, it was not possible to measure the performance of the integrated solar battery hybrid device, namely the charging of the lithium-ion battery upon illumination of the organic tandem solar cell and discharging under dark conditions. This was based on the one hand on the voltage drop of the solar cell caused by the electrolyte during long-term contact. As a consequence, the voltage supplied by the multi-junction solar cell was too low for charging the lithium-ion battery upon illumination requiring a minimum V_{mpp} of 1.15 V. On the other hand, the poor cycling performance with rapid capacity fading upon galvanostatic cycling was problematic and might be due to inappropriate sealing or contact with ambient atmosphere during long-term storage or by contacting problems.

Thus, there is still much effort required to improve the performance of the energy conversion and storage systems as well as to optimize the assembling procedure and packaging process in order to succeed in the fabrication of a working hybrid device.

Further research includes the optimization of the solar cell performance, the characterization of electrode materials and investigations with regard to the fabrication, assembling and packaging procedure of integrated solar battery hybrid devices. The solar cell performance, in particular the generated photo-voltage, needs to be improved in order to combine the photovoltaic system with common lithium-ion electrode materials such as graphite and $LiCoO_2$. This is important for future high-voltage applications such as self-powering and portable electronics. Moreover, appropriate low and wide band gap polymers with complementary absorption behavior need to be evaluated with regard to the application in multi-junction solar cells in order to improve photon harvesting and the device performance.

Further work is required for characterization of the prepared electro-active materials and composite electrodes. X-ray diffraction technique (XRD), for example, enables the determination of the crystal structure of the cobalt antimonide powders and thus provides the possibility to verify the formation of the respective compounds. Brunauer-Emmet-Teller (BET) analysis is a useful method to determine the specific surface area of the electro-active powder materials and the surface area of the prepared composite electrodes. In order to examine the changes in the morphology of the electrodes by insertion/extraction of lithium, the electrode materials can be characterized via scanning electron microscopy (SEM) before and after lithiation. The insertion mechanism of lithium in cobalt di- and triantimonides can be investigated by ^{121}Sb Mössbauer spectroscopy.[120]

With regard to integrated solar battery hybrid devices, several problems need to be overcome especially in terms of assembling and packaging in order to provide an air- and moisture-tight sealing. Piercing of the top electrode of the tandem solar cell with sharp edges of the current collector can be avoided by using conductive intermediate layers or by drop coating of the electrode onto the solar cell. The present sealing method using O-rings requires optimization and alternative sealing strategies need to be investigated such as encapsulation with epoxy. In addition to that, the influence of the electrolyte on the solar cell performance and alternative electrolytes (e.g. solid state electrolytes) need to be examined. Furthermore, the stability of the photovoltaic system, the battery system and the integrated solar battery hybrid device needs to be investigated.

5 References

[1] Key World Energy Statistics, International Energy Agency http://www.iea.org/publications/freepublications/publication/KeyWorld2014.pdf (accessed Aug 15, 2015).

[2] Liu, P.; Cao, Y.; Li, G.-R.; Gao, X.-P.; Ai, X.-P.; Yang, H.-X. *ChemSusChem* **2013**, *6*, 802–806.

[3] Snaith, H. J.; Schmidt-Mende, L. *Adv. Mater.* **2007**, *19*, 3187–3200.

[4] Ameri, T.; Dennler, G.; Lungenschmied, C.; Brabec, C. J. *Energy Environ. Sci.* **2009**, *2*, 347–363.

[5] World Energy Outlook 2013, Renewable Energy Outlook http://www.worldenergyoutlook.org/media/weowebsite/2013/WEO2013_Ch06_Renewables.pdf (accessed Aug 15, 2015).

[6] Energy and the Challenge of Sustainability, World Energy Assessment http://www.undp.org/content/dam/aplaws/publication/en/publications/environment-energy/www-ee-library/sustainable-energy/world-energy-assessment-energy-and-the-challenge-of-sustainability/World Energy Assessment-2000.pdf (accessed Aug 15, 2015).

[7] Chen, H.; Cong, T. N.; Yang, W.; Tan, C.; Li, Y.; Ding, Y. *Prog. Nat. Sci.* **2009**, *19* (3), 291–312.

[8] Luo, X.; Wang, J.; Dooner, M.; Clarke, J. *Appl. Energy* **2015**, *137*, 511–536.

[9] Zhao, H.; Wu, Q.; Hu, S.; Xu, H.; Rasmussen, C. N. *Appl. Energy* **2014**, *137*, 545–553.

[10] Evans, A.; Strezov, V.; Evans, T. J. *Renew. Sustain. Energy Rev.* **2012**, *16* (6), 4141–4147.

[11] Guo, W.; Xue, X.; Wang, S.; Lin, C.; Wang, Z. L. *Nano Lett.* **2012**, 1–5.

[12] Chakrapani, V.; Rusli, F.; Filler, M. A.; Kohl, P. A. *J. Power Sources* **2012**, *216*, 84–88.

[13] Yu, M.; Ren, X.; Ma, L.; Wu, Y. *Nat. Commun.* **2014**, *5*, 5111.

[14] Xu, X.; Li, S.; Zhang, H.; Shen, Y.; Zakeeruddin, S. M.; Graetzel, M.; Cheng, Y.-B.; Wang, M. *ACS Nano* **2015**, *9* (2), 1782–1787.

[15] Westover, A. S.; Share, K.; Carter, R.; Cohn, A. P.; Oakes, L.; Pint, C. L. *Appl. Phys. Lett.* **2014**, *104*, 1–4.

[16] Fu, Y.; Wu, H.; Ye, S.; Cai, X.; Yu, X.; Hou, S.; Kafafy, H.; Zou, D. *Energy Environ. Sci.* **2013**, *6*, 805.

[17] Chien, C.-T.; Hiralal, P.; Wang, D.-Y.; Huang, I.-S.; Chen, C.-C.; Chen, C.-W.; Amaratunga, G. A. J. *Small* **2015**, *11* (24), 2929-2937.

[18] Chen, T.; Qiu, L.; Yang, Z.; Cai, Z.; Ren, J.; Li, H.; Lin, H.; Sun, X.; Peng, H. *Angew. Chem. Int. Ed.* **2012**, *51*, 11977–11980.

[19] Green, M. A. *Phys. E Low-Dimensional Syst. Nanostructures* **2002**, *14* (1-2), 65–70.

[20] Aberle, A. G. *Thin Solid Films* **2009**, *517*, 4706–4710.

[21] Jackson, P.; Hariskos, D.; Lotter, E.; Paetel, S.; Wuerz, R.; Menner, R.; Wischmann, W.; Powalla, M. *Prog. Photovoltaics Res. Appl.* **2011**, *19* (7), 894–897.

[22] Yan, J.; Saunders, B. R. *RSC Adv.* **2014**, *4*, 43286–43314.

[23] Günes, S.; Neugebauer, H.; Sariciftci, N. S. *Chem.Rev.* **2007**, *107*, 1324–1338.

[24] Zhong, Y.; Trinh, M. T.; Chen, R.; Wang, W.; Khlyabich, P. P.; Kumar, B.; Xu, Q.; Nam, C.-Y.; Sfeir, M. Y.; Black, C.; Steigerwald, M. L.; Loo, Y.-L.; Xiao, S.; Ng, F.; Zhu, X.-Y.; Nuckolls, C. *J. Am. Chem. Soc.* **2014**, *136*, 15215–15221.

[25] Etxebarria, I.; Ajuria, J.; Pacios, R. *Org. Electron.* **2015**, *19*, 34–60.

[26] Veldman, D.; Offermans, T.; Sweelssen, J.; Koetse, M. M.; Meskers, S. C. J.; Janssen, R. A. J. *Thin Solid Films* **2006**, *511-512*, 333–337.

[27] Udum, Y.; Denk, P.; Adam, G.; Apaydin, D. H.; Nevosad, A.; Teichert, C.; White, M. S.; Sariciftci, N. S.; Scharber, M. C. *Org. Electron.* **2014**, *15*, 997–1001.

[28] Blom, P. W. M.; Mihailetchi, V. D.; Koster, L. J. A.; Markov, D. E. *Adv. Mater.* **2007**, *19*, 1551–1566.

[29] Tamai, Y.; Ohkita, H.; Benten, H.; Ito, S. *J. Phys. Chem. Lett.* **2015**, *6*, 3417–3428.

[30] Veldman, D.; Meskers, S. C. J.; Janssen, R. A. J. *Adv. Funct. Mater.* **2009**, *19*, 1939–1948.

[31] Heeger, A. J. *Adv. Mater.* **2014**, *26*, 10–28.

[32] Shockley, W.; Queisser, H. J. *J. Appl. Phys.* **1961**, *32* (3), 510–519.

[33] Würfel, P. *Physics in Solar Cells*; Wiley-VCH: Berlin, Germany, 2004.

[34] Ameri, T.; Li, N.; Brabec, C. J. *Energy Environ. Sci.* **2013**, *6*, 2390–2413.

[35] De Vos, A. *J. Phys. D. Appl. Phys.* **1980**, *13*, 839–846.

[36] Wang, Y.; Cao, G. *Adv. Mater.* **2008**, *20*, 2251–2269.

[37] Whittingham, M. S. *Prog. Solid State Chem.* **1978**, *12* (1), 41–99.

[38] Winter, M.; Besenhard, J. O.; Spahr, M. E.; Novák, P. *Adv. Mater.* **1998**, *10* (10), 725–763.

[39] Zaghib, K.; Mauger, A.; Groult, H.; Goodenough, J. B.; Julien, C. M. *Materials (Basel).* **2013**, *6*, 1028–1049.

[40] Buqa, H.; Goers, D.; Holzapfel, M.; Spahr, M. E.; Novák, P. *J. Electrochem. Soc.* **2005**, *152* (2), A474–A481.

[41] Chen, J. S.; Archer, L. A.; Lou, X. W. (David). *J. Mater. Chem.* **2011**, *21*, 9912–9924.

[42] Hwang, H.; Kim, H.; Cho, J. *Nano Lett.* **2011**, *11* (11), 4826–4830.

[43] Rao, B. M. L.; Francis, R. W.; Christopher, H. A. *J. Electrochem. Soc.* **1977**, *124* (10), 1490–1492.

[44] Wang, J.; Raistrick, I. D.; Huggins, R. A. *J. Electrochem. Soc.* **1986**, *133* (3), 457–460.

[45] Arora, P.; Zhang, Z. *Chem. Rev.* **2004**, *104*, 4419–4462.

[46] Zhang, S. S.; Xu, K.; Jow, T. R. *J. Electrochem. Soc.* **2002**, *149* (5), A586–A590.

[47] Marom, R.; Haik, O.; Aurbach, D.; Halalay, I. C. *J. Electrochem. Soc.* **2010**, *157* (8), A972–A983.

[48] Sun, X.; Radovanovic, P. V.; Cui, B. *New J. Chem.* **2015**, *39* (1), 38–63.

[49] Hsiao, K.-C.; Liao, S.-C.; Chen, J.-M. *Electrochim. Acta* **2008**, *53*, 7242–7247.

[50] Ohzuku, T.; Ueda, A.; Yamamoto, N. *J. Electrochem. Soc.* **1995**, *142* (5), 1431–1435.

[51] Zaghib, K.; Simoneau, M.; Armand, M.; Gauthier, M. *J. Power Sources* **1999**, *81-82*, 300–305.

[52] Chen, J.; Yang, L.; Fang, S.; Tang, Y. *Electrochim. Acta* **2010**, *55*, 6596–6600.

[53] Naoi, K.; Ishimoto, S.; Isobe, Y.; Aoyagi, S. *J. Power Sources* **2010**, *195*, 6250–6254.

[54] Park, M.-G.; Song, J. H.; Sohn, J.-S.; Lee, C. K.; Park, C.-M. *J. Mater. Chem. A* **2014**, *2*, 11391–11399.

[55] Xie, J.; Zheng, Y.-X.; Liu, S.-Y.; Song, W.-T.; Zhu, Y.-G.; Cao, G.-S.; Zhu, T.-J.; Zhao, X.-B. *Int. J. Electrochem. Sci.* **2012**, *7*, 1319–1331.

[56] Amornpitoksuk, P.; Suwanboon, S. *J. Alloys Compd.* **2009**, *473*, 373–375.

[57] Alcántara, R.; Fernández-Madrigal, F. J.; Lavela, P.; Tirado, J. L.; Jumas, J. C.; Olivier-Fourcade, J. *J. Mater. Chem.* **1999**, *9*, 2517–2521.

[58] Shrotriya, V.; Li, G.; Yao, Y.; Chu, C.-W.; Yang, Y. *Appl. Phys. Lett.* **2006**, *88*, 073508.

[59] Brunetti, F. G.; Kumar, R.; Wudl, F. *J. Mater. Chem.* **2010**, *20*, 2934–2948.

[60] Xin, H.; Guo, X.; Kim, F. S.; Ren, G.; Watson, M. D.; Jenekhe, S. A. *J. Mater. Chem.* **2009**, *19*, 5303–5310.

[61] Wang, F.; Xu, Q.; Tan, Z.; Li, L.; Li, S.; Hou, X.; Sun, G.; Tu, X.; Hou, J.; Li, Y. *J. Mater. Chem. A* **2014**, *2*, 1318–1324.

[62] Zhang, F.; Zhuo, Z.; Zhang, J.; Wang, X.; Xu, X.; Wang, Z.; Xin, Y.; Wang, J.; Wang, J.; Tang, W.; Xu, Z.; Wang, Y. *Sol. Energy Mater. Sol. Cells* **2012**, *97*, 71–77.

[63] Cheng, P.; Li, Y.; Zhan, X. *Energy Environ. Sci.* **2014**, *7* (6), 2005–2011.

[64] Lin, S.-H.; Lan, S.; Sun, J.-Y.; Lin, C.-F. *Org. Electron.* **2013**, *14* (1), 26–31.

[65] Park, S. H.; Roy, A.; Beaupré, S.; Cho, S.; Coates, N.; Moon, J. S.; Moses, D.; Leclerc, M.; Lee, K.; Heeger, A. J. *Nat. Photonics* **2009**, *3* (5), 297–302.

[66] Yao, Y.; Hou, J.; Xu, Z.; Li, G.; Yang, Y. *Adv. Funct. Mater.* **2008**, *18*, 1783–1789.

[67] Zhang, F.; Jespersen, K. G.; Björström, C.; Svensson, M.; Andersson, M. R.; Sundström, V.; Magnusson, K.; Moons, E.; Yartsev, A.; Inganäs, O. *Adv. Funct. Mater.* **2006**, *16*, 667–674.

[68] Synooka, O.; Eberhardt, K.-R.; Singh, C. R.; Hermann, F.; Ecke, G.; Ecker, B.; von Hauff, E.; Gobsch, G.; Hoppe, H. *Adv. Energy Mater.* **2014**, *4*, 1300981.

[69] Blouin, N.; Michaud, A.; Gendron, D.; Wakim, S.; Blair, E.; Neagu-Plesu, R.; Belletête, M.; Durocher, G.; Tao, Y.; Leclerc, M. *J. Am. Chem. Soc.* **2008**, *130* (2), 732–742.

[70] Muzafarov, A. M.; Bockholt, A. *Silicon Polymers*; Advances in Polymer Science; Springer-Verlag: Berlin, Heidelberg, 2010.

[71] Peet, J.; Kim, J. Y.; Coates, N. E.; Ma, W. L.; Moses, D.; Heeger, A. J.; Bazan, G. C. *Nat. Mater.* **2007**, *6*, 497–500.

[72] Zhao, D. W.; Sun, X. W.; Jiang, C. Y.; Kyaw, A. K. K.; Lo, G. Q.; Kwong, D. L. *Appl. Phys. Lett.* **2008**, *93* (8), 1–4.

[73] Kraffert, F.; Steyrleuthner, R.; Albrecht, S.; Neher, D.; Scharber, M. C.; Bittl, R.; Behrends, J. *J. Phys. Chem. C* **2014**, *118*, 28482–28493.

[74] Troshin, P. A.; Hoppe, H.; Peregudov, A. S.; Egginger, M.; Shokhovets, S.; Gobsch, G.; Sariciftci, N. S.; Razumov, V. F. *ChemSusChem* **2011**, *4*, 119–124.

[75] Kaltenhauser, V. In situ synthesis of metal sulphide / polymer nanocomposites in single junction and tandem solar cells. Dissertation, Graz University of Technology, 2013.

[76] Kim, J. Y.; Lee, K.; Coates, N. E.; Moses, D.; Nguyen, T.-Q.; Dante, M.; Heeger, A. J. *Science* **2007**, *317*, 222–225.

[77] Gilot, J.; Wienk, M. M.; Janssen, R. A. J. *Appl. Phys. Lett.* **2007**, *90*, 143512.

[78] Yakimov, A.; Forrest, S. R. *Appl. Phys. Lett.* **2002**, *80* (9), 1667–1669.

[79] Hiramoto, M.; Suezaki, M.; Yokoyama, M. *Chem. Lett.* **1990**, 327–330.

[80] Chen, F.-C.; Lin, C.-H. *J. Phys. D. Appl. Phys.* **2009**, *43*, 025104.

[81] Dhass, A. D.; Natarajan, E.; Ponnusamy, L. *Proc. - ICETEEEM 2012, Int. Conf. Emerg. Trends Electr. Eng. Energy Manag.* **2012**, 382–386.

[82] Yan, X.; Hao, H.; Chen, Y.; Shi, S.; Zhang, E.; Lou, J.; Liu, B. *Nanoscale Res. Lett.* **2014**, *9* (1), 548.

[83] Brabec, C. J.; Cravino, A.; Meissner, D.; Sariciftci, N. S.; Fromherz, T.; Rispens, M. T.; Sanchez, L.; Hummelen, J. C. *Adv. Funct. Mater.* **2001**, *11* (5), 374–380.

[84] Kasemo, B.; Lausmaa, J. *J. Biomed. Mater. Res.* **1988**, *22* (A2), 145–158.

[85] Tjong, S. C.; Mai, Y.-W. *Physical Properties and Applications of Polymer Nanocomposites*; Woodhead Publishing: Cambridge, 2010.

[86] Dennler, G.; Prall, H.-J.; Koeppe, R.; Egginger, M.; Autengruber, R.; Sariciftci, N. S. *Appl. Phys. Lett.* **2006**, *89* (7), 73502.

[87] Colsmann, A.; Junge, J.; Kayser, C.; Lemmer, U. *Appl. Phys. Lett.* **2006**, *89* (20), 203506.

[88] Janssen, A. G. F.; Riedl, T.; Hamwi, S.; Johannes, H.-H.; Kowalsky, W. *Appl. Phys. Lett.* **2007**, *91*, 073519.

[89] Hadipour, A.; De Boer, B.; Blom, P. W. M. *Adv. Funct. Mater.* **2008**, *18* (2), 169–181.

[90] Sun, X. W.; Zhao, D. W.; Ke, L.; Kyaw, A. K. K.; Lo, G. Q.; Kwong, D. L. *Appl. Phys. Lett.* **2010**, *97*, 053303.

[91] Yuan, Y.; Huang, J.; Li, G. *Green* **2011**, *1*, 65–80.

[92] Ajuria, J.; Etxebarria, I.; Cambarau, W.; Muñecas, U.; Tena-Zaera, R.; Jimeno, J. C.; Pacios, R. *Energy Environ. Sci.* **2011**, *4*, 453–458.

[93] Olthof, S.; Timmreck, R.; Riede, M.; Leo, K. *Appl. Phys. Lett.* **2012**, *100*, 113302.

[94] Fan, X.; Guo, S.; Fang, G.; Zhan, C.; Wang, H.; Zhang, Z.; Li, Y. *Sol. Energy Mater. Sol. Cells* **2013**, *113*, 135–139.

[95] Wang, E.; Wang, L.; Lan, L.; Luo, C.; Zhuang, W.; Peng, J.; Cao, Y. *Appl. Phys. Lett.* **2008**, *92* (3), 033307.

[96] Dennler, G.; Scharber, M. C.; Brabec, C. J. *Adv. Mater.* **2009**, *21*, 1323–1338.

[97] Huang, J.-H.; Lee, C.-P.; Ho, Z.-Y.; Kekuda, D.; Chu, C.-W.; Ho, K.-C. *Sol. Energy Mater. Sol. Cells* **2010**, *94* (1), 22–28.

[98] Reference Solar Spectral Irradiance: Air Mass 1.5 http://rredc.nrel.gov/solar/spectra/am1.5/ (accessed Jul 31, 2015).

[99] Gueymard, C. A.; Myers, D.; Emery, K. *Sol. Energy* **2002**, *73* (6), 443–467.

[100] Chu, T.-Y.; Alem, S.; Verly, P. G.; Wakim, S.; Lu, J.; Tao, Y.; Beaupré, S.; Leclerc, M.; Bélanger, F.; Désilets, D.; Rodman, S.; Waller, D.; Gaudiana, R. *Appl. Phys. Lett.* **2009**, *95*, 063304.

[101] Jiang, Y.-M.; Wang, K.-X.; Zhang, H.-J.; Wang, J.-F.; Chen, J.-S. *Sci. Rep.* **2013**, *3*, 3490.

[102] Kissinger, P. T.; Heineman, W. R. *J. Chem. Educ.* **1983**, *60* (9), 702–706.

[103] Xu, W.; Wang, J.; Ding, F.; Chen, X.; Nasybulin, E.; Zhang, Y.; Zhang, J.-G. *Energy Environ. Sci.* **2014**, *7*, 513–537.

[104] Bard, A. J.; Faulkner, L. R. *Electrochemical Methods: Fundamentals and Applications*; John Wiley & Sons: New York, 1980.

[105] Lindström, H.; Södergren, S.; Solbrand, A.; Rensmo, H.; Hjelm, J.; Hagfeldt, A.; Lindquist, S.-E. *J. Phys. Chem. B* **1997**, *101*, 7717–7722.

[106] Holzapfel, M. Lithium Titanium Spinel - $Li_4Ti_5O_{12}$, An Inherently Safe Anode Material for Lithium Ion Batteries – EXM 1037 http://www.phostechlithium.com/documents/TechnicalDataSheetEXM1037.pdf (accessed Jul 18, 2015).

[107] Rho, Y. H.; Kanamura, K. *J. Solid State Chem.* **2004**, *177*, 2094–2100.

[108] Kavan, L.; Procházka, J.; Spitler, T. M.; Kalbáč, M.; Zukalová, M.; Drezen, T.; Grätzel, M. *J. Electrochem. Soc.* **2003**, *150* (7), A1000–A1007.

[109] Takami, N.; Hoshina, K.; Inagaki, H. *J. Electrochem. Soc.* **2011**, *158* (6), A725–A730.

[110] Xie, J.; Zhao, X. B.; Cao, G. S.; Zhong, Y. D.; Zhao, M. J.; Tu, J. P. *Electrochim. Acta* **2005**, *50*, 1903–1907.

[111] Zhu, J.; Sun, T.; Chen, J.; Shi, W.; Zhang, X.; Lou, X.; Mhaisalkar, S.; Hng, H. H.; Boey, F.; Ma, J.; Yan, Q. *Chem. Mater.* **2010**, *22* (18), 5333–5339.

[112] Xie, J.; Zhao, X.; Cao, G.; Zhong, Y.; Zhao, M. *J. Electroanal. Chem.* **2003**, *542*, 1–6.

[113] Hong, K.-S.; Nam, D.-H.; Lim, S.-J.; Sohn, D.; Kim, T.-H.; Kwon, H.-S. *ACS Appl. Mater. Interfaces* **2015**.

[114] Toprak, M. S.; Stiewe, C.; Platzek, D.; Williams, S.; Bertini, L.; Müller, E.; Gatti, C.; Zhang, Y.; Rowe, M.; Muhammed, M. *Adv. Funct. Mater.* **2004**, *14* (12), 1189–1196.

[115] Tarascon, J.-M.; Morcrette, M.; Dupont, L.; Chabre, Y.; Payen, C.; Larcher, D.; Pralong, V. *J. Electrochem. Soc.* **2003**, *150* (6), A732–A741.

[116] Park, C.-M.; Yoon, S.; Lee, S.-I.; Kim, J.-H.; Jung, J.-H.; Sohn, H.-J. *J. Electrochem. Soc.* **2007**, *154* (10), A917–A920.

[117] Hanzu, I.; Djenizian, T.; Knauth, P. *J. Phys. Chem. C* **2011**, *115*, 5989–5996.

[118] Weppner, W.; Huggins, R. A. *J. Electrochem. Soc.* **1977**, *124* (10), 1569–1578.

[119] Kamienski, C. W.; McDonald, D. P.; Stark, M. W.; Papcun, J. R. In *Kirk-Othmer Encyclopedia of Chemical Technology*; John Wiley & Sons, Inc., 2004.

[120] Ionica, C. M.; Aldon, L.; Lippens, P. E.; Morato, F.; Olivier-Fourcade, J.; Jumas, J.-C. *Hyperfine Interact.* **2004**, *156-157* (1-4), 555–561.